NACA RM L56I14

NACA

RESEARCH MEMORANDUM

EXPERIMENTAL STUDY AND ANALYSIS OF LOADING AND PRESSURE DISTRIBUTIONS ON DELTA WINGS DUE TO THICKNESS AND TO ANGLE OF ATTACK AT SUPERSONIC SPEEDS

By William B. Boatright

Langley Aeronautical Laboratory
Langley Field, Va.

NATIONAL ADVISORY COMMITTEE
FOR AERONAUTICS

WASHINGTON
December 26, 1956
Declassified February 8, 1960

NACA RM L56I14

NATIONAL ADVISORY COMMITTEE FOR AERONAUTICS

RESEARCH MEMORANDUM

EXPERIMENTAL STUDY AND ANALYSIS OF LOADING AND PRESSURE DISTRIBUTIONS ON DELTA WINGS DUE TO THICKNESS AND TO ANGLE OF ATTACK AT SUPERSONIC SPEEDS

By William B. Boatright

SUMMARY

The aerodynamic loading on delta wings at supersonic speeds was studied principally to determine the coupling and nonlinear interference effects between the pressures due to angle of attack and due to thickness. Pressure distributions on four delta wings having leading-edge sweep angles of 53°, 60°, and 66.6° were measured at Mach numbers of 1.62, 1.93, and 2.41. Three wings had NACA 65A003 sections. The other wing had a flat upper surface and a leading-edge sweep angle of 53°. At Mach numbers of 1.94 and 2.41, some of the results for this wing simulate a wing of zero thickness; the pressure distributions are compared with the pressure distributions of an NACA 65A003 section wing of the same plan form. For this comparison the pressure distributions of the NACA 65A003 section wing had the experimental pressure distributions at 0° angle of attack deducted. Appreciable nonlinear interference effects are shown to exist such that the pressure distributions caused by thickness and by angle of attack are not additive at test angles of attack greater than 5°. These effects are shown to exist for all the NACA 65A003 section wings at all test Mach numbers, and in each case the experimental results are compared with theory.

The pressure distributions due to wing thickness are shown for the NACA 65A003 section wings at all test Mach numbers and in some cases are compared with theory. Also, quantitative information on span loadings of delta wings is presented for a wider range of operating conditions than presently exist.

The limited study of Reynolds number effects include variations in Reynolds number produced both by increased tunnel stagnation pressure and by the use of transition strips located near the wing leading edge.

Some results are presented of tests which were made with the wing of zero thickness at angles of attack greater than that necessary to produce leading-edge shock detachment. These tests were conducted with and without a thin leading-edge extension (maintained at 0° angle of attack) in an attempt to evaluate the upper and lower wing surface interactions in the presence of a detached shock.

INTRODUCTION

Loading studies on delta wings at supersonic speeds have been the subject of a number of experimental investigations, for example, references 1 to 7. The reason for the predominance of delta-wing data is the basic nature of the delta plan form. Not only is the theoretical treatment simple, but also the pressure distributions due to angle of attack of many other plan forms are readily determined, in whole or in part, from the pressure distribution due to angle of attack of a basic delta wing. Evaluation of the experimental pressure distribution due to angle of attack is complicated by the coupling effects that exist between the pressure distribution due to thickness and that due to angle of attack. Reference 7 shows that for a 5-percent-thick, sharp leading-edge delta wing at Mach number 3.33 appreciable effects exist such that, even for as small an angle of attack as 3°, the pressure distributions due to thickness and those due to angle of attack are not additive.

In the investigation of this report the coupling effects between thickness and angle-of-attack pressures are further explored for thinner wings at several lower Mach numbers than the data of reference 7. Four wings were tested at Mach numbers of 1.62, 1.94, and 2.41. Three of the wings had NACA 65A003 sections and leading-edge sweep angles of 53°, 60°, and 66.6°. The other wing was a semiflat plate (designated herein as a zero-thickness wing) such that at Mach numbers for which its leading edge was supersonic (attached shock) the results for the flat surface corresponded to results for a wing of zero thickness. Tests were also conducted for this zero-thickness wing with and without a thin, sharp leading-edge extension (which was maintained at 0° angle of attack) in an attempt to evaluate the upper- and lower-surface interactions ("bleed-around" effects) in the presence of a detached shock.

The span loadings and lateral center of pressures are presented in order to supplement the available information of this type and to furnish quantitative data for a wider range of operating conditions than presently exist. The values of the ratios of semiapex angles to Mach angles covered by the tests of this report vary from about 0.55 to 1.65.

Pressure distributions due to thickness are shown and, in some cases, are compared with the predictions of a recent theoretical technique presented in reference 8.

The Reynolds number effects were assessed both by some additional tests at an increased stagnation pressure and by some tests with roughness strips near the leading edge of the wing.

SYMBOLS

A	aspect ratio
$b/2$	semispan (measured from root chord to tip of delta wing as if tip and trailing edge were not cut off)
$b'/2$	local semispan
c	local chord
c_r	root chord (with trailing edge not cut off)
c_N	section normal-force coefficient, $\int_0^1 \frac{p - p_\infty}{q} \frac{dx}{c}$
C_N	normal-force coefficient, N/qS
C_p	pressure coefficient, $\frac{p - p_\infty}{q}$
M	Mach number
N	normal force
p	local static pressure
p_∞	free-stream static pressure
q	free-stream dynamic pressure, $0.7p_\infty M^2$
R	Reynolds number (based on mean aerodynamic chord of 5.00 inches)
S	wing area
t	wing thickness
x	longitudinal distance along wing chord (measured from apex)
x'	longitudinal distance along wing chord (measured from leading edge)
y	distance along span normal to the root chord
α	angle of attack
β	$\sqrt{M^2 - 1}$

ϵ wing semiapex angle

Λ wing leading-edge sweep angle

ω angle between wing root chord and a conical ray from the apex

APPARATUS

Tunnel

All tests were conducted in the Langley 9-inch supersonic tunnel which is a continuously operating closed-circuit type in which the stagnation pressure and temperature, and the humidity of the tunnel air may be controlled. The different test Mach numbers are obtained by interchangeable nozzles which form a test section about 9 inches square.

Models

The semispan models were mounted from a boundary-layer bypass plate as shown in the photograph of figure 1. The bypass plate was rigidly attached to a plug which was mounted in a hole in the tunnel walls in which the schlieren windows are usually located. The window plug, bypass plate, and the various wings which were tested are shown in the photograph of figure 2. The steel wings had grooves cut on their surfaces into which the tubing leading to the orifices was inlaid. After installation of the tubing, a clear plastic was used to fill the grooves and to make the wing surface flush. Consquently, although the photographs show what appears to be a rough surface with many grooves, each wing surface was actually smooth.

Figure 3 shows a dimensional sketch of the various wing models and the location of the transition strips which were used for some of the tests. The orifice locations are given in table I. Because the wings were designed with constant t/c, they were very thin at the tips. In order to alleviate the loading on the thin portions of the wing, the tips and the trailing edges were cut off as shown in figure 3 such that for inviscid flow the pressure readings of any of the orifices would not be affected. Figure 4 shows a sketch of the semiflat wing (wing 1) with the leading-edge extension attached. A different, prebent extension was attached to the wing for each test angle of attack. The juncture of the wing leading edge and the bend line was faired such that a continuous, distinct corner was present along this juncture on the flat side of the wing. Some schlieren photographs made in the Langley 9-inch supersonic tunnel (not shown herein) at a Mach number 1.94 of a similar wing plan form indicated that the leading-edge extension shown in

figure 4 extended far enough forward of the leading edge to assure that the leading-edge extension was effective in preventing "bleed-around" effects at all test angles of attack.

TESTS

Most of the tests were conducted with smooth models at a Reynolds number of about 2.3×10^6. Simulation of a higher Reynolds number was attempted in additional tests by using transition strips near the leading edge in order to make the boundary layer turbulent rearward of the strip. The thickness of each strip was about 0.006 inch. The tests using transition strips were conducted for a limited number of angles of attack (-20°, -10°, 0°, 10°, and 20°) for all test Mach numbers. At a Mach number of 2.41, some tests were also conducted at a Reynolds number of about 4.65×10^6. This higher Reynolds number was produced by an increased stagnation pressure.

For most of the tests, the angles of attack were nominally 0°, 5°, 10°, 15°, and 20°. However, with the larger wings at the lower Mach numbers the angle-of-attack range was limited because of the tunnel choking.

The tests with the zero-thickness wing were supplemented at angles of attack beyond shock detachment by tests with and without a thin, sharp leading-edge extension (0.020 inch thick). The purpose of these tests was to evaluate interference effects between the upper and lower wing surfaces when the leading-edge shock was detached.

PROCEDURES AND PRECISION

All pressures were indicated on a multiple tube, mercury manometer. The manometer readings were photographed and the data were mechanically reduced to pressure-coefficient form.

Since the wings were instrumented on only one surface, the data corresponding to the high-pressure side were obtained by testing the wing at negative angles of attack, and the data corresponding to the low-pressure side were obtained by testing at positive angles of attack.

The angles of attack were measured using a clinometer on a reference, flattened surface of the wing mount, which extended outside the tunnel. The initial alinement of the wing, referenced to free-stream direction,

was measured with a cathetometer. The accuracy of this latter operation resulted in a probable error of $\pm 0.1^{\circ}$ in angle of attack. However, the errors in the angle-of-attack settings with respect to each other for any one test were probably $\pm 0.05^{\circ}$. For the tests at different Reynolds numbers, it was not necessary to reference the model again with respect to the free-stream direction; however, for the tests with roughness strips near the wing leading edge, this operation was necessary.

The maximum inaccuracy in the pressure-coefficient data, due to a constant error in reading the manometer, occurred for the tests at the lowest Reynolds number ($R = 2.3 \times 10^6$) and the accuracies to be quoted are based on these tests. These accuracies were essentially the same at all Mach numbers since the dynamic pressures were (for the purpose of accuracy estimates) essentially the same. This condition was a by-product of controlling the stagnation pressure so that the tests were conducted at constant Reynolds number for all test Mach numbers. Because the manometer was photographed and the data reduced mechanically, the accuracy was less than that obtained by direct manual recording which is estimated to be ± 0.003. A check of typical pressure-coefficient data obtained both directly and mechanically assessed the accuracy of the mechanically reduced pressure-coefficient data to be ± 0.005 for approximately 80 percent of the data and not ever exceeding ± 0.01.

No corrections were applied to the pressure-coefficient data for the local ± 0.01 Mach number variation that is known to occur throughout the region of the test section occupied by the wing. This variation in free-stream Mach numbers could produce an error in the pressure coefficient of ± 0.004 at $M = 2.41$, and ± 0.008 at $M = 1.62$.

RESULTS AND DISCUSSION

Span Loadings and Lift Coefficients

Figures 5, 6, 7, and 8 present the span load distributions for the four wings which were tested in this investigation. All data points were obtained by mechanically integrating the chordwise pressure distributions. The experimental loading is compared with the loading predicted by linear theory at some of the test angles of attack.

The well-known fact that the span loading on delta wings approaches a more triangular distribution as the angle of attack increases is apparent for all the test configurations. The primary purpose of this presentation of loading data is to supplement existing information so that accurate quantitative estimates of span load distributions will be possible for a wider range of values of $\beta \tan \epsilon$ and α than presently exist.

Figure 9 presents the lateral center-of-pressure data for the various test configurations. The figures are arranged in order of increasing values of $\beta \tan \epsilon$. Each vertical line at a value of $y/\frac{b}{2}$ of 0.33 represents the center-of-pressure location which would result if the loading were triangular. If the loading were elliptical, the center of pressure would be at a value of $y/\frac{b}{2}$ of 0.423. This location is denoted by another vertical line.

It is interesting to note that at 20° angle of attack the lateral centers of pressure for all test configurations are very close to the same value of $y/\frac{b}{2} = 0.35$. At lower angles of attack, the variations in the lateral center-of-pressure locations are much greater. As would be expected, the subsonic leading-edge wings at the lower angles of attack have a center of pressure approaching that for an elliptical loading and the supersonic leading-edge wings have centers of pressure at lower angles of attack that correspond to loadings that are between elliptical and triangular.

Figure 10 shows the normal-force-coefficient curves for the various wings at the various test Mach numbers. The results were obtained by mechanically integrating the span-load curves. The results are compared with the lift curves predicted by linear theory. In all cases the theory slightly overpredicts the slope except for the wing with the lowest aspect ratio (wing 4) at Mach number 1.62. For this configuration the better agreement between theory and experiment is undoubtedly associated with the increase in lift produced by the leading-edge vortex which forms on the low-pressure side of a wing with a highly sweptback leading edge when flying at low supersonic Mach numbers. (See refs. 9 and 10.)

It is interesting to note that the normal-force-coefficient curve for the zero-thickness wing (wing 1) has a slightly greater slope than the curve for the NACA 65A003 section wing of the same plan form (wing 2) and more closely approximates the prediction of linear theory. This is true except at Mach number 2.41 where there is essentially no difference between the normal-force curves for the two wings below an angle of attack of about 15°.

Pressure Distributions Due to Thickness

The pressure-distribution measurements with the various wings at 0° angle of attack are presented in figures 11, 12, and 13. Figure 11 presents the results for wings 1 and 2. Both of these wings had the same plan form ($\Lambda = 53°$) but wing 1 had a semiflat section and wing 2 had an NACA 65A003 section. Wing 1, at Mach numbers 1.94 and 2.41,

should have indicated zero pressure coefficient over its entire surface since at these two Mach numbers the leading edge was supersonic, and in the absence of viscosity the data should correspond to a zero-thickness wing at 0° angle of attack. At a Mach number of 1.62, the leading edge of wing 1 was only slightly subsonic ($\beta \tan \epsilon = 0.960$), and for the thin section that was used the leading-edge flow deflection angle was probably sufficiently small that the effects from the cambered surface of the wing did not appreciably affect the pressures on the flat surface which was instrumented.

The data for the zero-thickness wing indicate essentially zero pressure coefficient at all test Mach numbers except for two possibly erroneous test points which are shown in figure 11(a) for locations near the leading edge and near the tip. The generally small departures from zero-pressure coefficient for wing 1 are probably due to the ± 0.01 free-stream Mach number variation and to the fact that the wing surface was not absolutely flat. Because of the difficulty of machining this flat wing with such a thin section, the surface, instead of being absolutely flat, had about 0.010-inch concavity between the leading and trailing edge near the root chord.

The data in figure 11 pertaining to the NACA 65A003 section wing is denoted by the square symbols. A consistent and expected thickness effect is shown with positive pressures near the leading edge and negative pressures near the trailing edge. This similar trend in the data for all the wings at all test Mach numbers is evident in figures 11, 12, and 13. Also, there appears to be a general increase in the pressure level for the pressures due to thickness with increasing Mach number.

Figure 12 presents the thickness pressure distribution for wing 3 ($\Lambda = 60^\circ$) and figure 13 presents the thickness pressure distribution for wing 4 ($\Lambda = 66.6^\circ$). The pressure distributions are compared with linear theory in figures 13(a) and 13(b). The theoretical technique presented in reference 8 was used to compute the theoretical curves for the subsonic leading-edge configurations. This technique permits the calculation of the pressure at a given point for any arbitrary distribution of slopes of the wing surface in the Mach forecone ahead of the point. The method is semigraphical, but the formulas involved are simple. A more detailed description of the method can be found in reference 8, but the method will be summarized here to give the reader, who is unfamiliar with the method, an understanding of the approximations involved in the theoretical calculations.

Figure 14 shows a typical graphical layout that is necessary for the computation of the pressure at point P. Since the wings of the tests of this report had a constant t/c ratio at all spanwise stations, the surface slopes were conical with respect to the tip and lines of constant slope emanating from the tip were drawn. The Mach forecone from P was

divided into an arbitrary number of equal parallelograms (depending on the degree of accuracy needed in the calculations). The wing surface slope was assumed constant in each parallelogram and with a value which was equal to the surface slope at the center of each parallelogram. This slope was readily determined from the graphical layout such as figure 14. A simple formula determined the effect of each parallelogram on the pressure at point P, and the resulting pressure at P consisted of the sum of the effects of each parallelogram. It was only necessary to consider the summation of the parallelograms in region ABCP since the effects of triangles ABD and CBE were cancelled by the effects of the flow distortion between the leading edge and the Mach cone emanating from the wing apex. (See ref. 11.) The effects of the region DBEF on point P were computed in some cases but were found to be negligible for those cases.

For the configurations with subsonic leading edges for which the theory was computed, figures 13(a) and 13(b), the agreement between theory and experiment is good except for the fact that theory predicts a higher positive pressure near the leading edge for the outboard wing sections than actually exist. Since the publication of reference 8, a similar method has been presented in reference 12 for calculating the thickness pressure distributions for delta wings with supersonic leading edges. However, theoretical calculations of the thickness pressure distributions were not undertaken except for the two configurations with subsonic leading edges which are shown for wing 4 in figures 13(a) and 13(b). Calculations for the other configurations were not expected to be particularly informative because of the smallness of the pressure gradients involved for the thin wings of this investigation and because the experimental pressure distributions due to thickness were similar for all the wings, whether the leading edge was subsonic or supersonic

It should be mentioned that reference 13 presents a method based on shock-expansion theory for computing pressures in the region ahead of the Mach cone from the apex of a delta wing with a sharp supersonic leading edge. This method is applicable to any wing of this type with single-curved surfaces, but because of the round leading edges and the low Mach number range of the configurations tested in this report theoretical calculations of thickness pressure distributions using this method were not attempted.

Pressure Distributions Due to Angle of Attack and Interference Pressures Produced by Thickness

The study of pressure distributions on wings of generally used sections is complicated by distinguishing the contributions to the pressures that are due to thickness from the contributions that are due to

angle of attack. Linear theory assumes that the two types of pressures may be superposed; however, in reference 7 it is shown that even for 3° angle of attack at a Mach number of 3.3, there are important effects due to nonlinearities and the interference of the thickness pressures on the angle-of-attack pressures. In order to better describe the mechanism for the coupling of these two types of pressure distributions, consider the analogy of a two-dimensional, double-wedge section wing at angle of attack. The surface slope is the algebraic sum of the angle of attack and the local surface slope due to thickness δ. Busemann's second-order theory gives the following expression for the pressure coefficient:

$$C_P = C_1(\alpha + \delta) + C_2(\alpha + \delta)^2$$

or

$$C_P = C_1\alpha + C_1\delta + C_2\left(\alpha^2 + 2\alpha\delta + \delta^2\right)$$

where C_1 and C_2 are constants which are functions only of the Mach number. The well-known fact that nonlinearities of the type calculable by second-order theory cannot be superposed is obvious, since the cross-product term prohibits the addition of thickness and angle-of-attack effects. Inspection of this equation shows that it is possible for the thickness contribution to be small such that the term δ^2 is negligible, but that at sufficiently large angles of attack a small thickness might affect the nonlinearity of the pressure if the term $2\alpha\delta$ is significant. Furthermore, from this two-dimensional analogy it can be reasoned that the nonlinearities will be greater with increasing Mach number since C_2 increases with Mach number.

The test program used in this investigation for the study of the coupling effects between thickness and angle of attack consisted of tests with a wing which in inviscid flow simulates a zero-thickness wing at angles of attack below shock detachment and tests with NACA 65A003 section wings. One of the latter wings was of the same plan form as the zero-thickness wing and permitted direct comparison to determine second-order thickness effects on the angle-of-attack pressure distributions. The semiflat wing (wing 1) simulates a zero-thickness wing at Mach numbers for which its leading edge is supersonic (1.94 and 2.41) and at angles of attack below shock detachment, and the data for these conditions correspond to the assumptions of usual theoretical calculations. At angles of attack above shock detachment, an attempt was made to evaluate the upper- and lower-surface interactions in the presence of a leading-edge detached shock by testing with and without a thin leading-edge extension which was maintained at 0° angle of attack independent of the wing angle of attack.

Zero-thickness wing and comparison with theory.- Figures 15, 16, and 17 present the pressure measurements as a function of conical ray from the wing apex for the zero-thickness wing (wing 1) at three Mach numbers. The pressure-coefficient parameter is the value of the pressure coefficient at 0° angle of attack subtracted from the value at each particular test angle of attack and multiplied by β. The pressure-coefficient parameter is plotted against $\tan \omega / \tan \epsilon$. Plotted in this manner the data should define a single curve if the pressures are constant along conical rays from the wing apex. Although the data define a single curve reasonably well for angles of attack of 10° or less, generally, there is poor agreement between experiment and linear theory. (There is better agreement between theory and experiment at low angles of attack and lower Mach numbers, as might be expected.) This lack of ability of linear theory to predict actual pressures is well known but possibly underemphasized since attention is usually directed to how well it predicts lifting pressures.

Reference 14 presents an exact theory for computation of pressures on delta wings and points out large differences between the pressures computed by exact and linear theories. Reference 14 was not used to calculate some exact pressure distributions for the zero-thickness wing of this investigation because the calculations are laborious and because it was evident that, although the agreement between theory and experiment would be improved, the exact theory would still not predict the pressures very well. This latter reason was apparent because the exact theory of reference 14 uses shock-expansion theory for predicting the pressures in the region of the wing ahead of the Mach lines from the apex and predicts a constant pressure in this region for a zero-thickness wing. The experimental pressures were not constant in this region even for the zero-thickness wing of this investigation. Figure 17(b) shows the experimental pressures compared both with linear theory and shock-expansion theory for the outboard part of the wing and illustrates the poor agreement between theory and experiment for this Mach number at 10° angle of attack. Shock-expansion theory is sometimes used at higher Mach numbers to approximate the pressure over the entire wing surface by treating the wing section as if it were two dimensional. When used in this manner shock-expansion theory would predict a constant pressure over the entire surface for the zero-thickness wing (wing 1). It can be seen in figure 17(b), where the prediction of shock-expansion theory is shown for just the region of the wing ahead of the Mach lines from the apex, that for the Mach number range of this investigation the experimental pressures are not even constant in this region and that the assumption of constant pressure over the entire surface would be even more erroneous. If the assumption is made that the reason the pressures on the outboard part of this wing are not constant is due to viscous effects, it is interesting to note that these effects do not seriously disrupt the conical nature of the flow for this zero-thickness wing at angles of attack of 10° or less.

The data shown in figures 15, 16, and 17 for the zero-thickness wing at higher angles of attack than 10° show some departure from conical flow. Since it will be shown subsequently that the interference pressures produced by thickness cause similar departures from conical flow and to a greater extent than is shown in figures 15, 16, and 17 at higher angles of attack than 10°, it appears possible that the boundary layer on the wing might be causing the zero-thickness wing to have some effective thickness. This thickness effect for the resulting wing might then be the cause for the departures from conical flow which occur for high angles of attack.

Some of the data for the zero-thickness wing with and without the leading-edge extension is shown in figures 18 to 21. These data are plotted in the same manner as the preceding figures in order to illustrate the conical nature of the flow. The data for about 11° angle of attack or less define a single curve reasonably well, both with and without the leading-edge extension. This indicates that the flow is reasonably conical. If the corresponding angles of attack in figures 18 and 19 and in figures 20 and 21 are compared, it can be seen that there is very little difference in the data with or without the leading-edge extension, although to a slight extent the flow for the wing with the extension is less conical than the flow for the wing without the extension. This fact might be due to mechanical imperfections in the extension.

Some of the angles of attack for which data are presented are not necessarily high enough to produce a detached shock. Because one surface of the wing was flat and the other surface was a thin wedge (3 percent thick), the angle of attack at which the shock detached was different at positive angles of attack from that at negative angles of attack. At Mach number 1.94, the shock from the wedge side of the wing would be detached even with the wing at 0° angle of attack. When obtaining data for the high-pressure side (that is, with the wing at a negative angle of attack), theoretically the shock would detach at an angle of attack of -5.3°. At a Mach number of 2.41, the shock detaches at -17.7° and +8.0° angle of attack.

Figures 22 and 23, where pressure coefficient is plotted against chord location, also show some typical results with and without the leading-edge extension. In both figures there is a tendency for the pressures on the high-pressure side of the wing to be more positive with the extension than without. This effect was usually more predominant near the leading edge and was in the expected direction since it can be reasoned that the extension would suppress the pressure-relieving effect of the leading edge with a detached shock. However, this effect was not pronounced at all angles of attack and spanwise stations, and in many of these cases the effect of the extension was negligible for that portion of the wing surface which was instrumented.

For the low-pressure side of the wing, the effect of the extension was, in general, opposite to what might have been expected if the same reasoning had been used as for the high-pressure side. Instead of the pressures being more negative with the extension, they were less negative near the leading edge in almost every case. Usually, this effect was sufficiently small that it might be considered negligible within the accuracy of the data; however, the data for $\alpha = 9.3^\circ$ and $\alpha = 11.3^\circ$ at $y/\frac{b}{2} = 0.55$ inch (fig. 22) show an effect that is definitely greater than the accuracy of the data. A similar effect was noticed for other outboard stations at this Mach number. A possible explanation for this type of effect is that the boundary layer on the upper surface prevented the full theoretical expansion of the flow. It would be expected that this effect might become important on the low-pressure side of the wing where the boundary layer is relatively thick and not be important on the high-pressure side with its thin boundary layer. The possibility also exists that, although the leading-edge extension was carefully set at 0° angle of attack, possibly the deflection of the wing under load caused a warping of the thin leading-edge extension at these higher angles of attack. In any case, compared with the discrepancy between experiment and linear theory, which is shown for higher angles of attack in figures 22 and 23, the effects of the leading-edge extension were small. For predicting the pressure distribution, the theory does not agree with the experimental results either with or without the leading-edge extension.

NACA 65A003 section wings.- Figures 24 to 32 present the pressure data in the same manner as figures 15, 16, and 17 except that figures 24 to 32 apply to the NACA 65A003 section wings instead of the zero-thickness wing. This presentation is similar to that of reference 7 and extends the studies of reference 7 to thinner wings at lower Mach numbers. Since the values of the pressure coefficients at 0° angle of attack are subtracted from the values at each particular test angle of attack, the thickness pressure distribution for these figures is supposedly not present and the pressure distributions are due solely to angle of attack, if thickness and angle of attack effects are purely additive. However, figures 24 to 32 show that the thickness and angle-of-attack effects are not purely additive even for the thin, 3-percent-thick wings of this investigation, since the data indicate that the flow on the wing is not conical for test angles of attack greater than 5°. Instead of a single curve, the data indicate a regular and consistent departure from conical flow for these configurations. Since the data do define a single curve reasonably well at 5° angle of attack, the effects of thickness are not so strong as those presented in reference 7. Reference 7 showed appreciable departures from conical flow at 3° angle of attack for a sharp leading-edge, 5-percent-thick, delta wing at a Mach number of 3.33.

If the data of figures 24, 25, and 26 are compared with the data of figures 15, 16, and 17, it is apparent that the departures from conical

flow at test angles of attack greater than 5° are more pronounced for wing 2 (the NACA 65A003 section wing) than for wing 1 (the zero-thickness wing) at corresponding angles of attack. This comparison is a direct indication of the second-order effects of even the small amount of thickness of a 3-percent-thick wing on the pressure distributions.

The departure from conical flow in figures 27 to 32 are similar to the departures shown in figures 24, 25, and 26 and indicate that the effects of Mach number and aspect ratio on these nonlinear, second-order thickness effects are secondary. In this connection, it will be remembered that the thickness pressure distributions were similar for wings 2, 3, and 4. (See figs. 11, 12, and 13.) It is also apparent in figures 24 to 32 that the departures from conical flow due to the second-order thickness effects are greater than the direct effects of thickness on the pressure distributions.

Since it was shown that linear theory did not predict the pressure distributions adequately even for a zero-thickness wing at angles of attack of 10° and above, the fact that there is poor agreement between theory and experiment for these wings with thickness is as expected.

Pressure contours.- Since figures 24 to 32 show consistent departures from conical flow due to second-order thickness effects, some typical pressure contours are presented in figures 33 to 43 to permit better visualization of these effects. The contours were constructed by linearly interpolating between the pressure readings of each longitudinal row of orifices to determine the location of each contour at each spanwise station. These locations were then joined by straight lines. Figures 33, 34, and 35 show pressure contours for wing 1 with and without the leading-edge extension. The remaining figures are for the wings with NACA 65A003 sections. In each case, the pressures at 0° angle of attack were subtracted from the pressures at each particular test angle of attack. The contours with and without the leading-edge extension were, in general, very similar (figs. 33, 34, and 35) at corresponding angles of attack. It should be pointed out that, for wings on which a shallow pressure gradient exists over a large region, variations in the patterns of the individual contours in this region can be greatly changed by small inaccuracies or insignificant local-pressure fluctuations. For this reason, too much significance should not be attached to the locations of individual contours in regions where the contour spacing is large, but attention should be confined to the overall general effects shown by the contours.

Figures 36 to 43 show that the general effect of the thickness coupling on the angle-of-attack pressure contours is to cause deviations from straight conical contours to curved contours which are convex with respect to the wing leading edge. Viscous effects such as separation near the wing trailing edge could also cause this same type of curvature

and is believed to account for part of the deviations from conical flow which were experienced for wing 1 at high angles of attack.

The pressure contours of figures 33 to 43 illustrate graphically the steeper pressure gradients that occur on wings of lower aspect ratios at lower Mach numbers than occur on wings of higher aspect ratios at higher Mach numbers.

Reynolds Number Effects

Although the study of Reynolds number effects was not one of the primary objectives of this investigation, some data to help evaluate Reynolds number effects were obtained. Typical data showing Reynolds number effects are shown in figure 44 and 45. Figure 44(a) shows a chordwise pressure distribution for the wing of lowest aspect ratio at the lowest Mach number. Figure 44(b) shows a spanwise pressure distribution for the same configuration. Figure 45 represents corresponding data for the wing of highest aspect ratio at the highest Mach number. No pronounced Reynolds number effects are apparent in the data. For many of the pressure distributions of other configurations which are not shown, there were small Reynolds number effects on the low-pressure side of the wing of the same order of magnitude as shown in figure 45(a). This low-pressure side of the wing consistently showed the greatest scatter in the curves; however, the effect is so small that it is questionable whether it is real or due to the inaccuracy of the data.

Since references 2 and 3 showed more pronounced effects of Reynolds number on the pressure distributions of a 68.4° sweptback delta wing, it is not correct to generalize that Reynolds number effects are always negligible for delta wings. The wing used in the investigation of references 2 and 3 had a different section (NACA 00-series) and had a thickness ratio varying from 4 percent at the root to 6 percent at the tip. Also, the investigation of Reynolds number effects was the primary objective in references 2 and 3 and smaller angle-of-attack increments were chosen in order to obtain a better history of separation phenomena throughout the angle-of-attack range. Reference 1 also presents some test results for delta wings with higher aspect ratios than the wing which was tested in references 2 and 3 and shows no pronounced Reynolds number effects. There is, therefore, some indication that Reynolds number effects are associated with wings of low aspect ratio if they are sufficiently thick.

CONCLUSIONS

Pressure distribution and loading studies on delta wings with zero thickness and with NACA 65A003 sections at test Mach numbers of 1.62, 1.94, and 2.41 have obtained the following results and indicated the following conclusions:

1. The well-known tendency for the loading on delta wings to become more triangular with increasing angle of attack is shown quantitatively for a wider range of operating conditions than the range for which data currently exist.

2. The location of the lateral centers of pressure for all the wings of this investigation at all test Mach numbers were essentially the same at 20° angle of attack. This center-of-pressure location was at 35 percent of the semispan. At lower angles of attack, there were greater variations in the lateral center-of-pressure locations and these locations were shown quantitatively.

3. Tests with a wing of zero thickness disclosed that at angles of attack of 10° or less the flow was conical at all test Mach numbers, and only small departures from conical flow were present at higher angles of attack.

4. The wing of zero thickness was tested at angles of attack greater than those necessary to produce leading-edge shock detachment, with and without the thin leading-edge extension, in order to evaluate pressure-distribution phenomena associated with leading-edge shock detachment. For the most part, the leading-edge extension had little effect on the pressure distributions.

5. Although conical flow existed on the wing of zero thickness at 10° angle of attack, linear theory was shown to be inadequate for predicting the actual pressures on the wing surface at this or higher angles of attack. Contrary to the prediction of shock-expansion theory the experimental pressures were not constant in the region ahead of Mach lines from apex.

6. Even for the thin NACA 65A003 section wings of this investigation, appreciable nonlinear interference effects were shown to exist between the angle of attack and the thickness pressure distributions at test

angles of attack greater than 5°. These effects caused regular and consistent departures from conical flow in the pressure distributions.

Langley Aeronautical Laboratory,
National Advisory Committee for Aeronautics,
Langley Field, Va., August 29, 1956.

REFERENCES

1. Boyd, John W., and Phelps, E. Ray: A Comparison of the Experimental and Theoretical Loading Over Triangular Wings at Supersonic Speeds. NACA RM A50J17, 1951.

2. Hatch, John E., Jr., and Hargrave, L. Keith: Effects of Reynolds Number on the Aerodynamic Characteristics of a Delta Wing at Mach Number of 2.41. NACA RM L51H06, 1951.

3. Hatch, John E., Jr., and Gallagher, James J.: Aerodynamic Characteristics of a 68.4° Delta Wing at Mach Numbers 1.6 and 1.9 Over a Wide Reynolds Number Range. NACA RM L53I08, 1953.

4. Kaattari, George E.: Pressure Distributions on Triangular and Rectangular Wings to High Angles of Attack - Mach Numbers 1.45 and 1.97. NACA RM A54D19, 1954.

5. Kaattari, George E.: Pressure Distributions on Triangular and Rectangular Wings to High Angles of Attack - Mach Numbers 2.46 and 3.36. NACA RM A54J12, 1955.

6. Katzen, Elliot D., and Pitts, William C.: Load Distributions on Wings and Wing-Body Combinations at High Angles of Attack and Supersonic Speeds. NACA RM A55E17, 1955.

7. Katzen, Elliot D.: Limitations of Linear Theory in Predicting the Pressure Distribution on Triangular Wings. Jour. Aero. Sci. (Readers' Forum), vol. 22, no. 7, July 1955, pp. 514-516.

8. Etkin, Bernard, and Woodward, Frank A.: Lift Distribution on Supersonic Wings With Subsonic Leading Edges and Arbitrary Angle of Attack Distribution. Jour. Aero. Sci. (Readers' Forum), vol. 21, no. 11, Nov. 1954, pp. 783-785.

9. Brown, Clinton E., and Michael, William H., Jr.: On Slender Delta Wings With Leading-Edge Separation. NACA TN 3430, 1955.

10. Michael, William H., Jr.: Flow Studies on Flat-Plate Delta Wings at Supersonic Speed. NACA TN 3472, 1955.

11. Evvard, John C.: Distribution of Wave Drag and Lift in the Vicinity of Wing Tips at Supersonic Speeds. NACA TN 1382, 1947.

12. Etkin, B.: Lift Distribution on Warped Supersonic Wings. Canadian Aero. Jour., vol. 1, no. 1, Apr. 1955, pp. 16-20.

13. Vincenti, Walter G., and Fisher, Newman H., Jr.: Calculation of the Supersonic Pressure Distribution on a Single-Curved Tapered Wing in Regions not Influenced by the Root or Tip. NACA TN 3499, 1955.

14. Fowell, L. R.: An Exact Theory of Supersonic Flow Around A Delta Wing. UTIA Rep. No. 30, Univ. of Toronto, Inst. Aerophysics, Mar. 1955.

TABLE I.- WING-ORIFICE LOCATIONS

Wing 1

Row	$y/\frac{b}{2}$	x'/c								
A	0.100	0.122	0.213	0.317	0.423	0.538	0.635	0.735	0.833	0.918
B	.250	.122	.218	.310	.406	.498	.589	.682	.798	.903
C	.400	.126	.222	.317	.411	.506	.605	.748	.877	
D	.550	.163	.267	.371	.479	.602	.728	.835		
E	.700	.218	.358	.495	.642	.758				
F	.800	.319	.434	.553	.633					
Row	x/c_r	$y/\frac{b'}{2}$								
1	0.476	0.201	0.360	0.513	0.668	0.826				
2	.762	.126	.227	.323	.426	.521	0.621	0.715	0.821	0.913

Wing 2

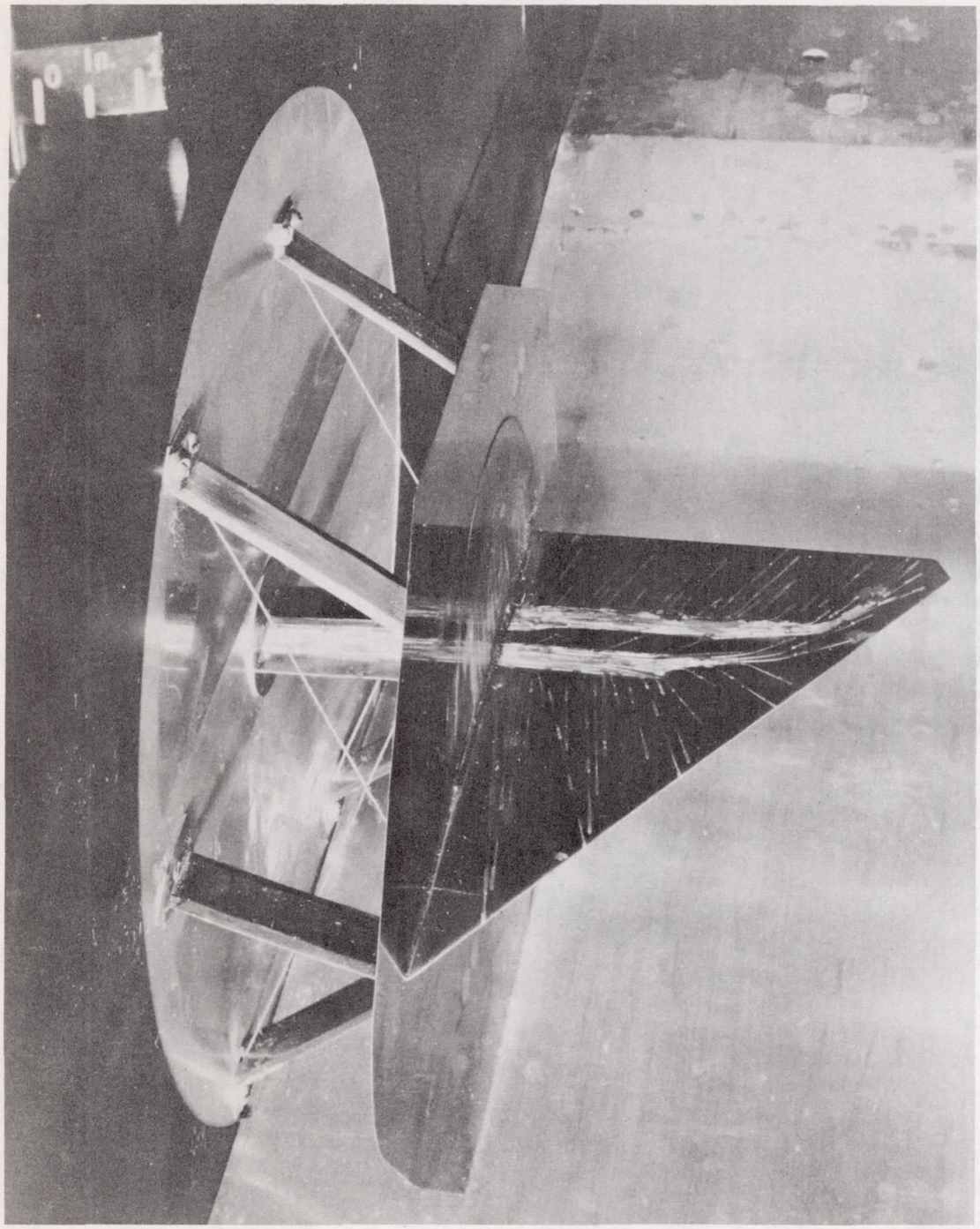
Row	$y/\frac{b}{2}$	x'/c								
A	0.100	0.040	0.132	0.263	0.424	0.528	0.634	0.737	0.832	0.918
B	.250	.033	.107	.205	.302	.428	.562	.684	.801	.901
C	.400	.038	.123	.244	.362	.482	.604	.743	.875	
D	.550	.083	.204	.331	.476	.595	.720	.835		
E	.700	.103	.221	.402	.598	.751				
F	.800	.219	.349	.484	.632					
Row	x/c_r	$y/\frac{b'}{2}$								
1	0.477	0.211	0.368	0.524	0.674	0.829				
2	.762	.135	.235	.329	.431	.525	0.625	0.713	0.820	0.913

Wing 3

Row	$y/\frac{b}{2}$	x'/c								
A	0.100	0.025	0.113	0.259	0.410	0.524	0.634	0.740	0.838	0.918
B	.250	.025	.120	.203	.299	.431	.561	.688	.799	.904
C	.400	.034	.117	.236	.357	.480	.605	.751	.878	
D	.550	.051	.170	.310	.472	.590	.731	.823		
E	.700	.094	.188	.379	.578	.749				
F	.800	.158	.305	.468	.602					
Row	x/c_r	$y/\frac{b'}{2}$								
1	0.473	0.208	0.368	0.529	0.685	0.848				
2	.766	.131	.237	.331	.433	.529	0.729	0.852	0.928	

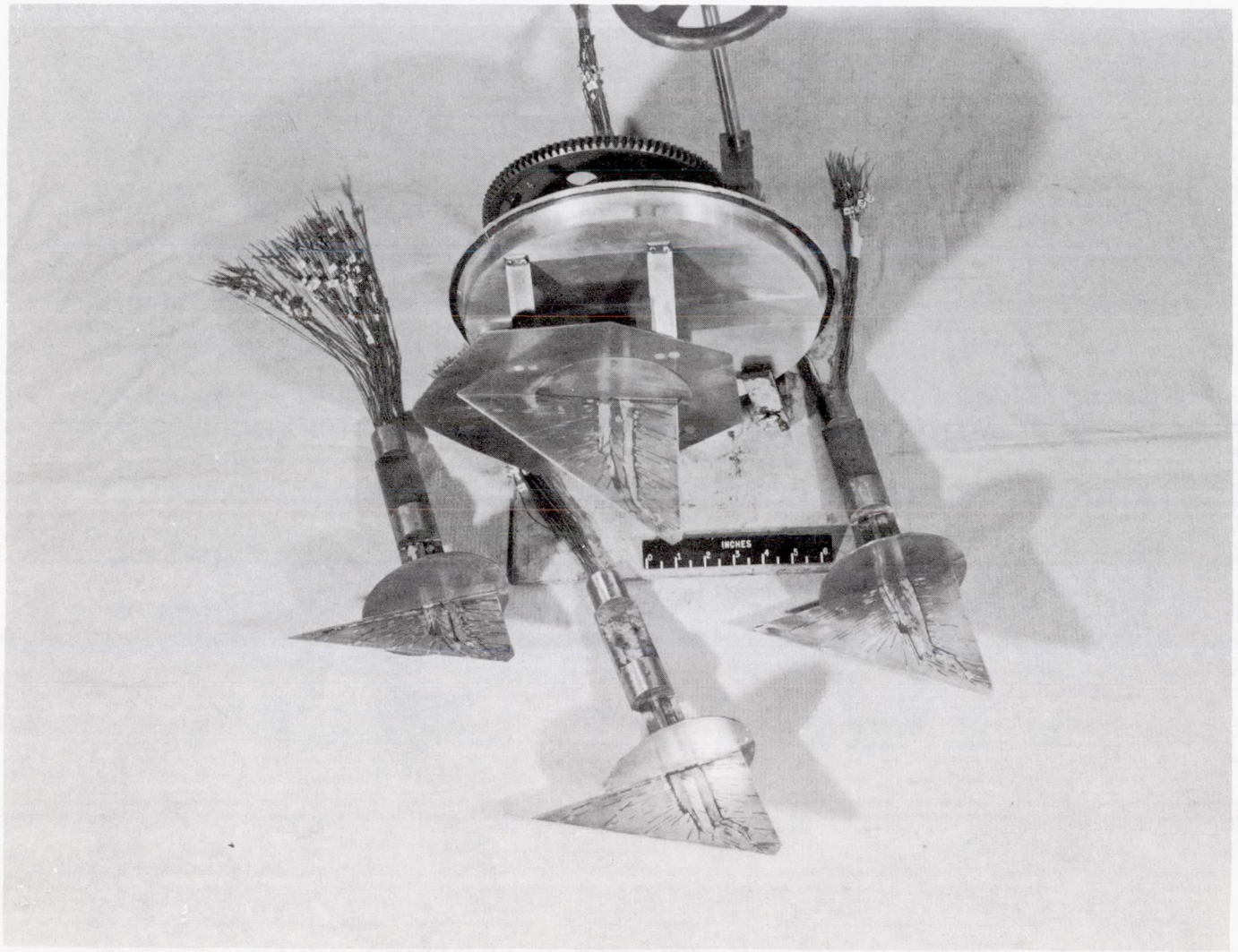
Wing 4

Row	$y/\frac{b}{2}$	x'/c								
A	0.100	0.042	0.124	0.252	0.419	0.534	0.637	0.738	0.836	0.919
B	.250	.030	.120	.221	.313	.439	.563	.685	.801	.903
C	.400	.054	.128	.248	.367	.483	.605	.747	.878	
D	.551	.092	.202	.342	.482	.603	.736	.841		
E	.701	.066	.167	.385	.572	.752				
F	.801	.187	.326	.465						
Row	x/c_r	$y/\frac{b'}{2}$								
1	0.476	0.200	0.373	0.517	0.672	0.831				
2	.757	.129	.229	.326	.424	.525	0.622	0.720	0.830	0.899



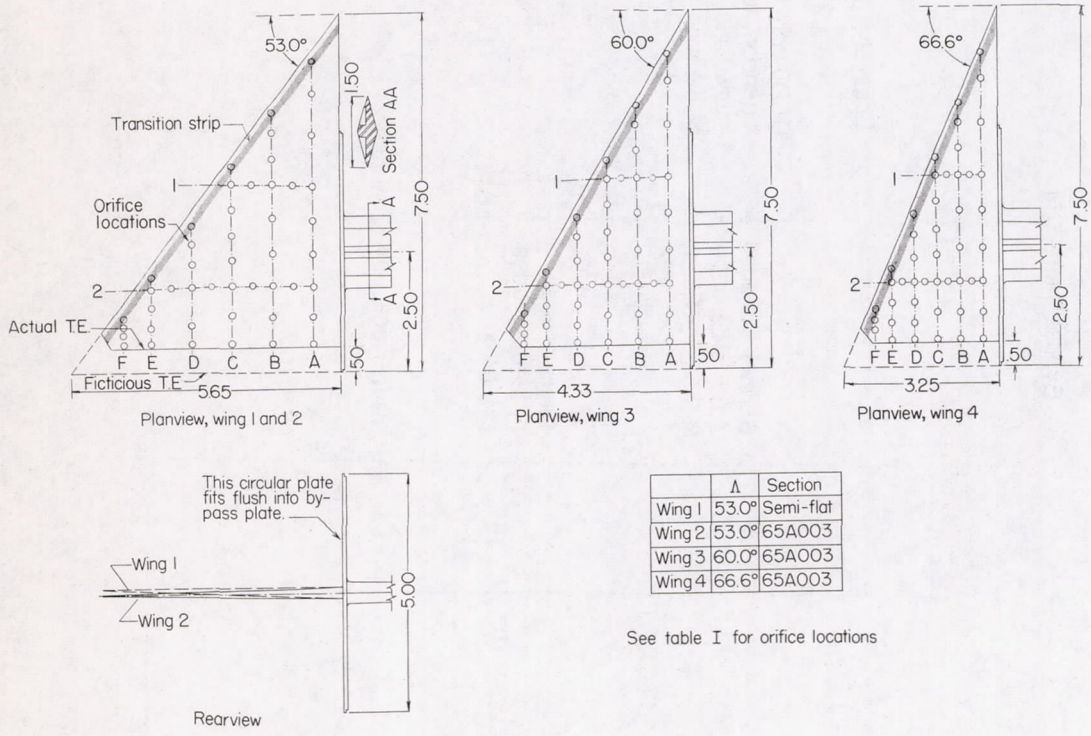
L-92734

Figure 1.- Photograph of wing model and bypass plate mounted in tunnel. (Top half of tunnel nozzle removed.)



L-92573

Figure 2.- Photograph of various wings tested and bypass plate.



	Λ	Section
Wing 1	53.0°	Semi-flat
Wing 2	53.0°	65A003
Wing 3	60.0°	65A003
Wing 4	66.6°	65A003

See table I for orifice locations

Figure 3.- Dimensional sketch of various wing models showing orifice locations. (All dimensions in inches.)

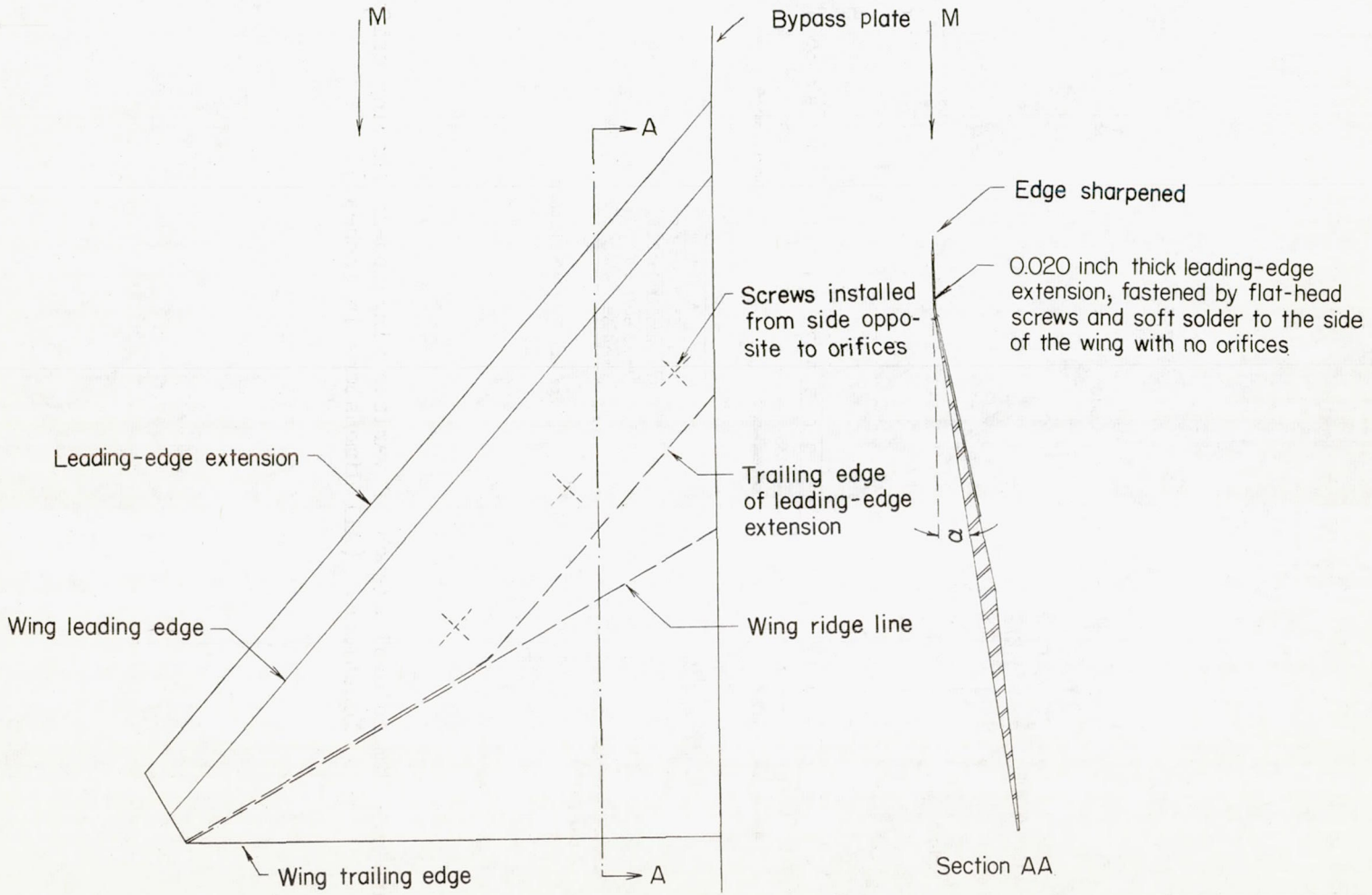


Figure 4.- Sketch of wing 1 showing method of attaching leading-edge extension.

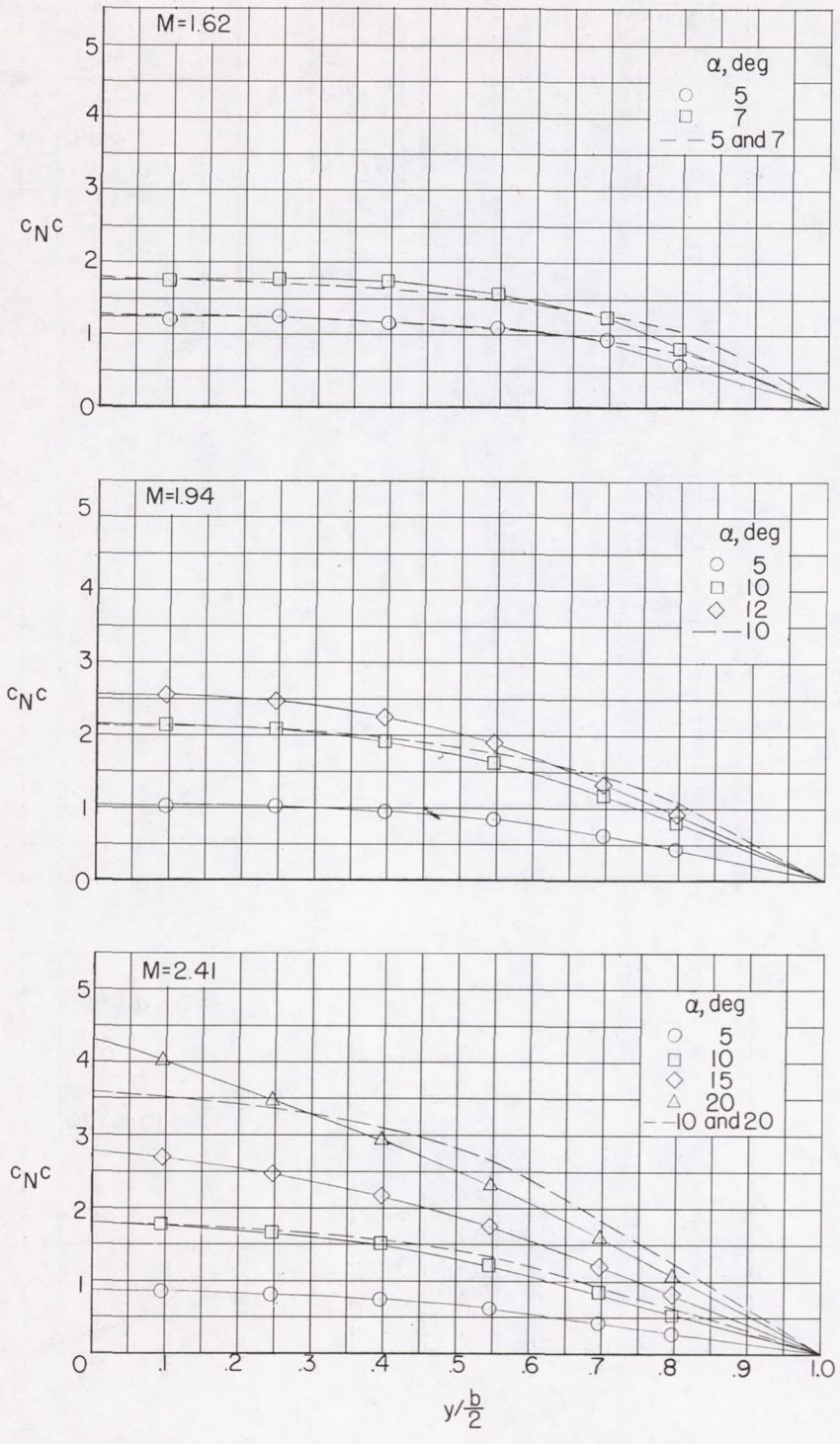


Figure 5.- Span load distributions for wing 1 ($\Lambda = 53^{\circ}$). (Dashed curves represent linear theory.)

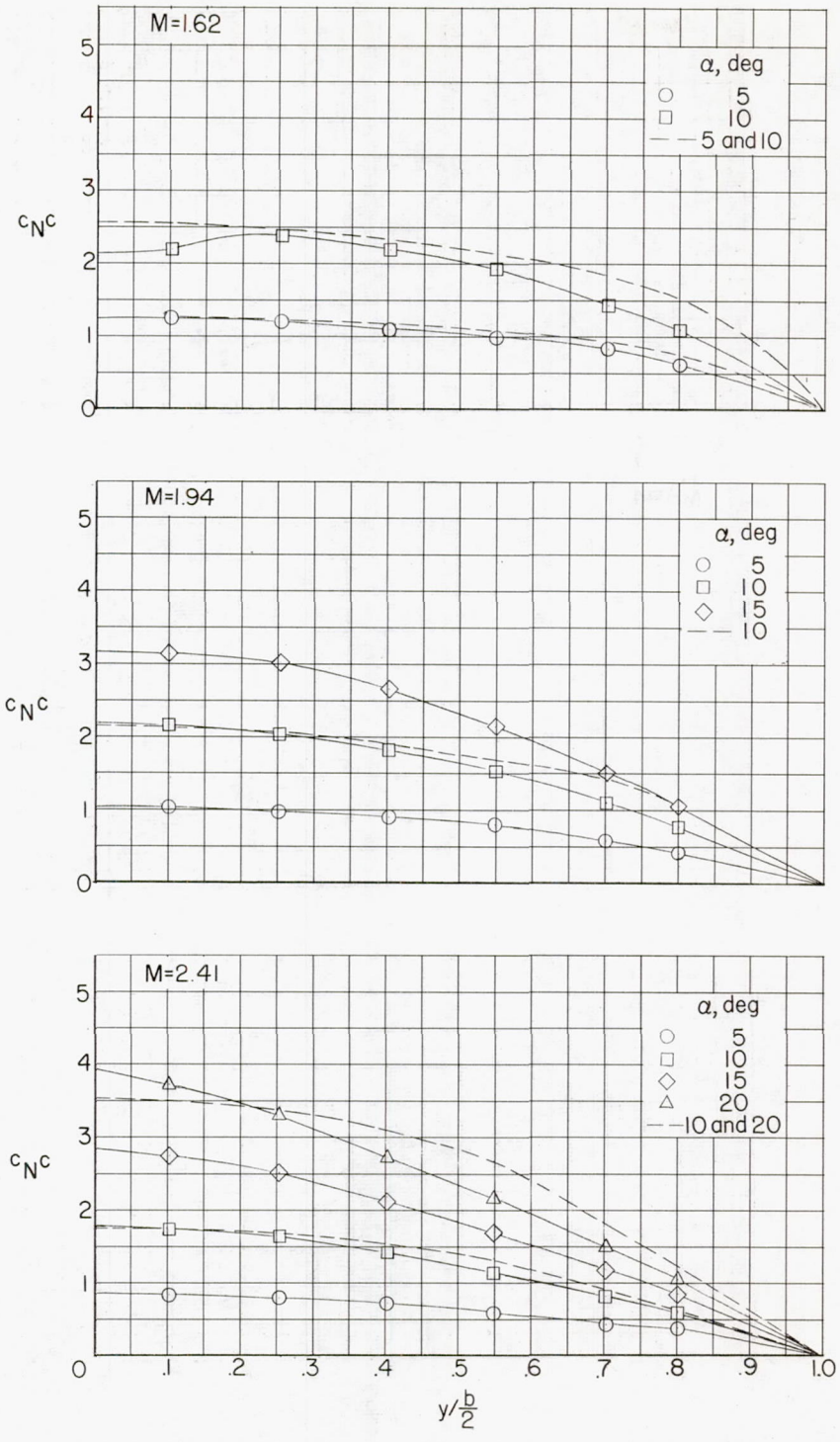


Figure 6.- Span load distributions for wing 2 ($\Lambda = 53^{\circ}$). (Dashed curves represent linear theory.)

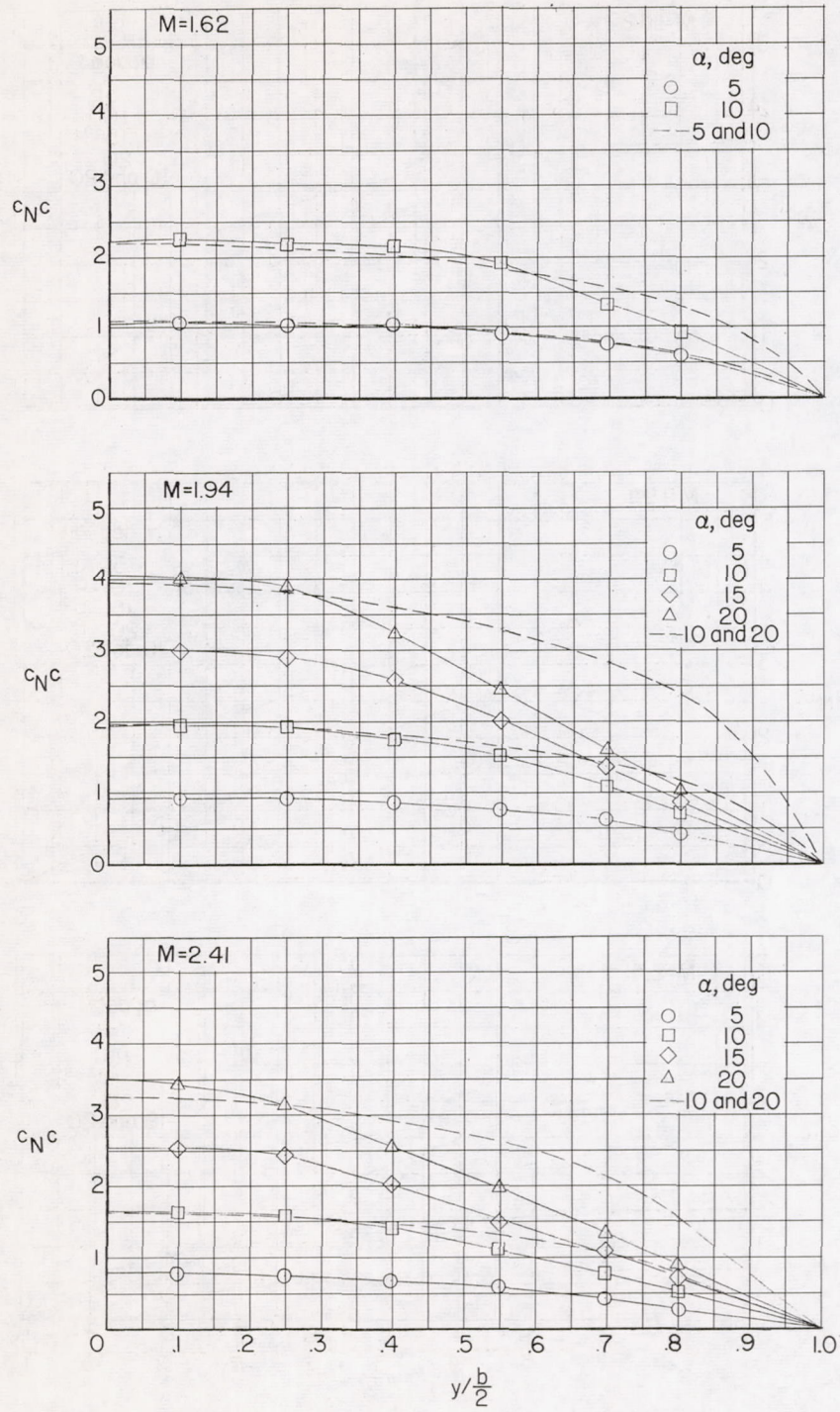


Figure 7.- Span load distributions for wing 3 ($\Lambda = 60^{\circ}$). (Dashed curves represent linear theory.)

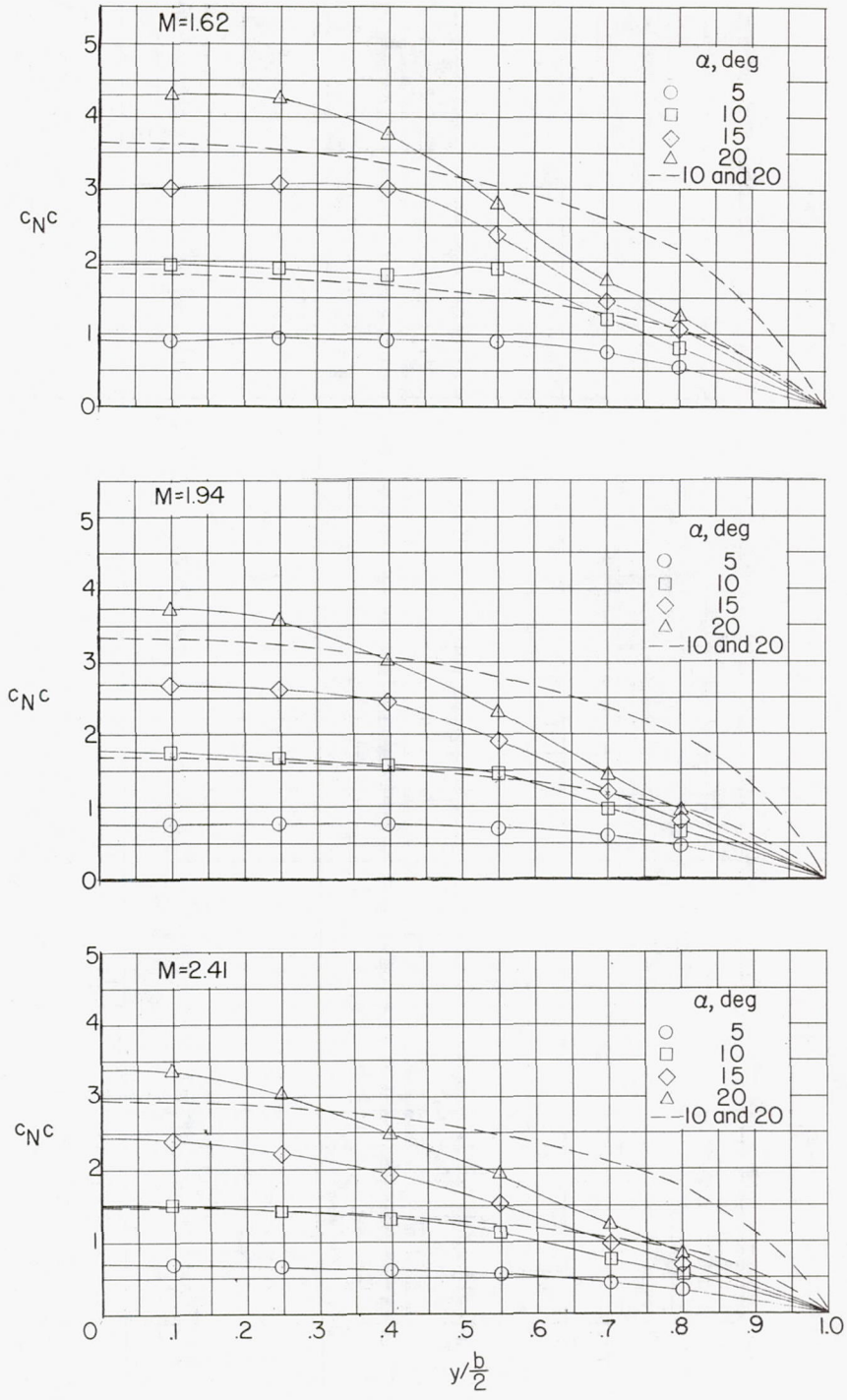


Figure 8.- Span load distributions for wing 4 ($\Lambda = 66.6^{\circ}$). (Dashed curves represent linear theory.)

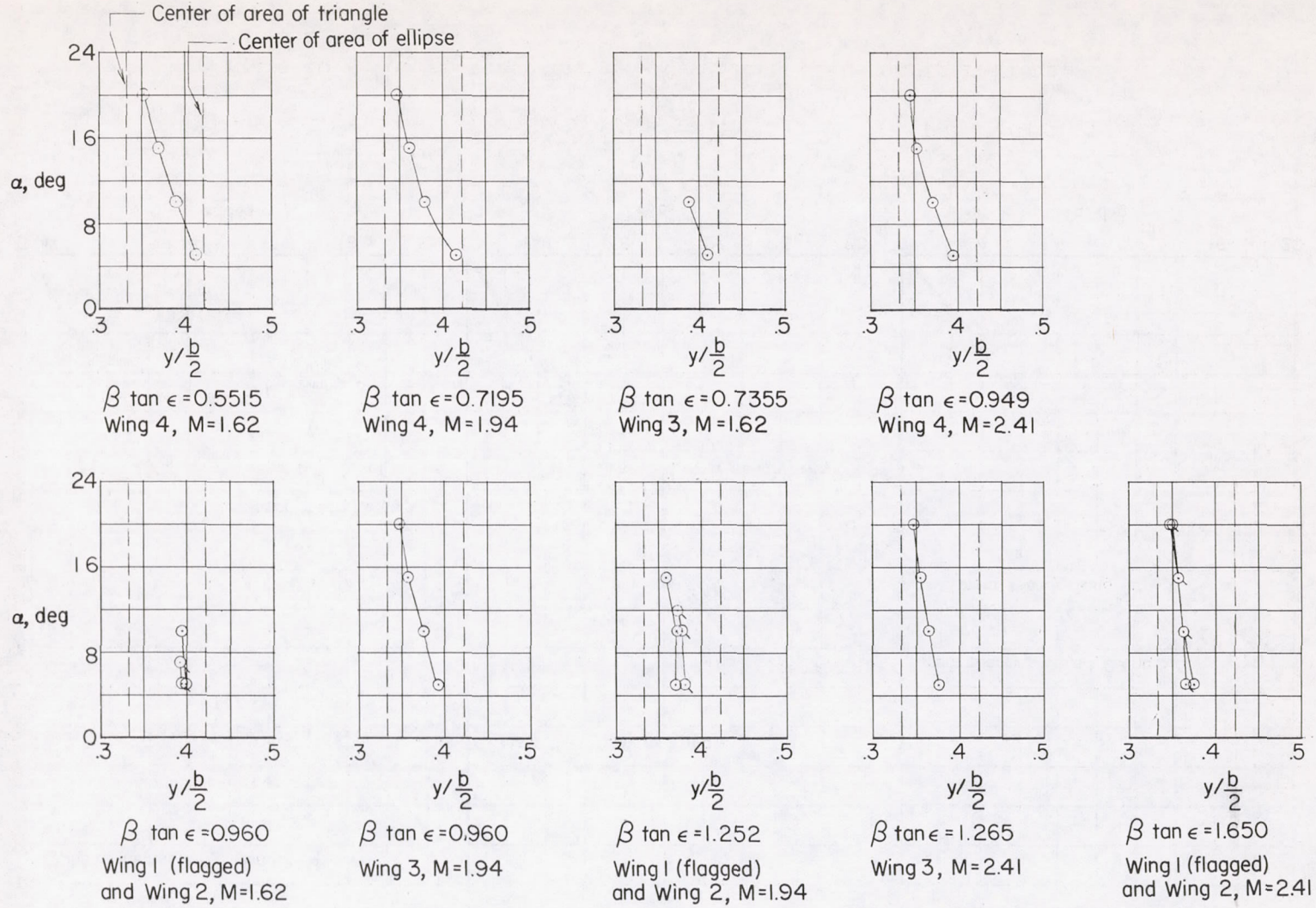
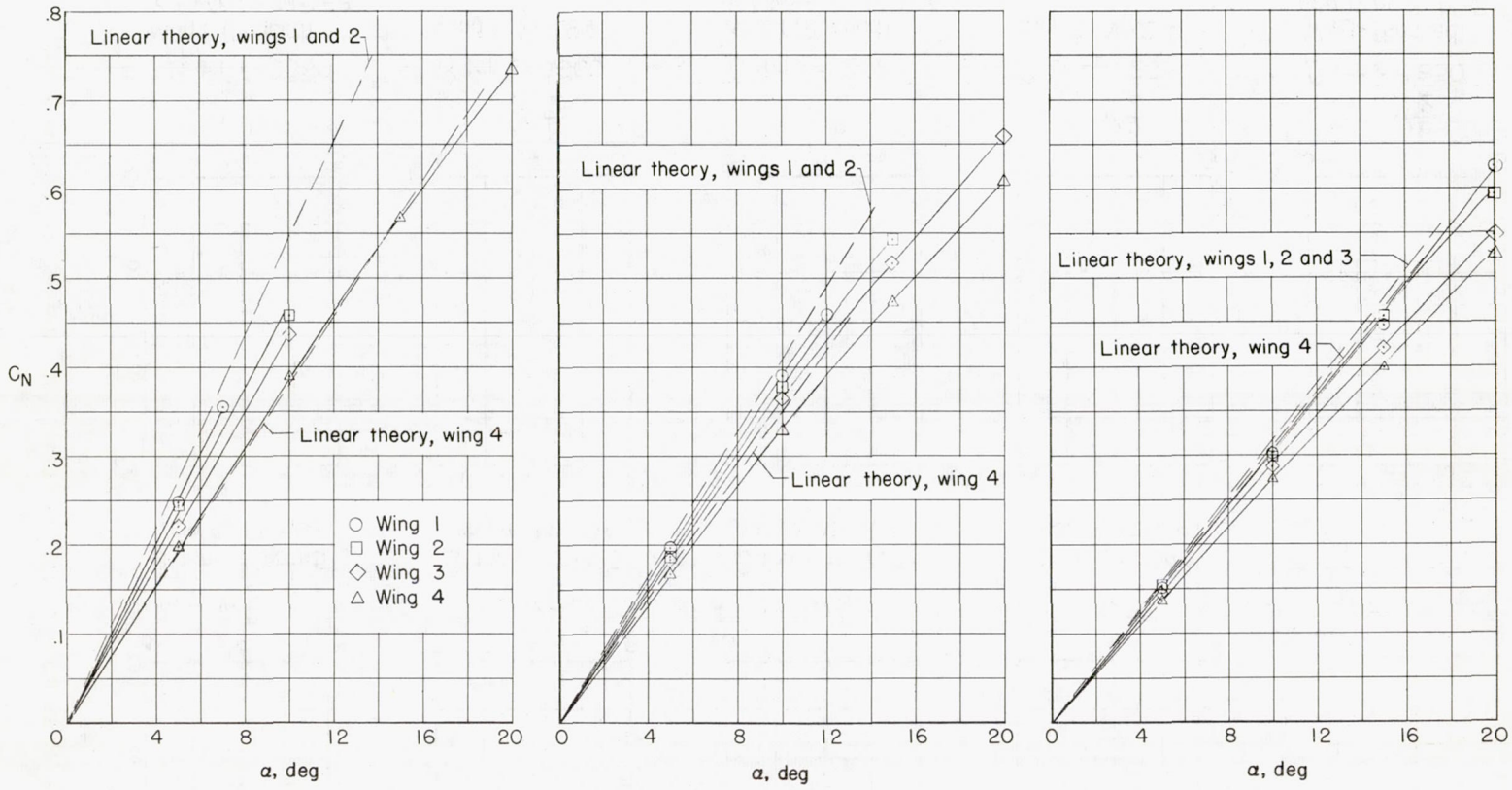
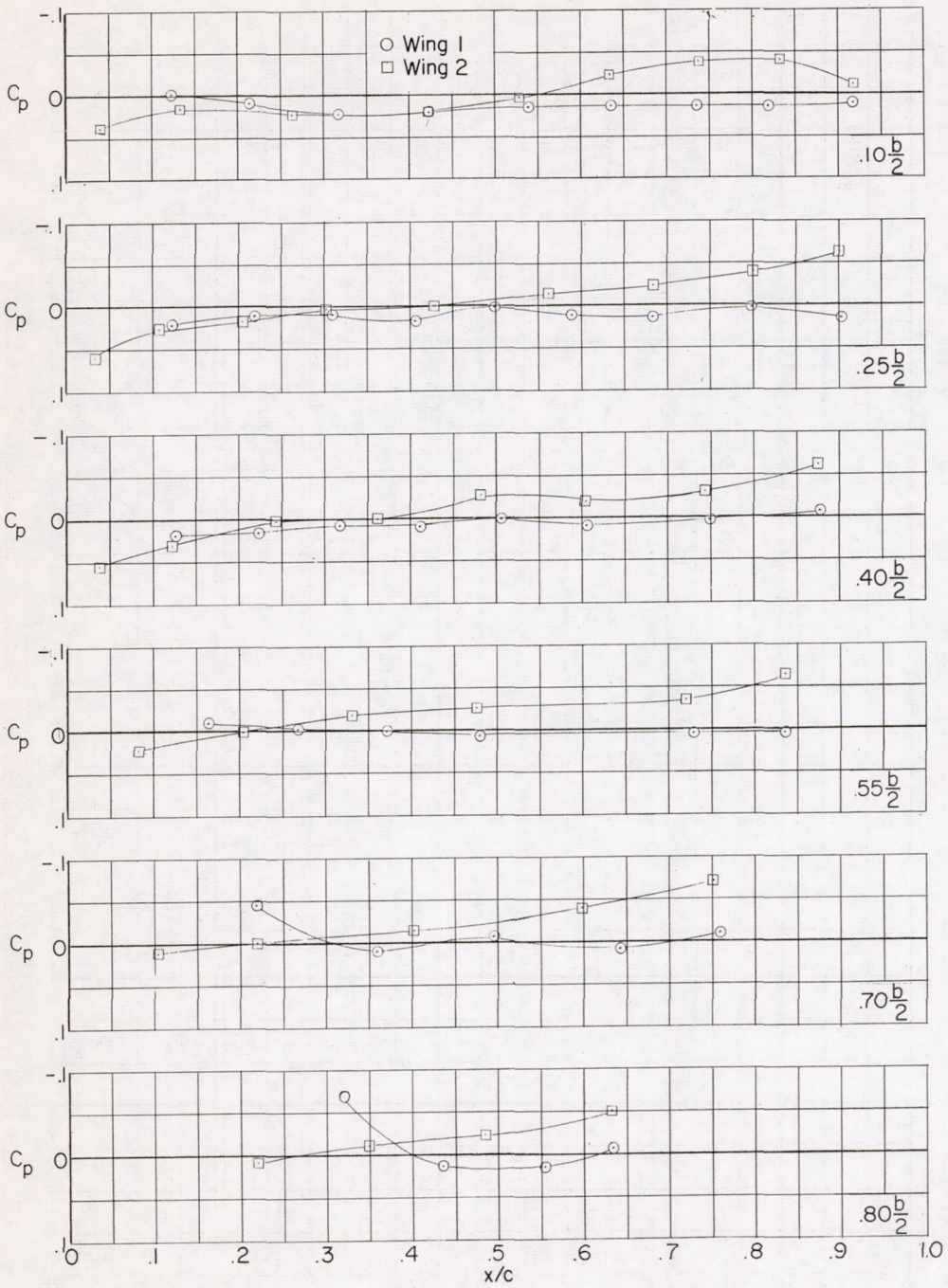


Figure 9.- Lateral center-of-pressure data for various test configurations.



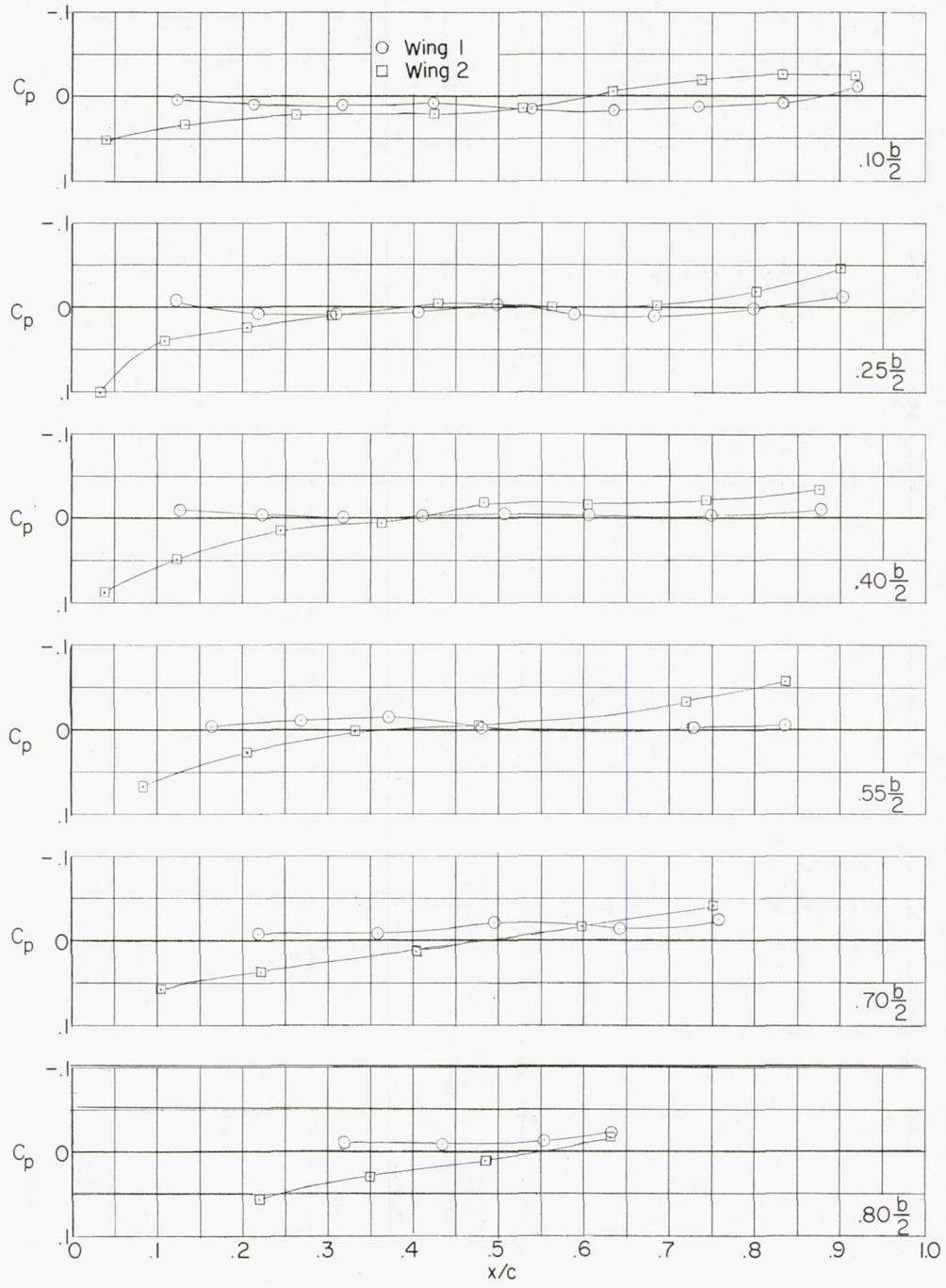
(a) M = 1.62. (b) M = 1.94. (c) M = 2.41.

Figure 10.- Normal force curves of various test configurations.



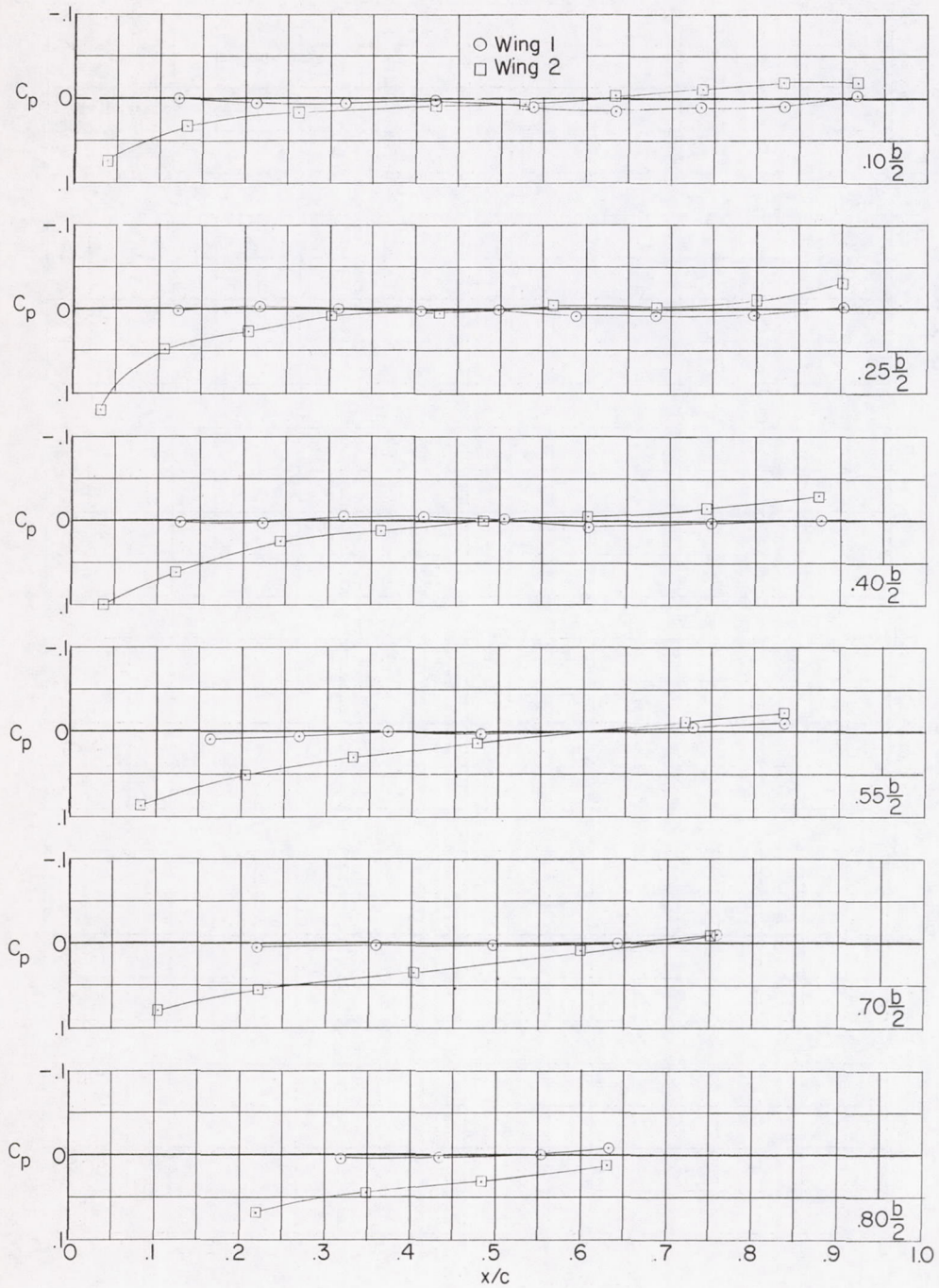
(a) M = 1.62.

Figure 11.- Pressure distributions at $\alpha = 0^{\circ}$. Wings 1 and 2.



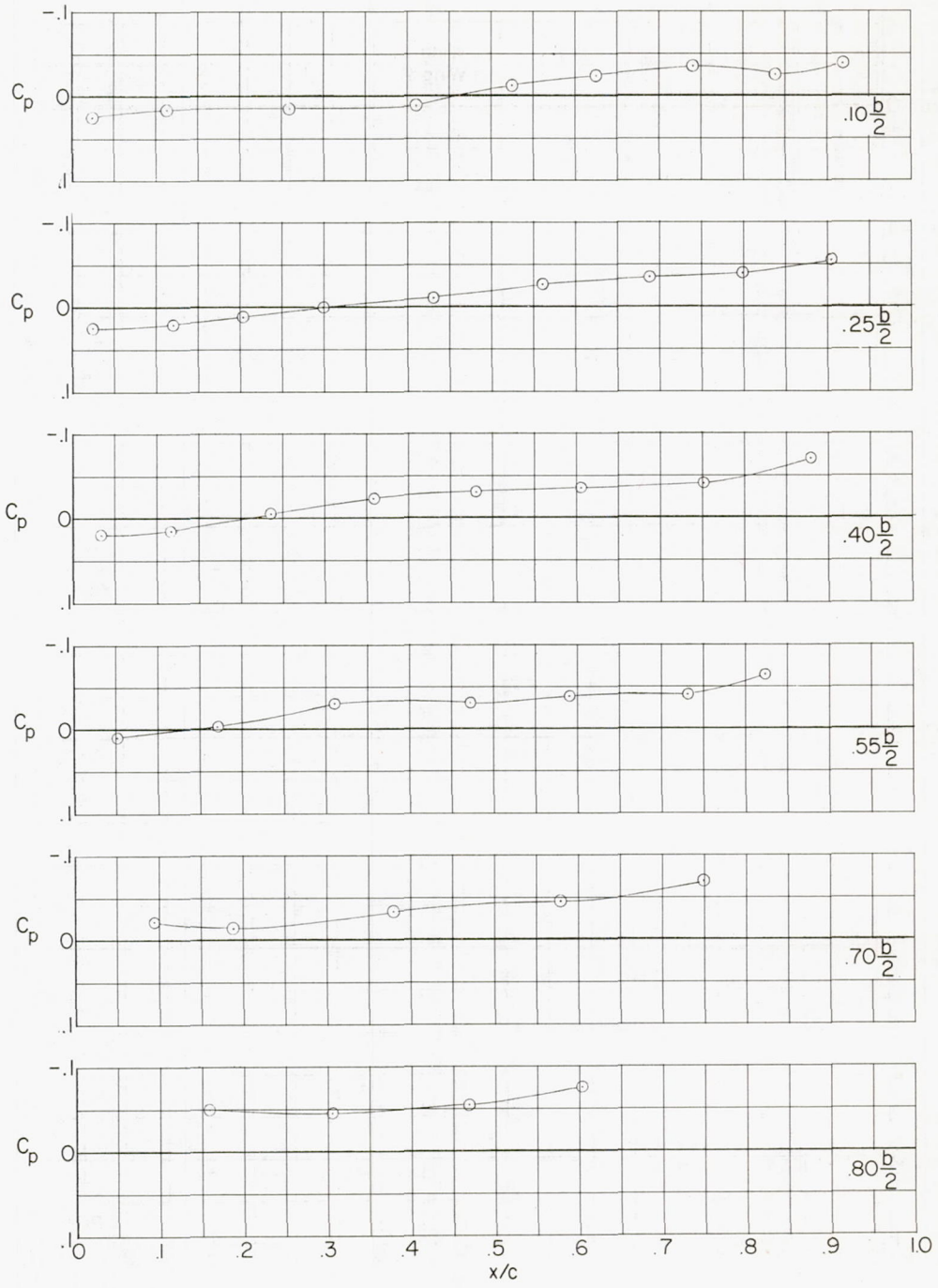
(b) M = 1.94.

Figure 11.- Continued.



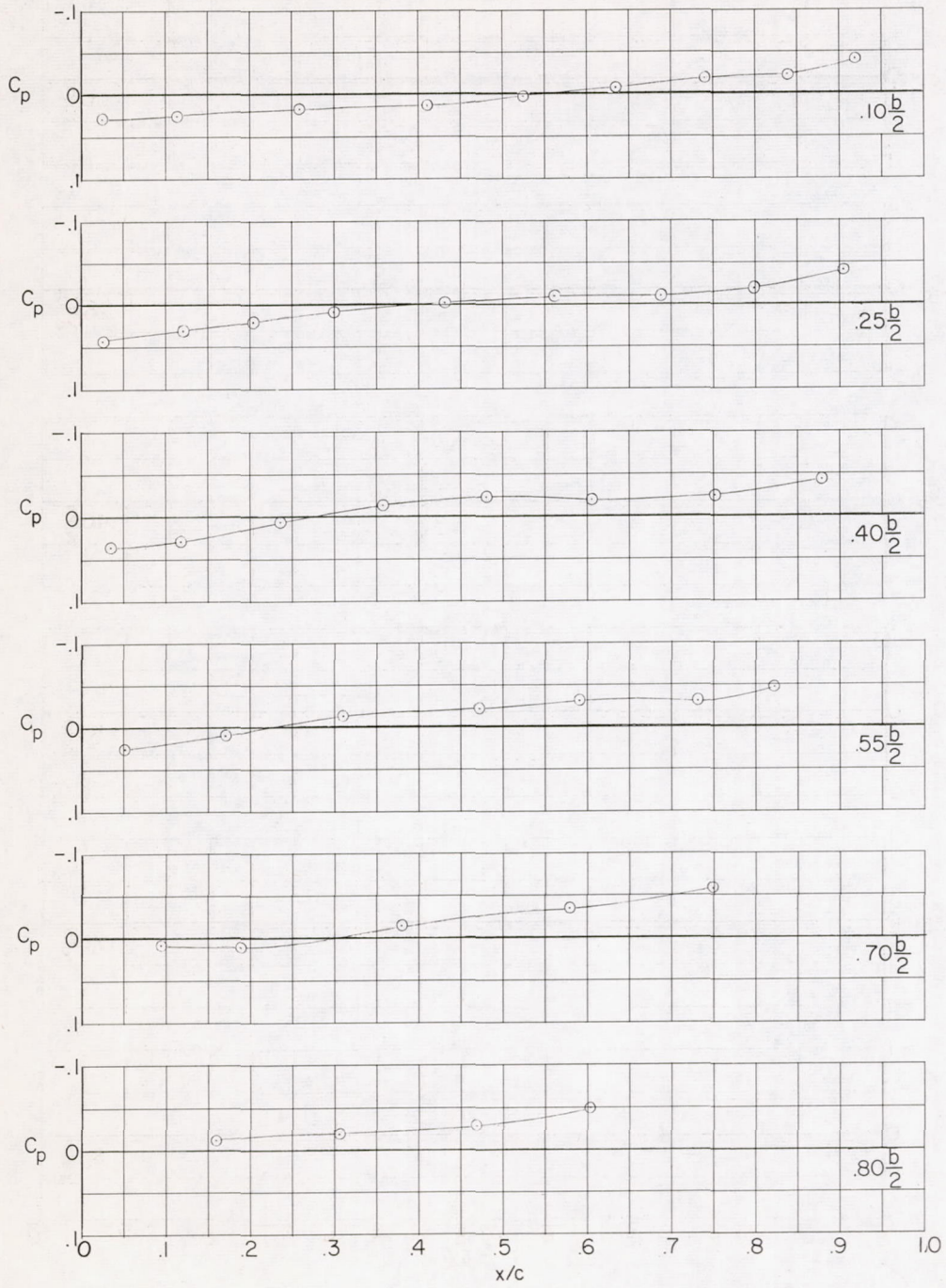
(c) M = 2.41.

Figure 11.- Concluded.



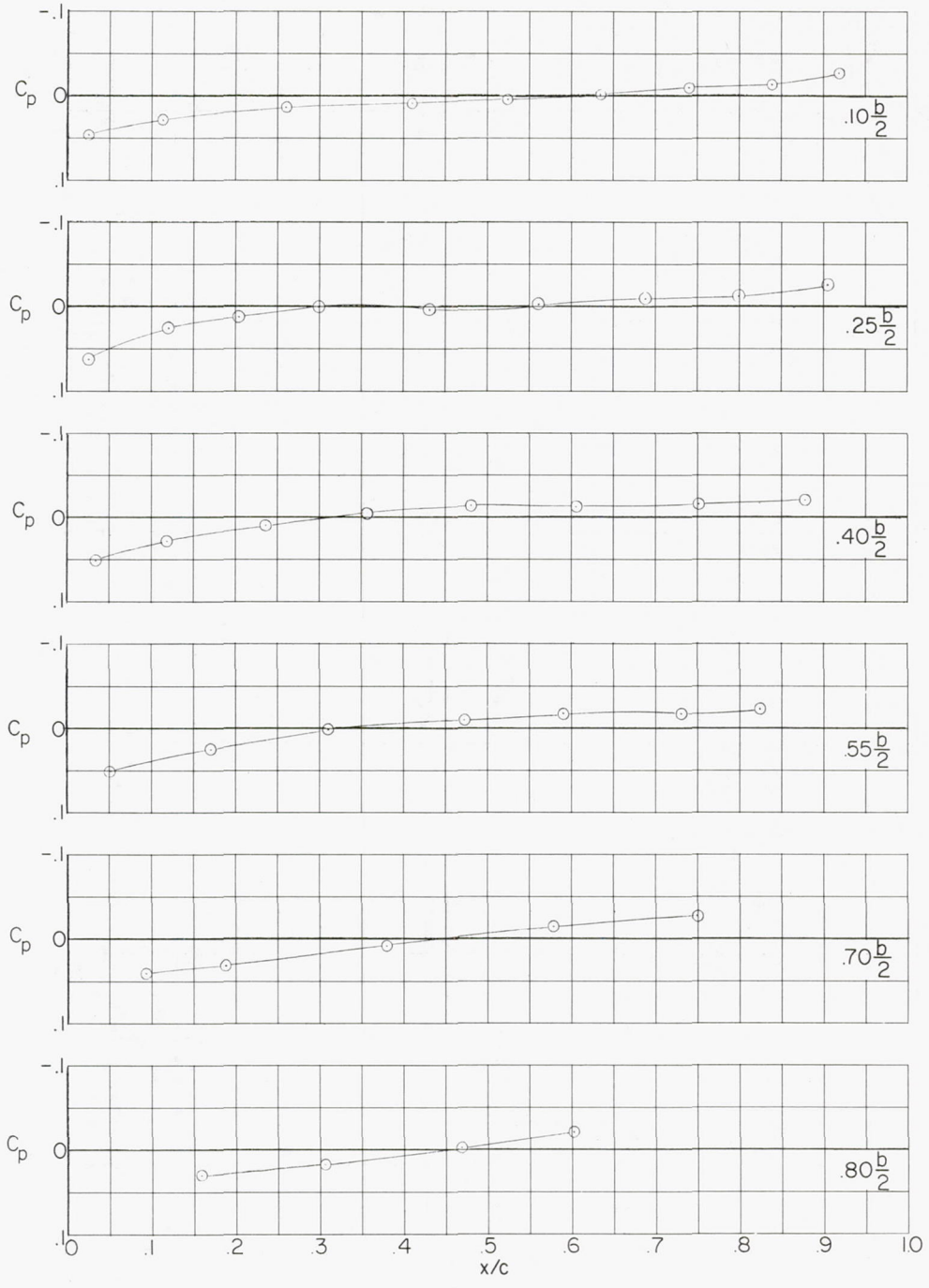
(a) M = 1.62.

Figure 12.- Pressure distributions at $\alpha = 0^{\circ}$. Wing 3.



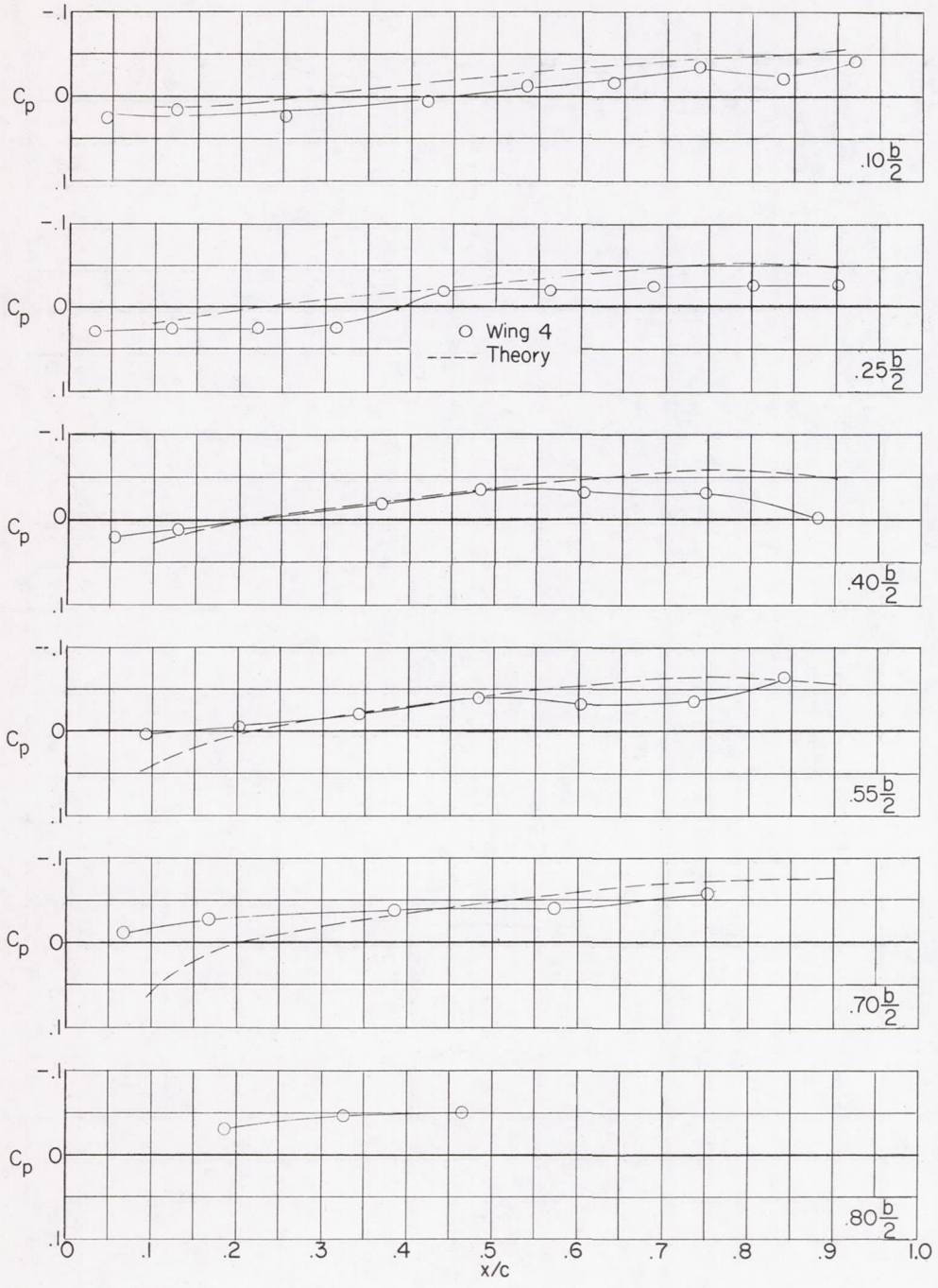
(b) M = 1.94.

Figure 12.- Continued.



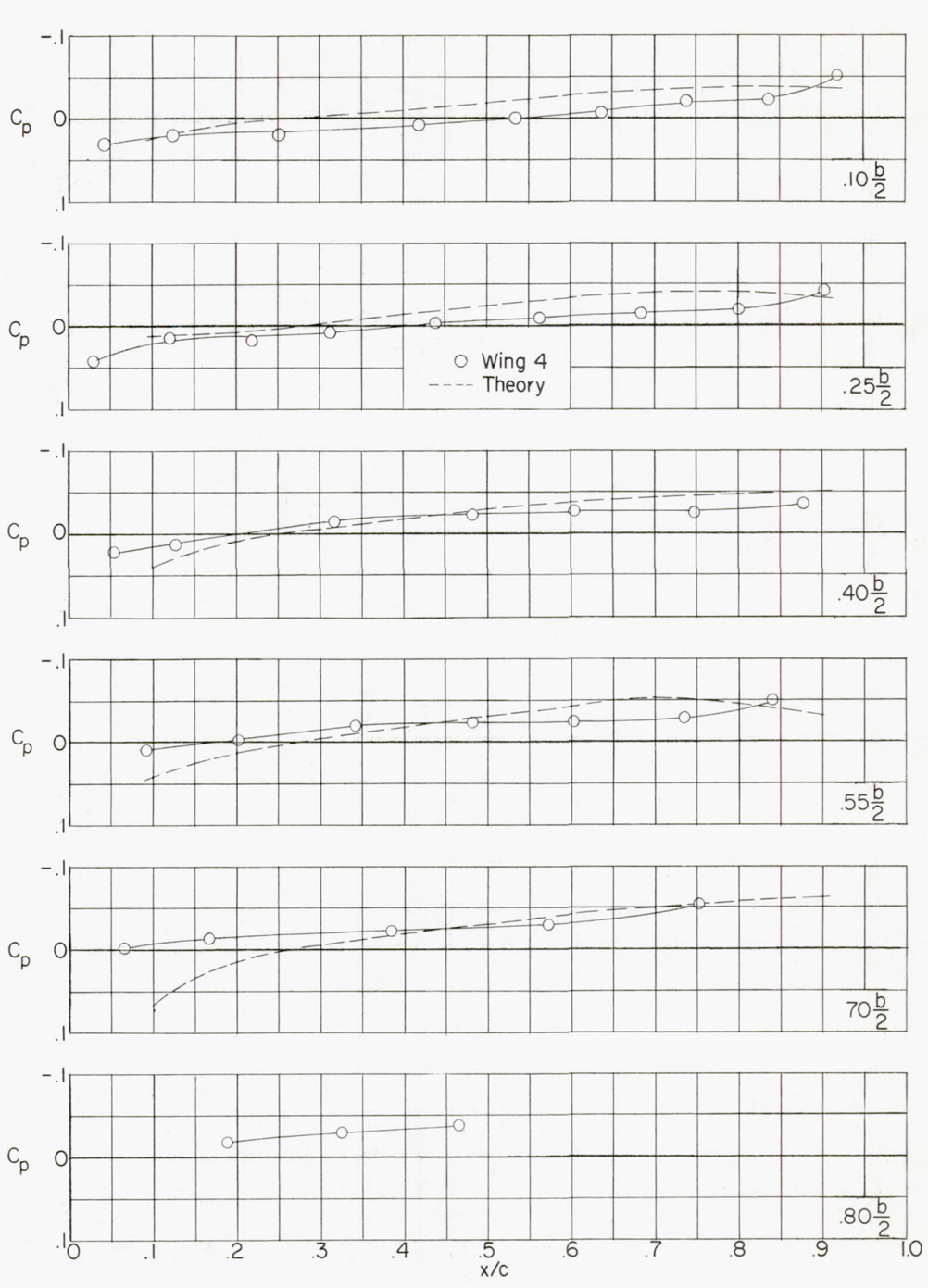
(c) M = 2.41.

Figure 12.- Concluded.



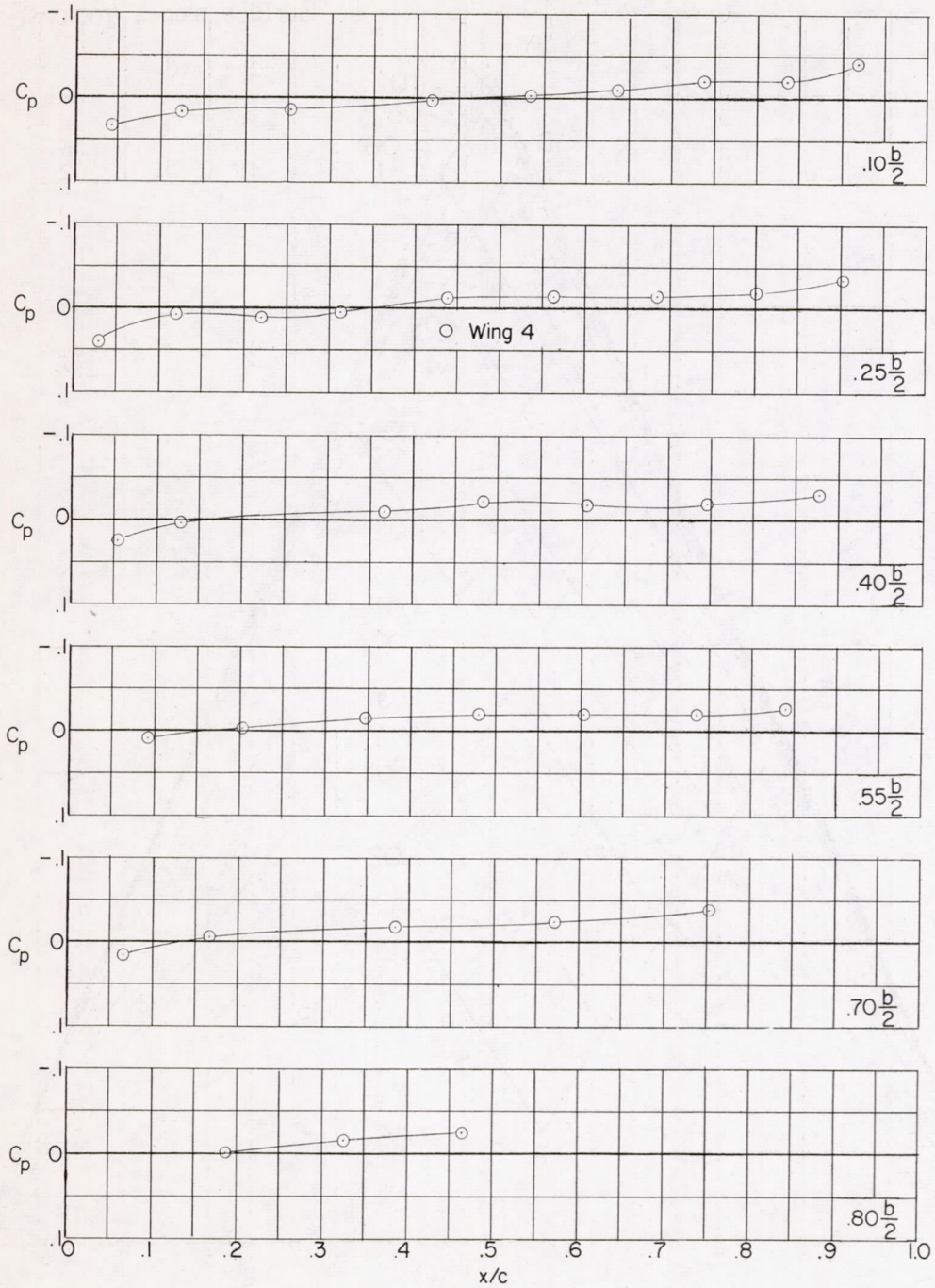
(a) M = 1.62.

Figure 13.- Pressure distributions at $\alpha = 0^{\circ}$. Wing 4.



(b) M = 1.94.

Figure 13.- Continued.



(c) M = 2.41.

Figure 13.- Concluded.

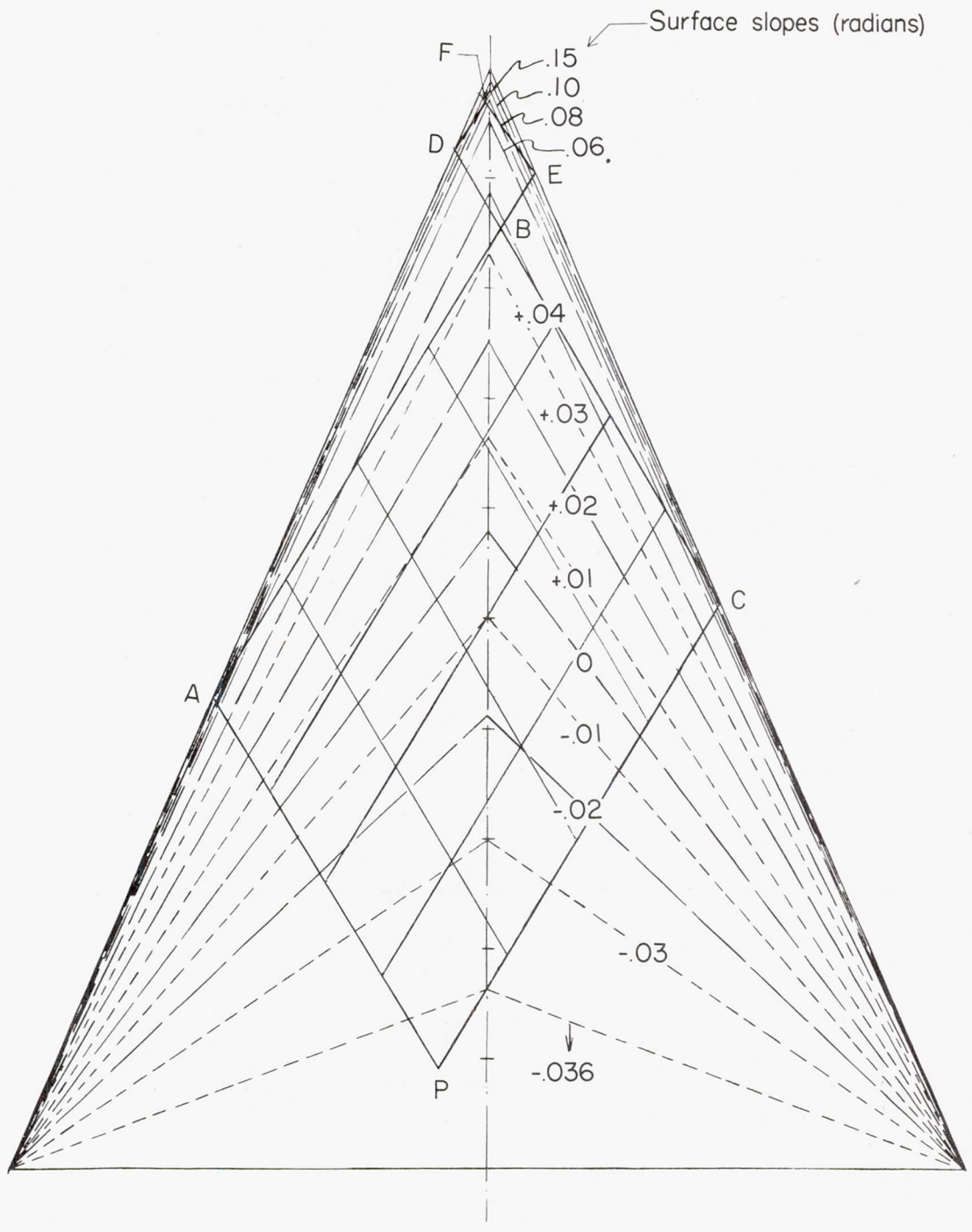


Figure 14.- Sketch of typical graphical layout necessary for computation of theoretical pressure at point P. Wing 4, M = 1.94.

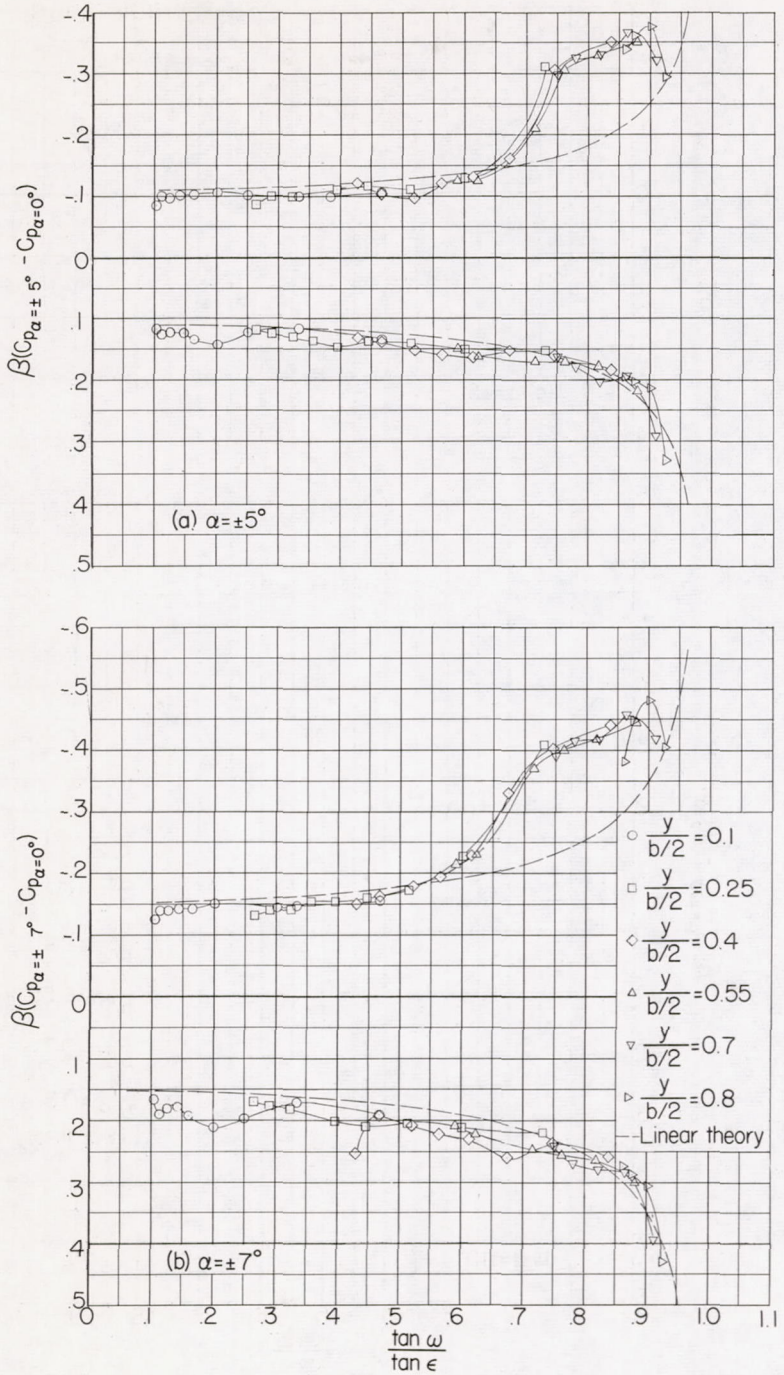


Figure 15.- Pressure distributions as a function of conical ray from wing apex. Wing 1 at M = 1.62.

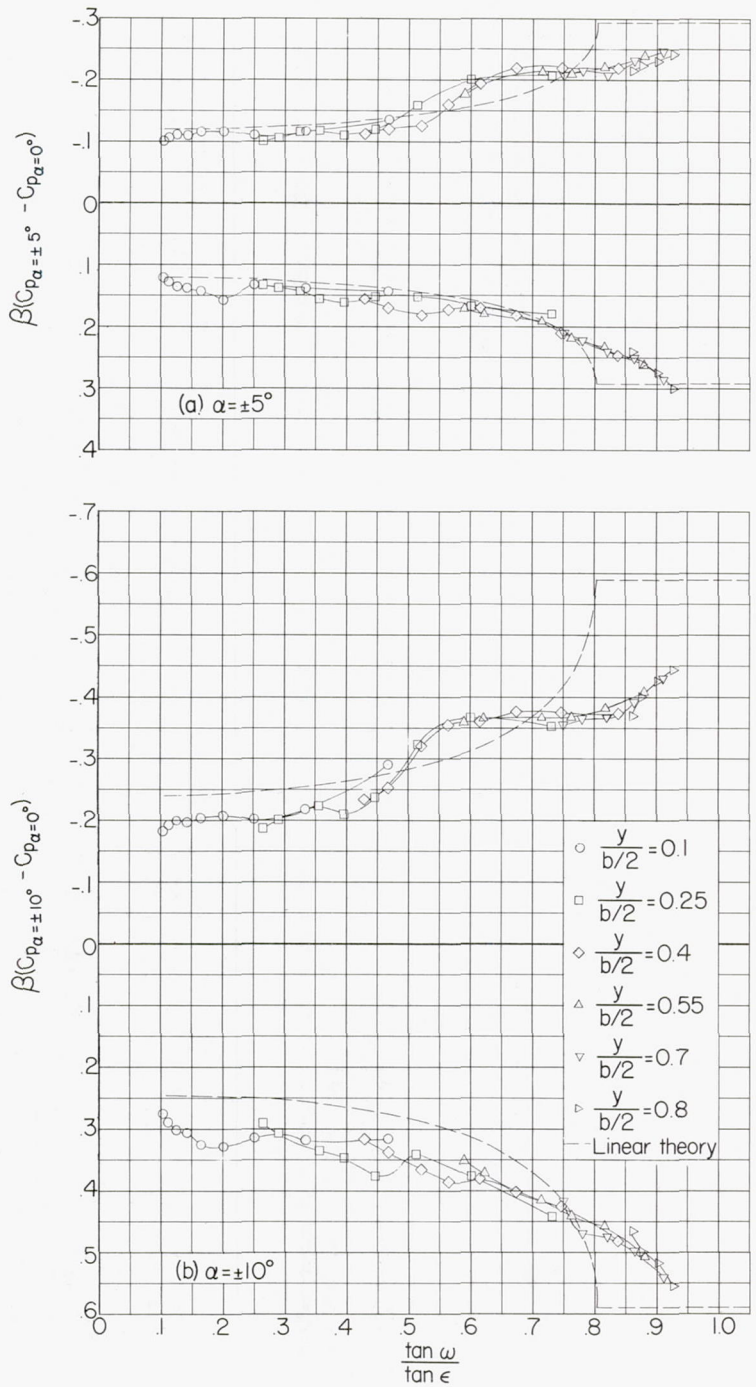


Figure 16.- Pressure distributions as a function of conical ray from wing apex. Wing 1 at M = 1.94.

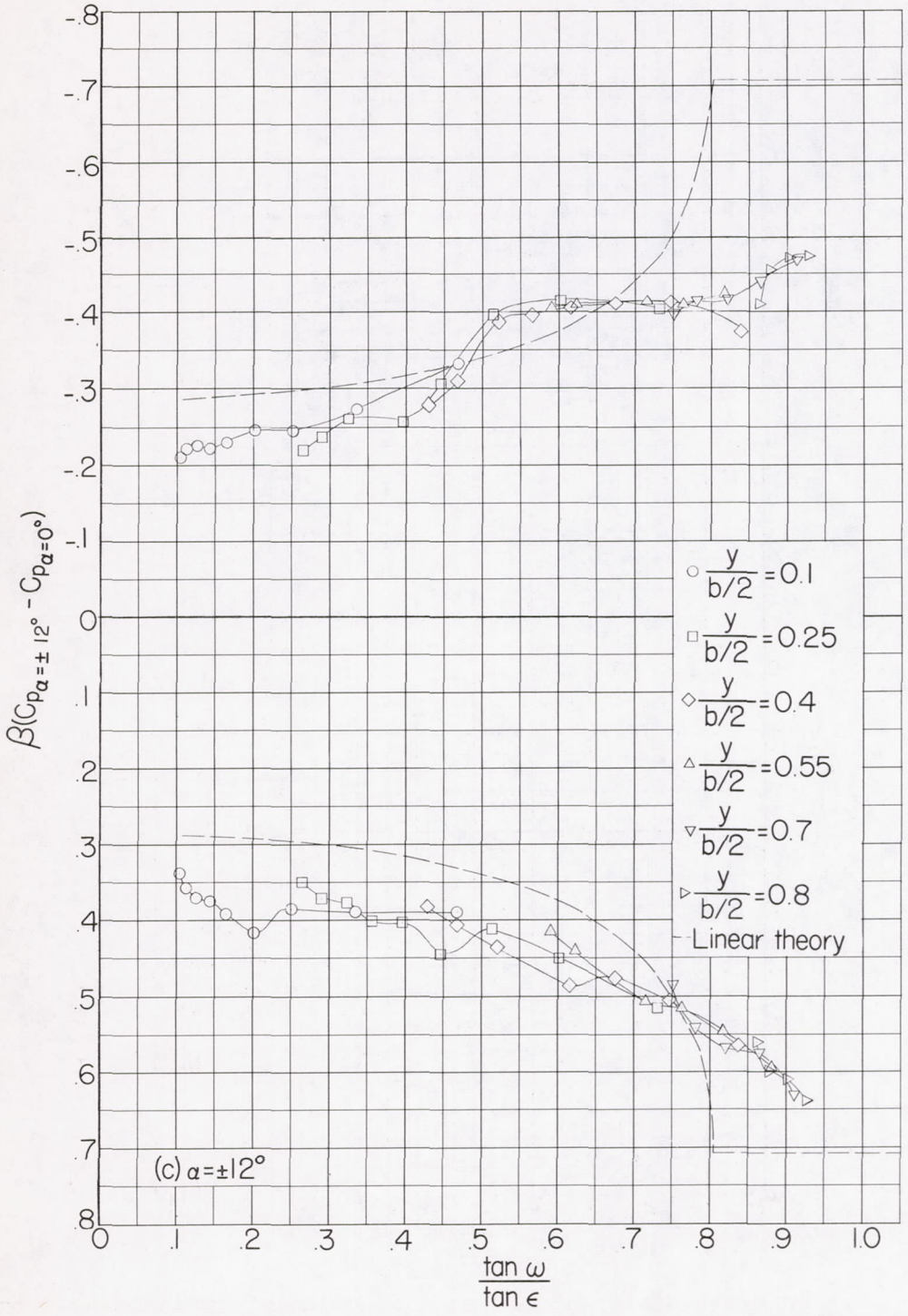


Figure 16.- Concluded.

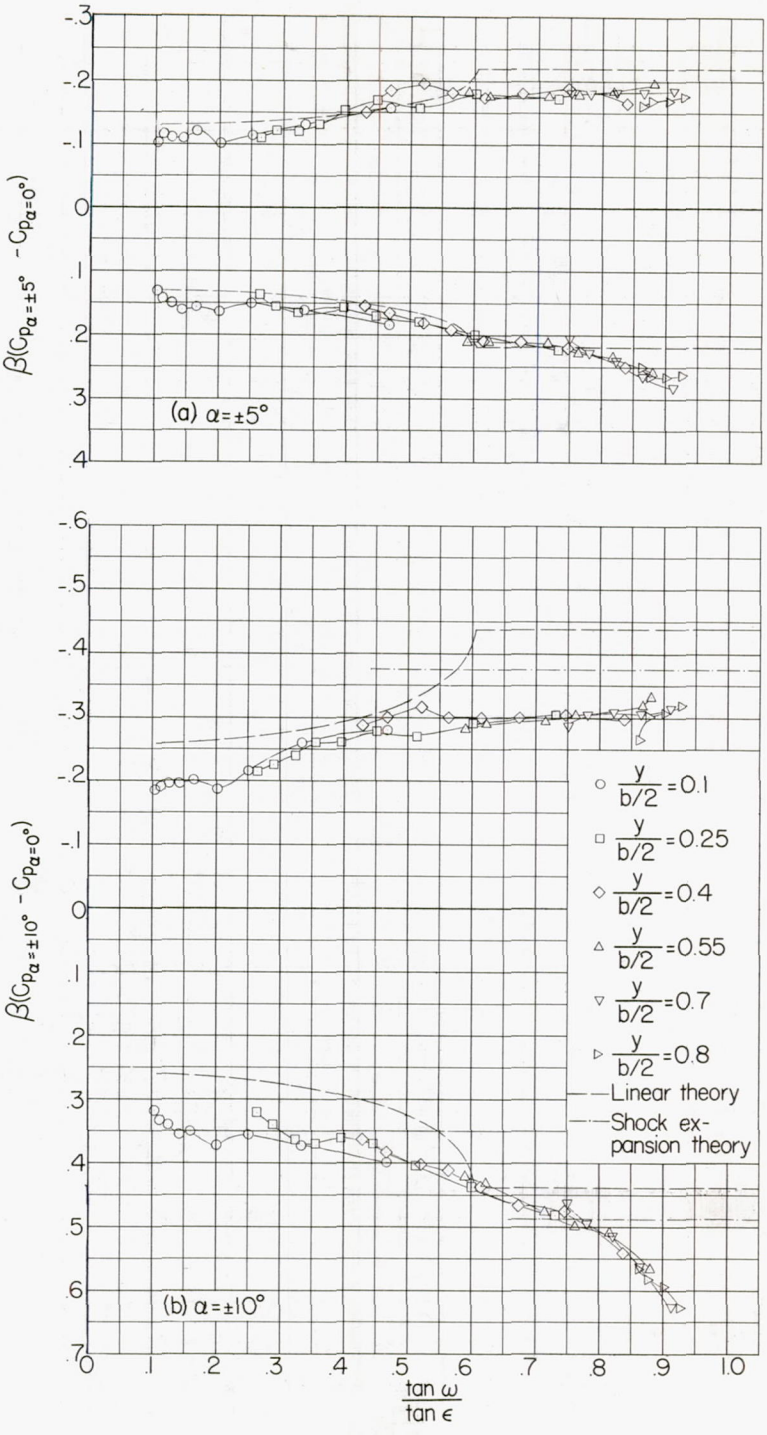


Figure 17.- Pressure distributions as a function of conical ray from wing apex. Wing 1 at M = 2.41.

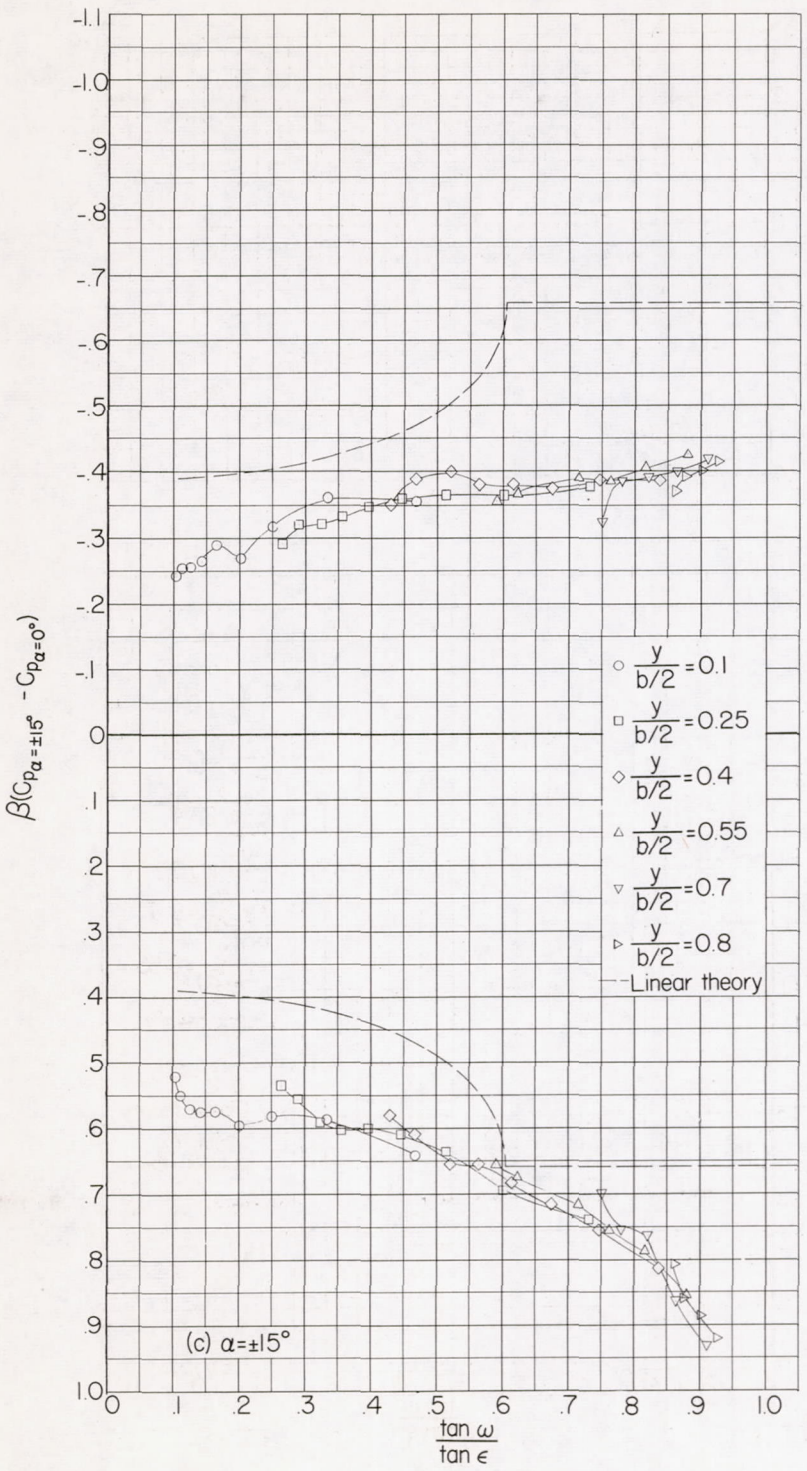


Figure 17.- Continued.

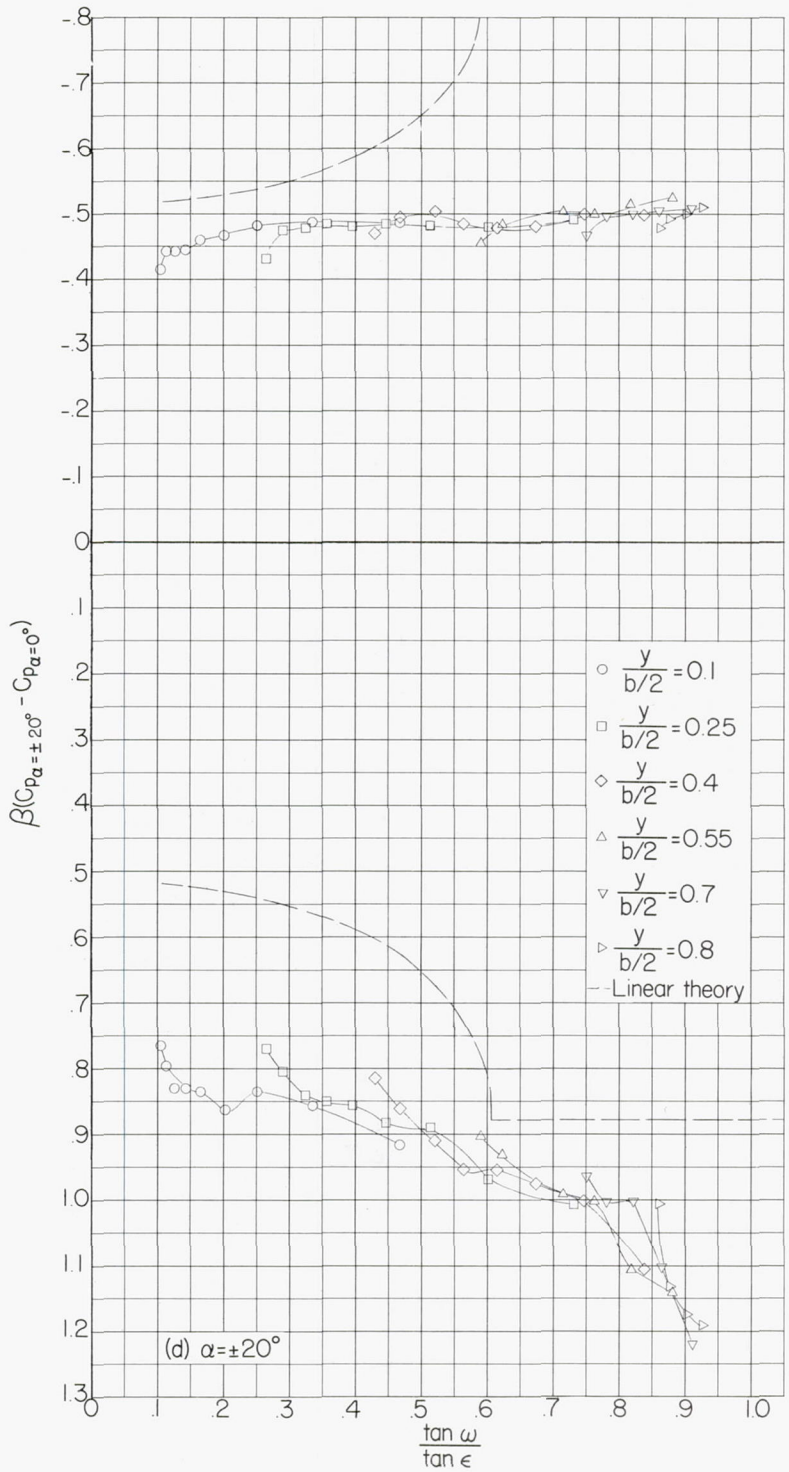


Figure 17.- Concluded.

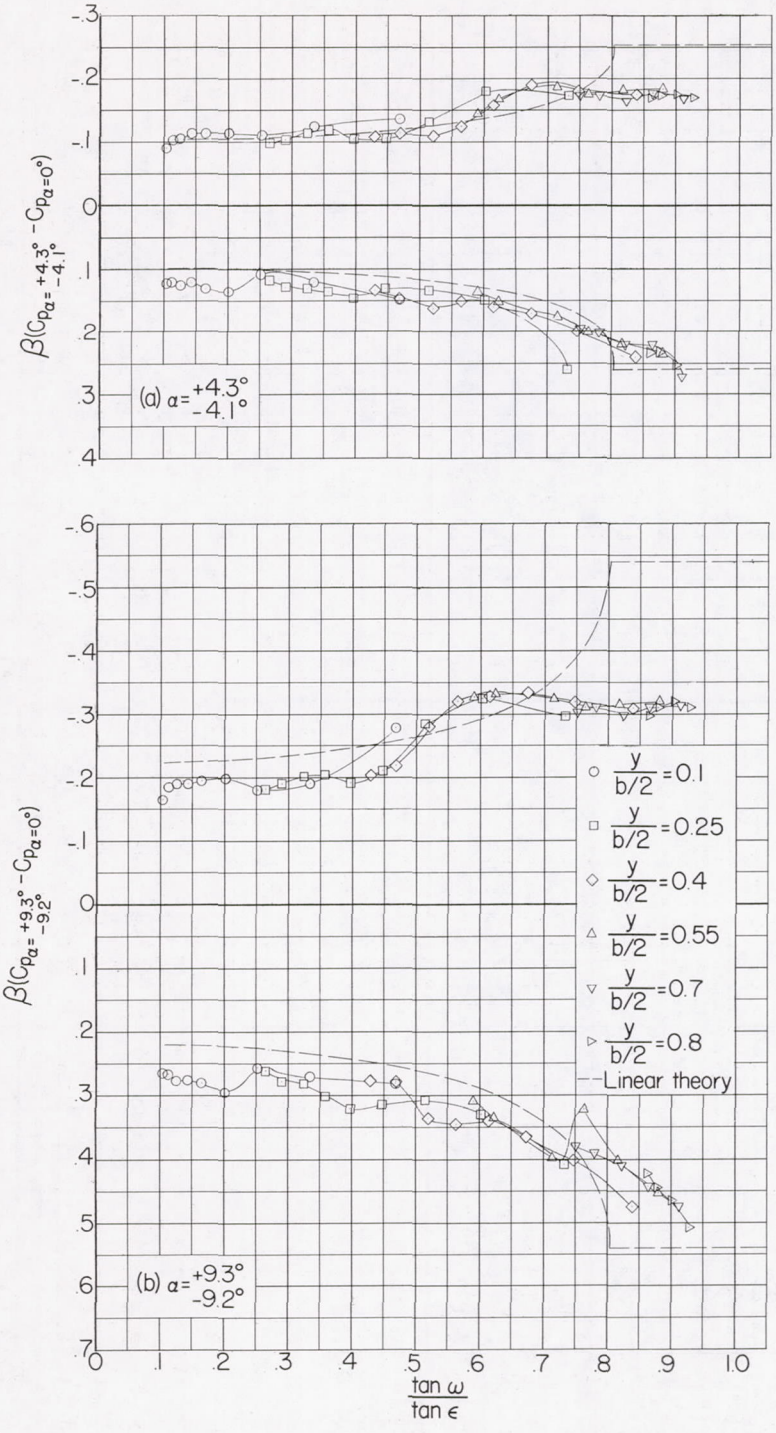


Figure 18.- Pressure distributions as a function of conical ray from wing apex. Wing 1 with leading-edge extension at M = 1.94.

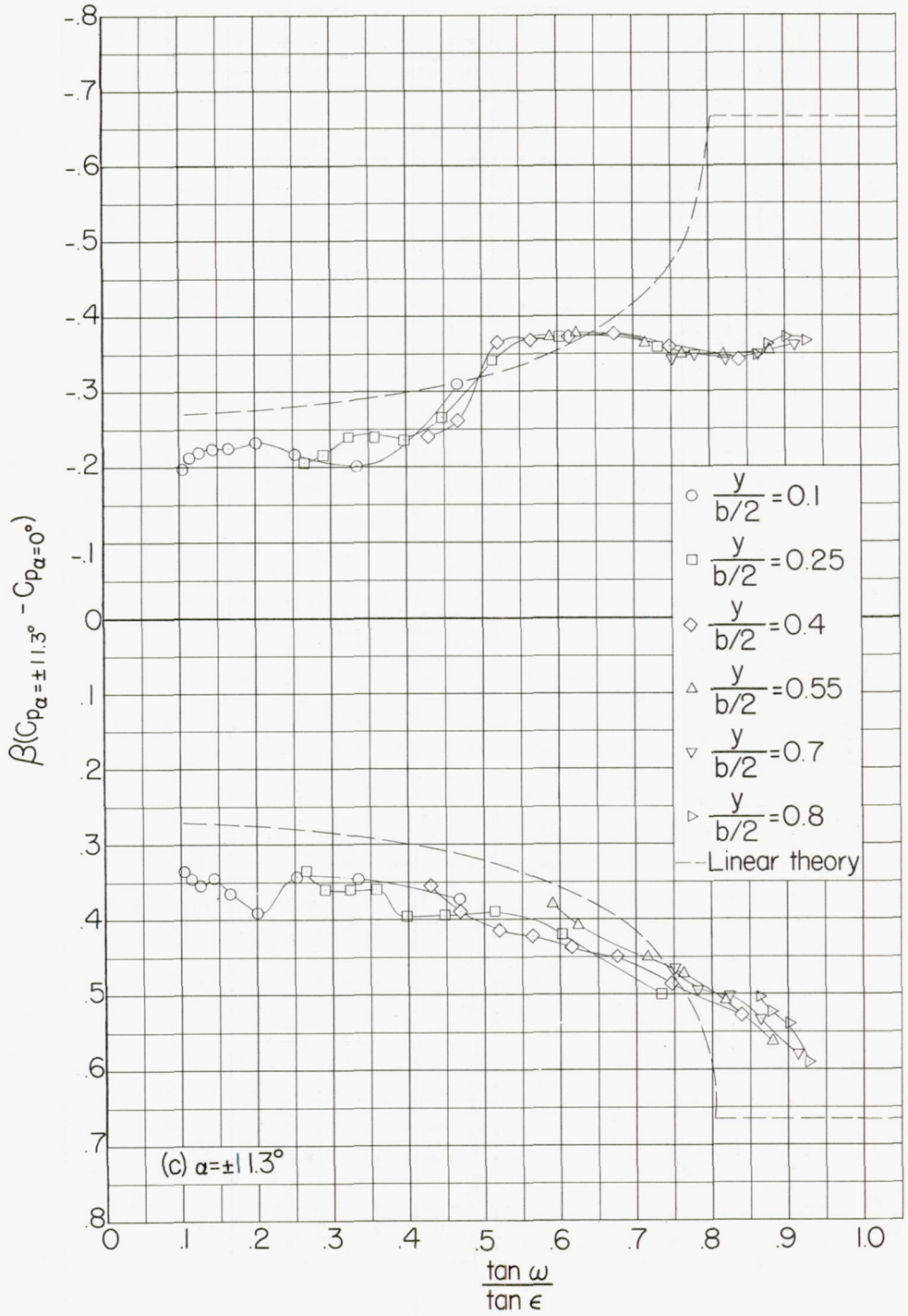


Figure 18.- Concluded.

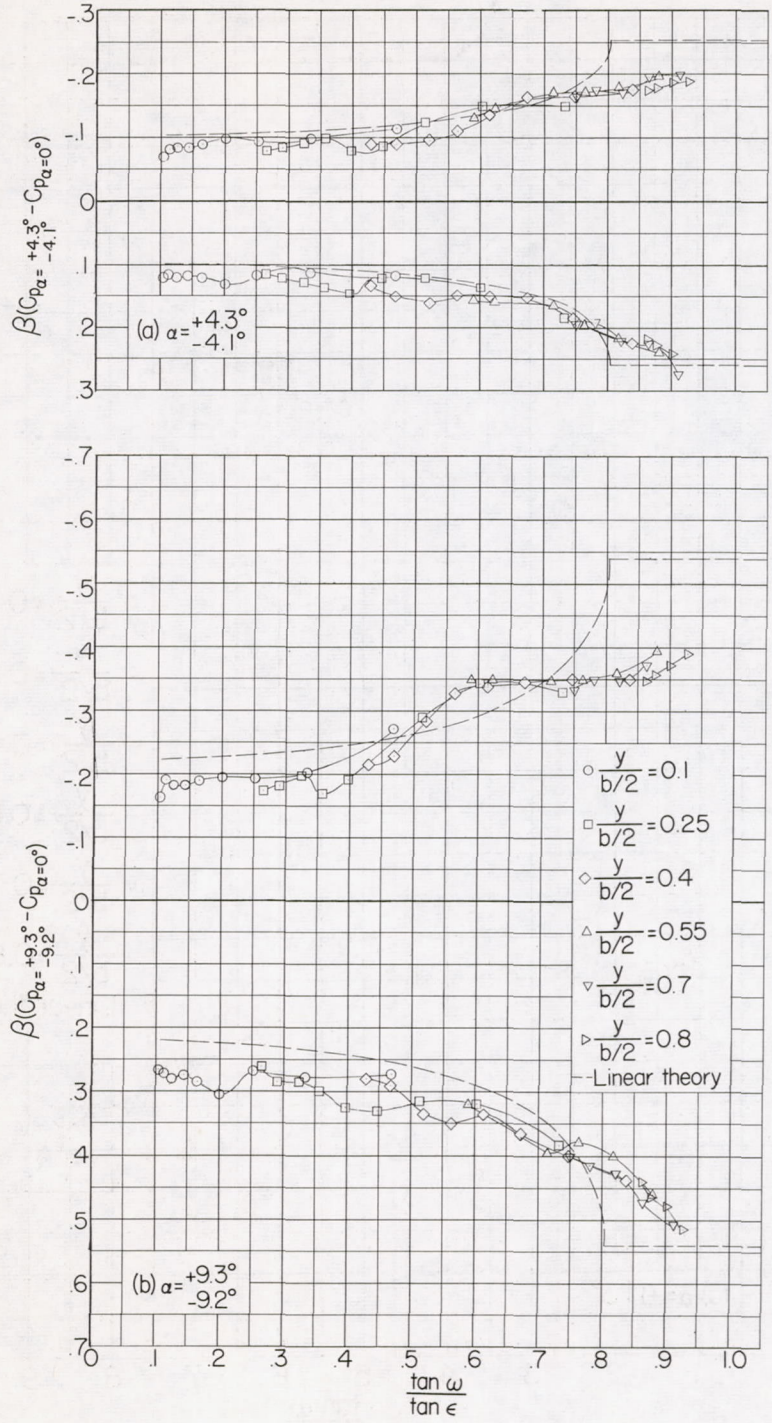


Figure 19.- Pressure distributions as a function of conical ray from wing apex. Wing 1 without leading-edge extension at M = 1.94.

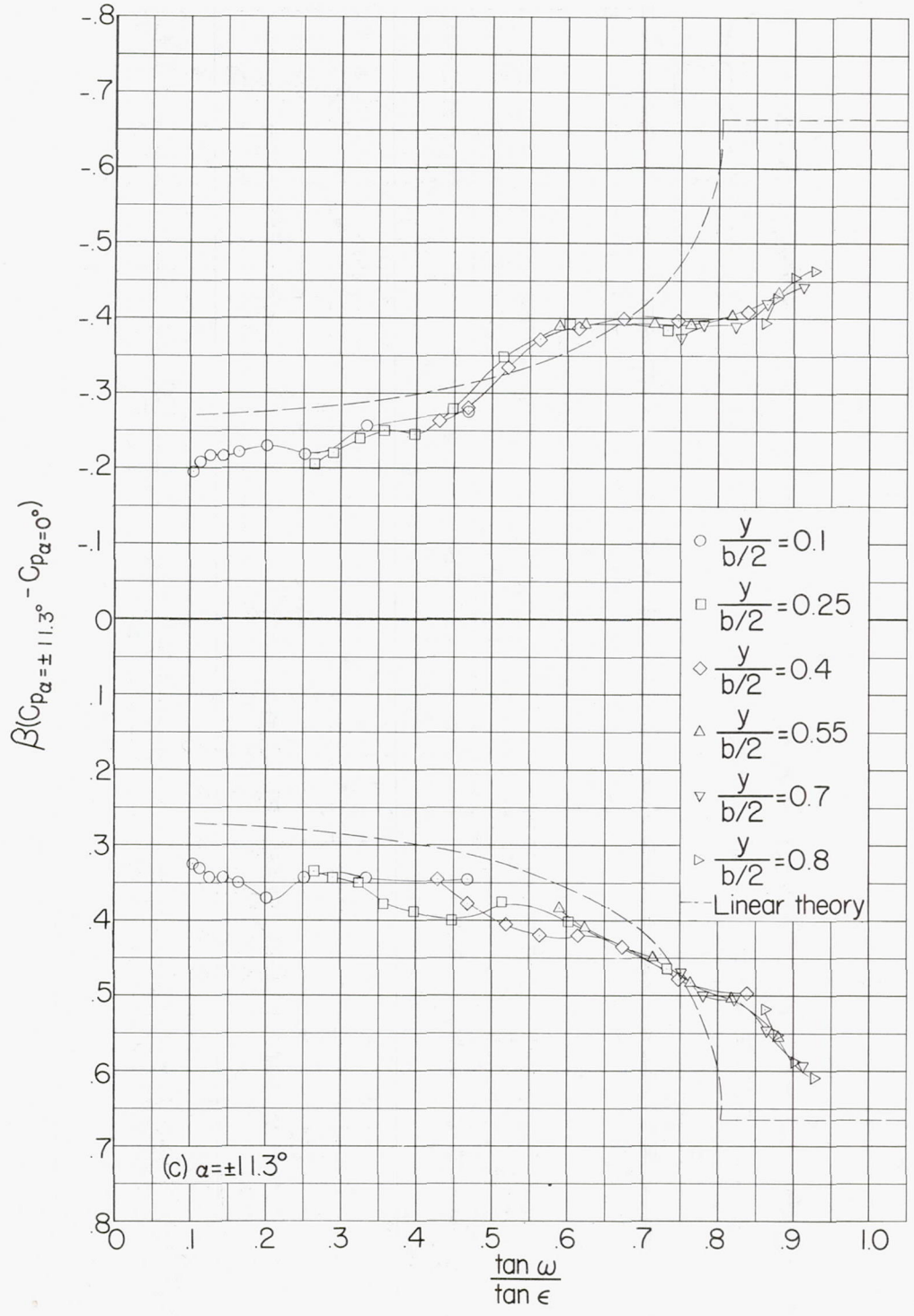


Figure 19.- Concluded.

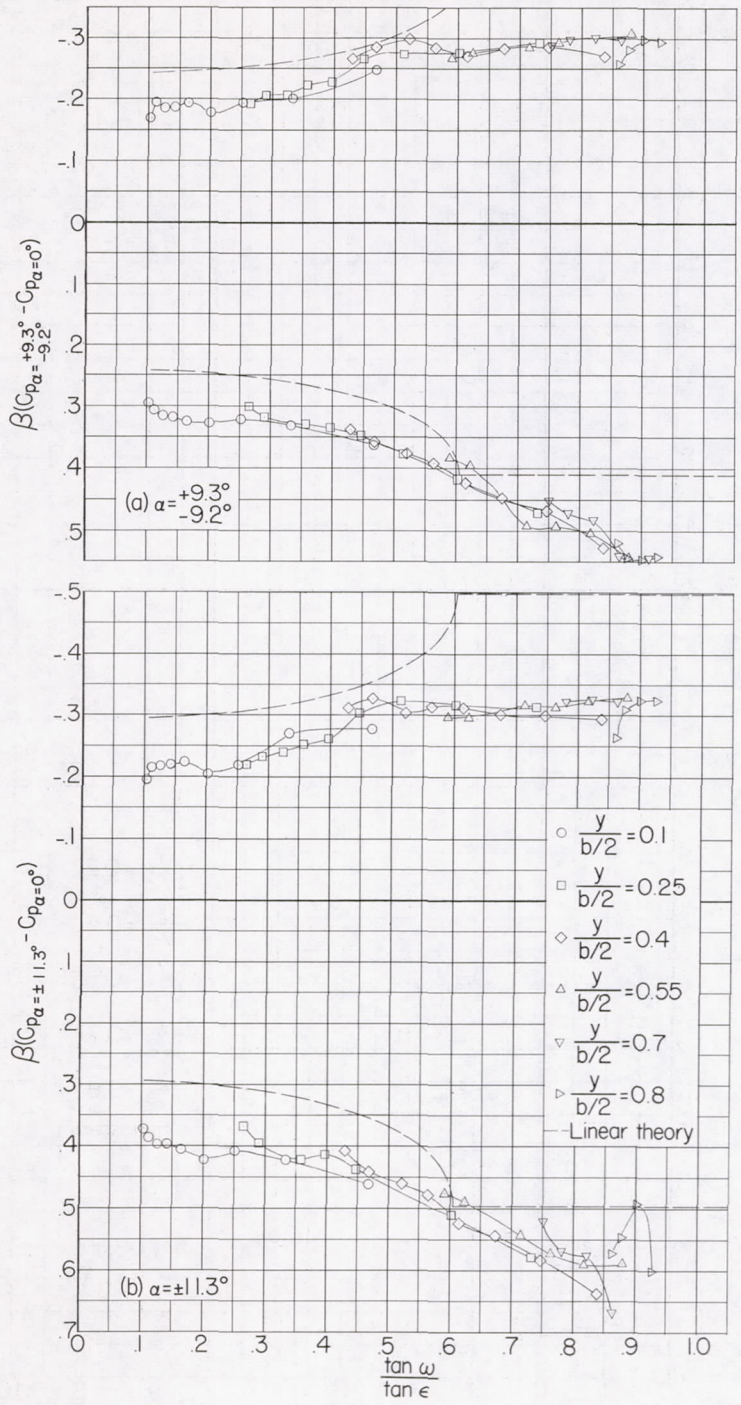


Figure 20.- Pressure distributions as a function of conical ray from wing apex. Wing 1 with leading-edge extension at M = 2.41.

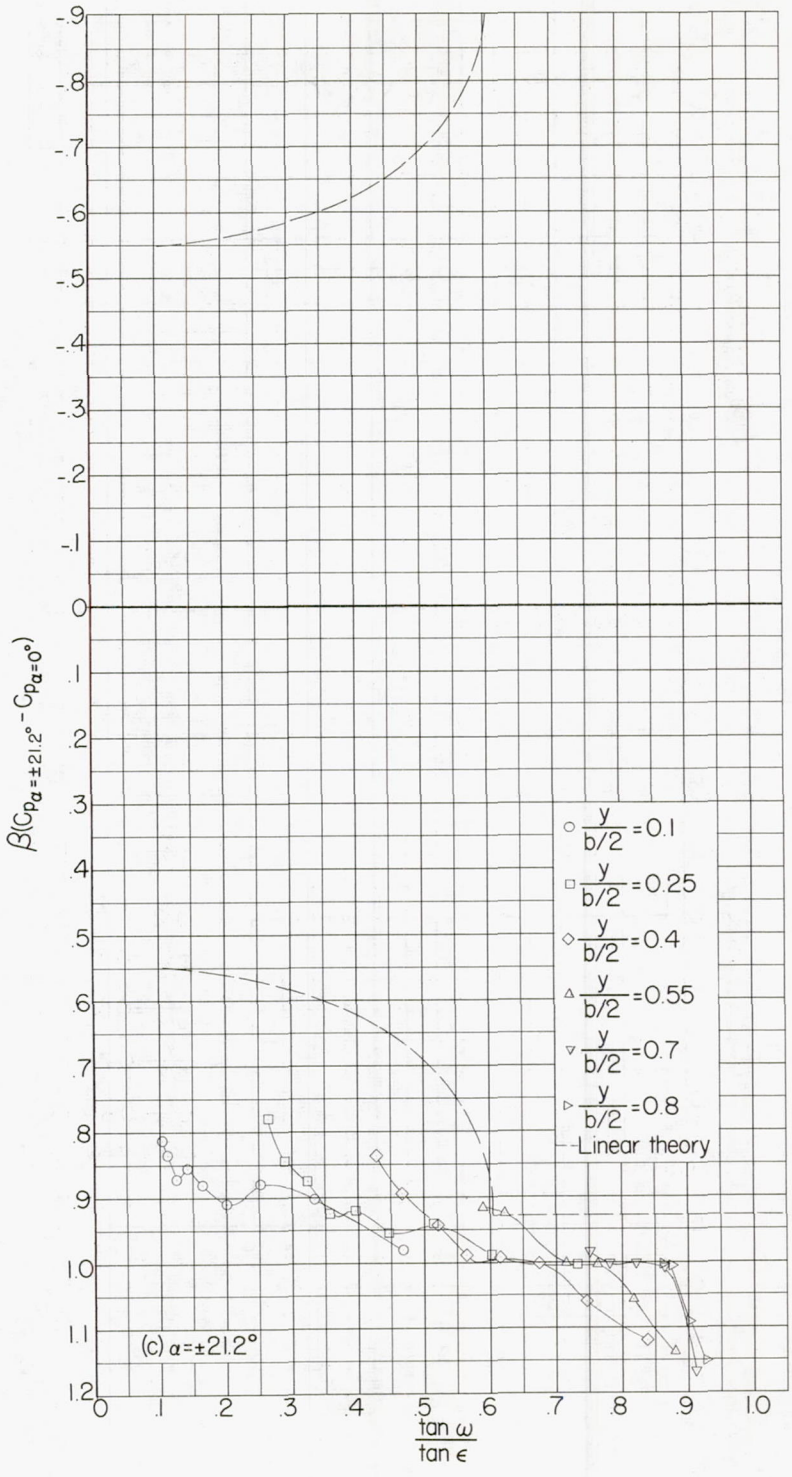


Figure 20.- Concluded.

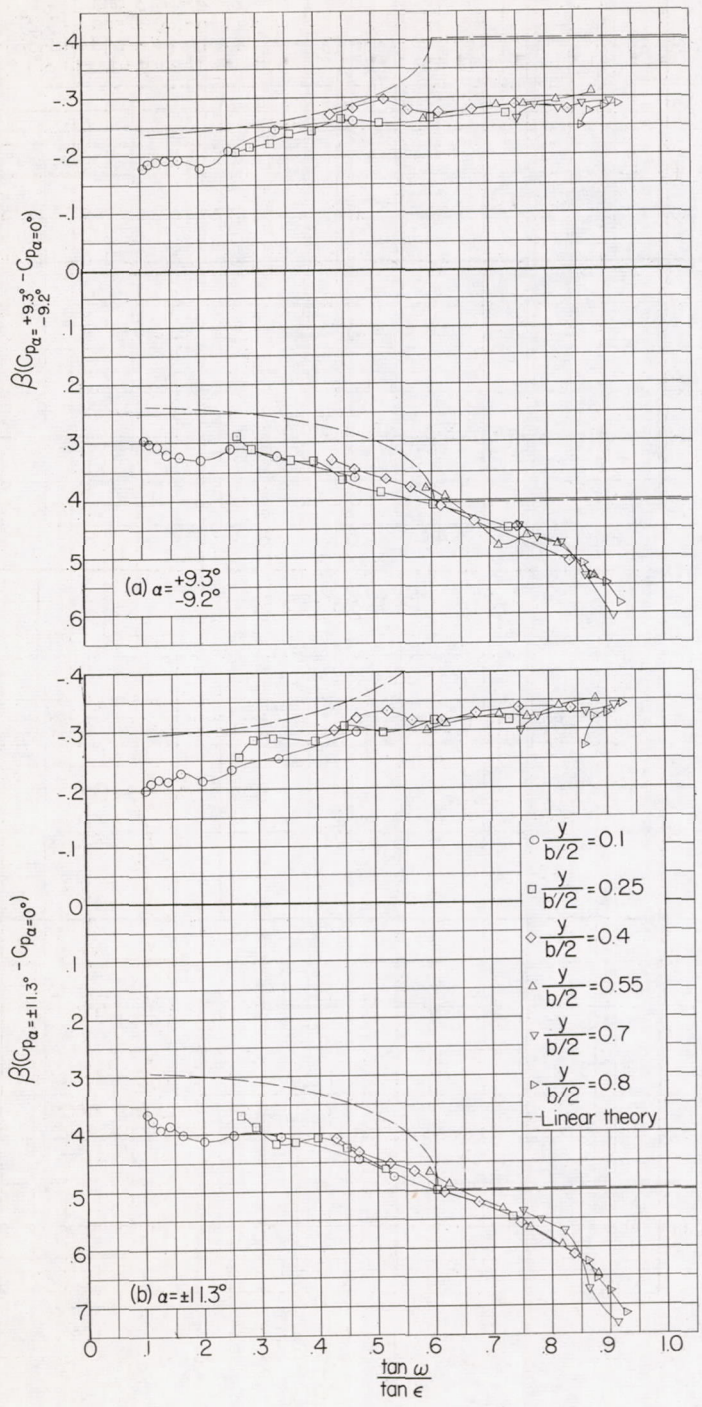
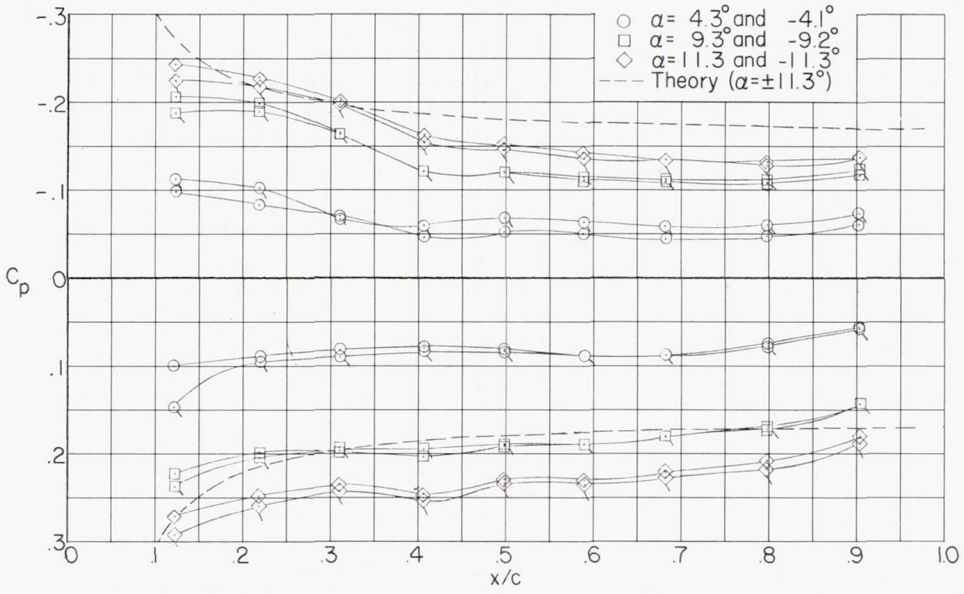


Figure 21.- Pressure distributions as a function of conical ray from wing apex. Wing 1 without leading-edge extension at M = 2.41.



(a) $y/\frac{b}{2}=0.25$



(b) $y/\frac{b}{2}=0.55$

Figure 22.- Pressure distributions with and without leading-edge extensions. Wing 1 at M = 1.94. (Flagged symbols denote data with leading-edge extension.)

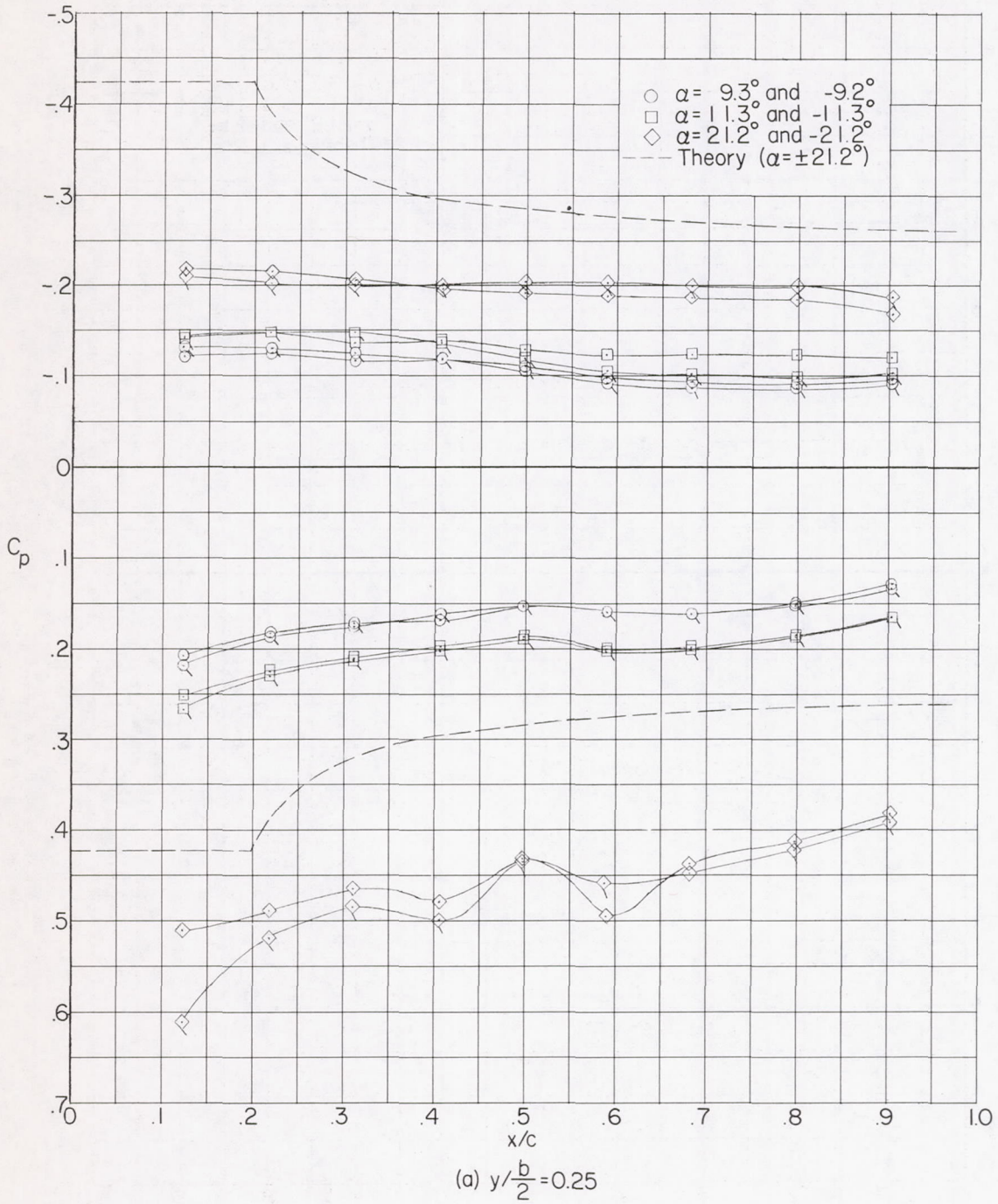


Figure 23.- Pressure distributions with and without leading-edge extensions. Wing 1 at M = 2.41. (Flagged symbols denote data with leading-edge extension.)

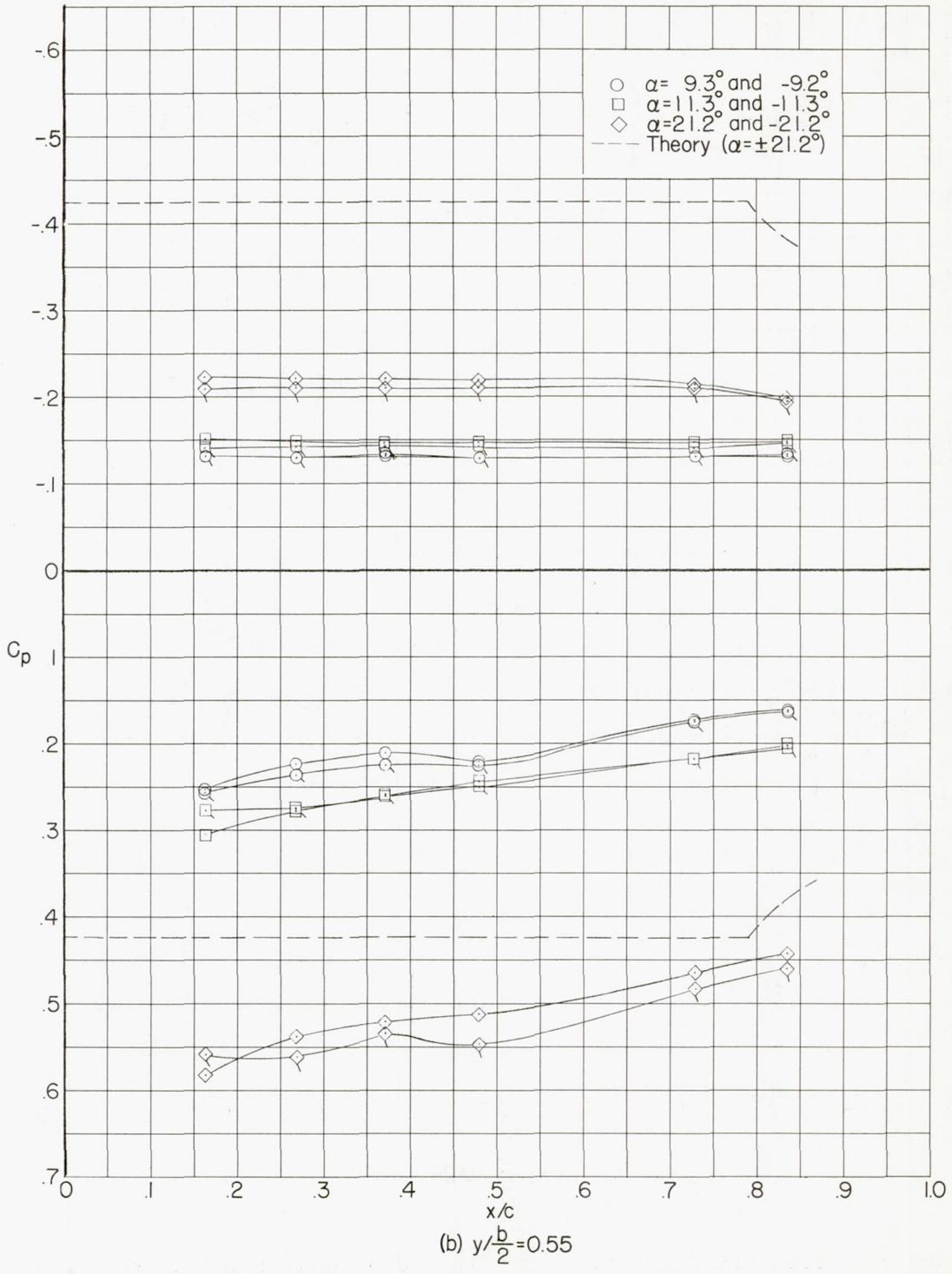


Figure 23.- Concluded.

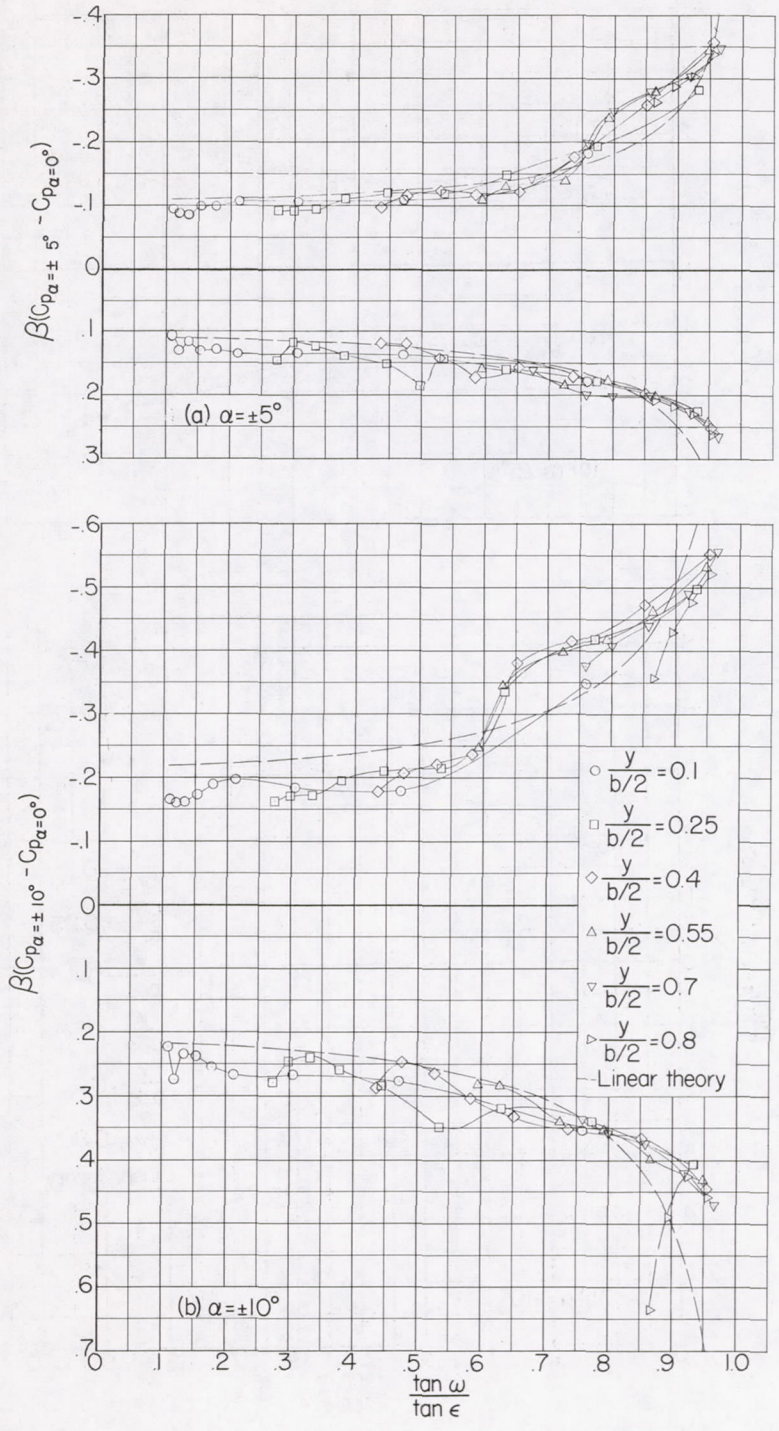


Figure 24.- Pressure distributions as a function of conical ray from wing apex. Wing 2 at M = 1.62.

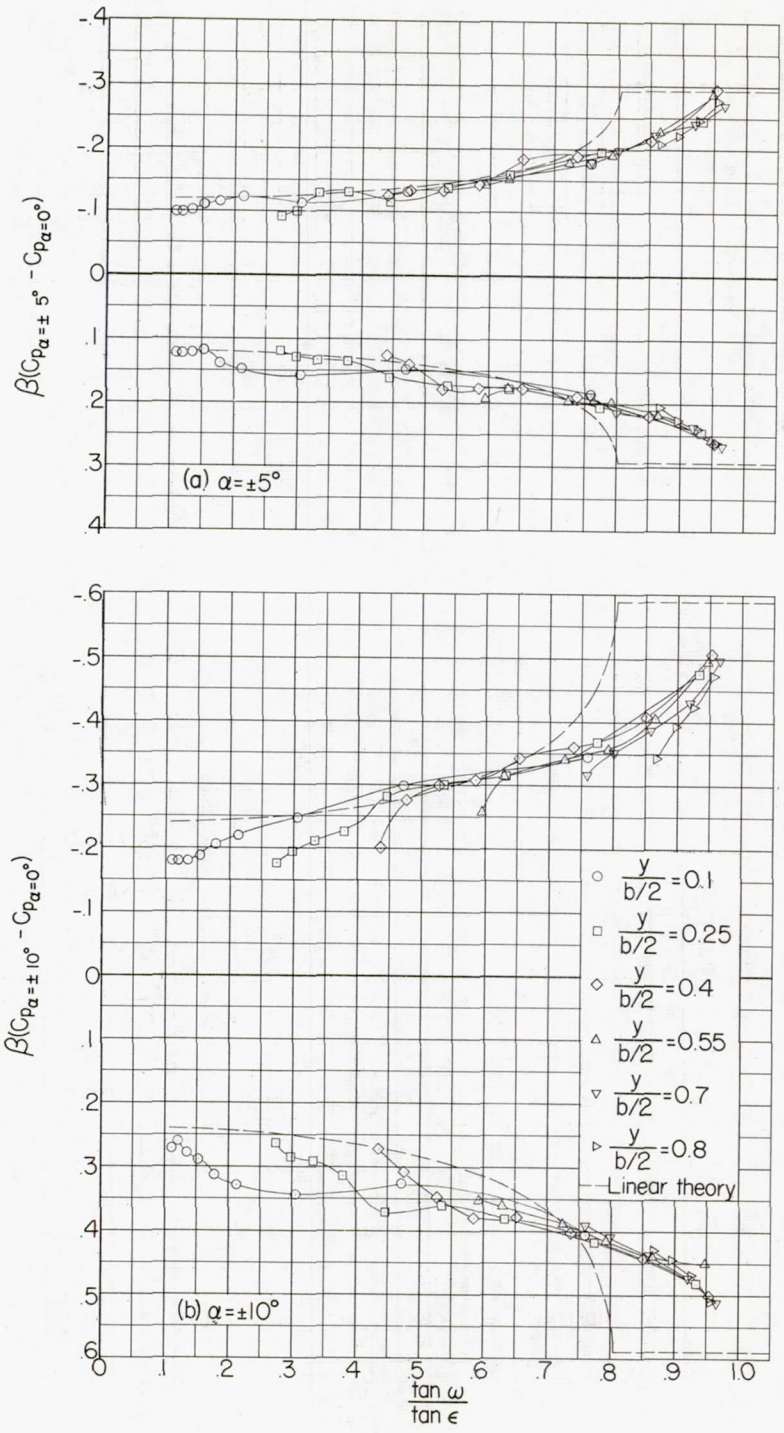


Figure 25.- Pressure distributions as a function of conical ray from wing apex. Wing 2 at M = 1.94.

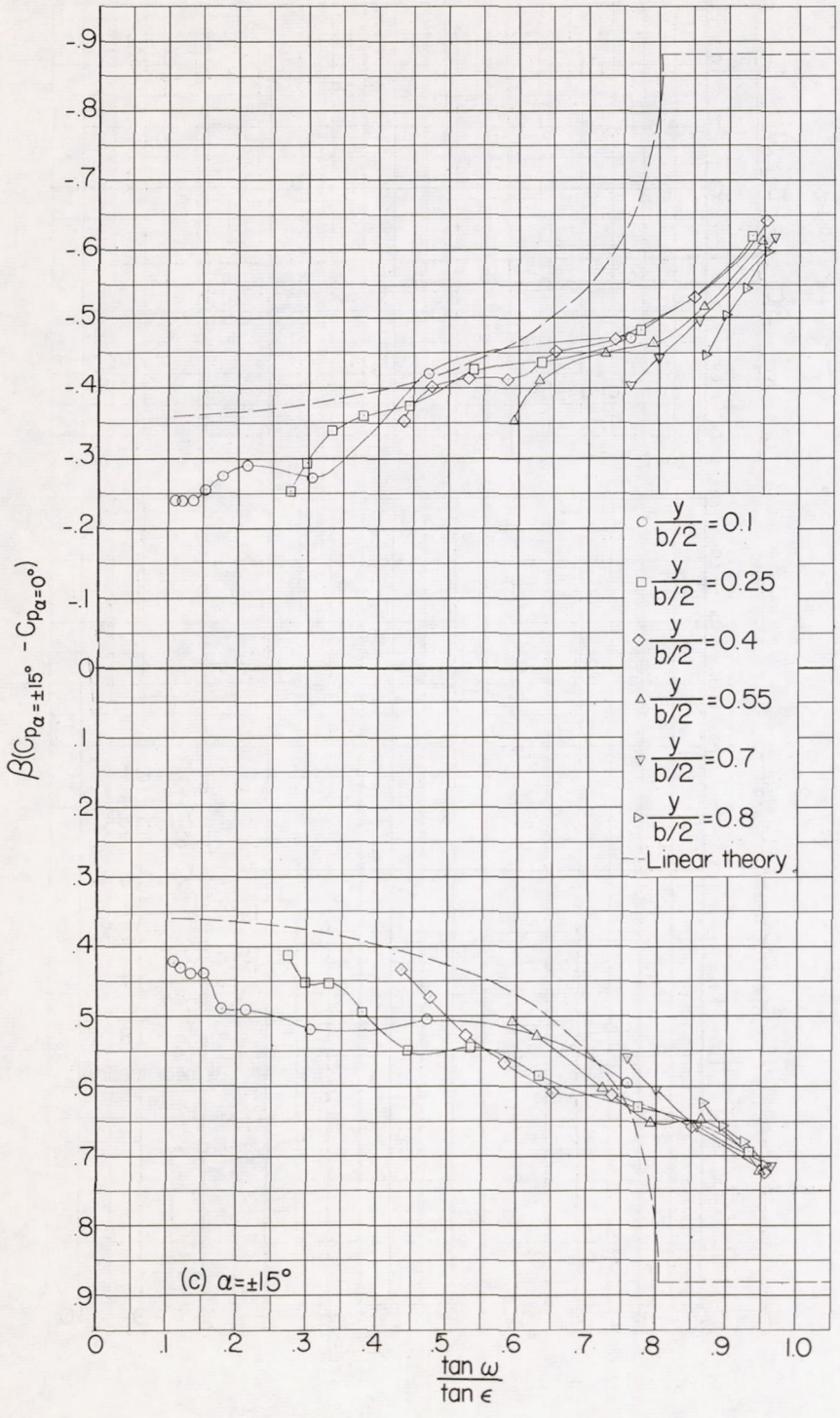


Figure 25.- Concluded.

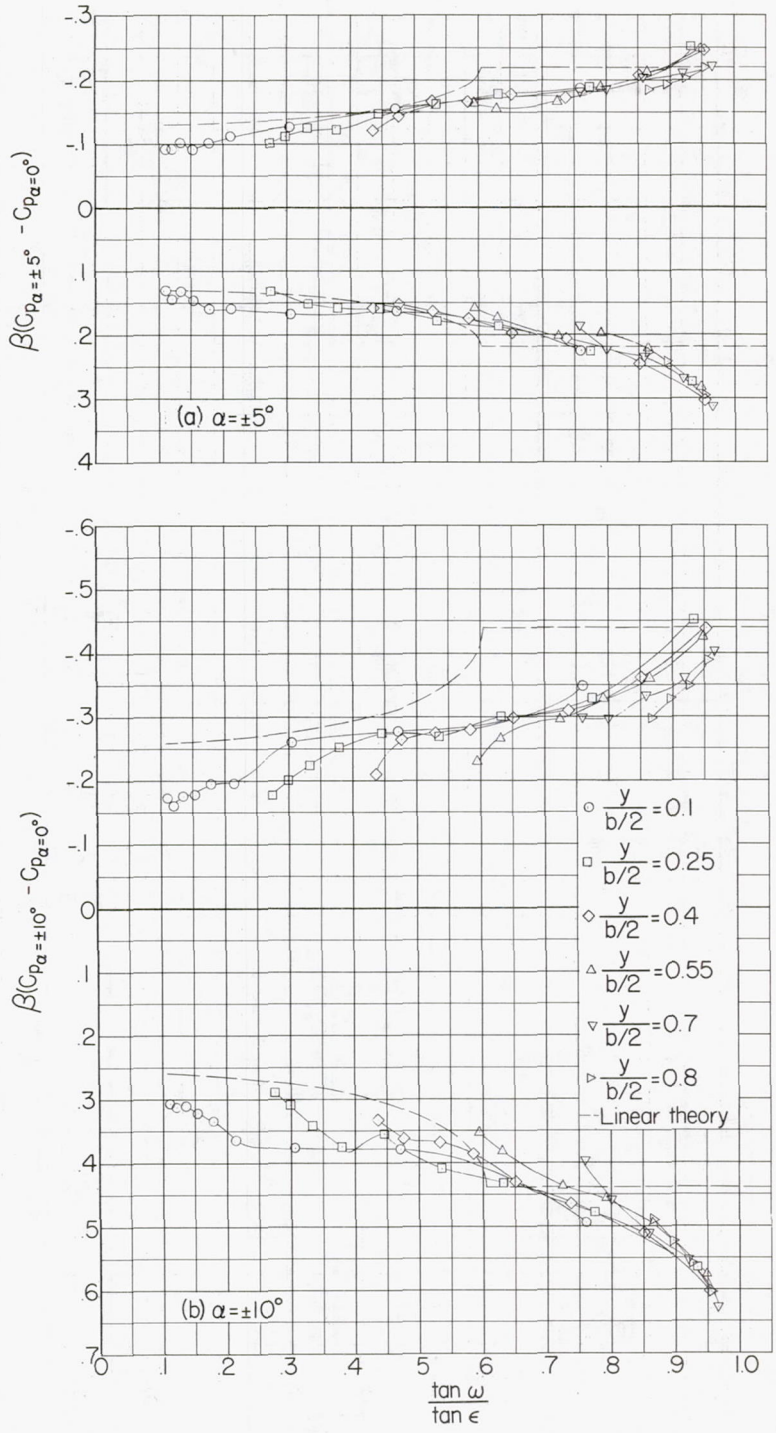


Figure 26.- Pressure distributions as a function of conical ray from wing apex. Wing 2 at M = 2.41.

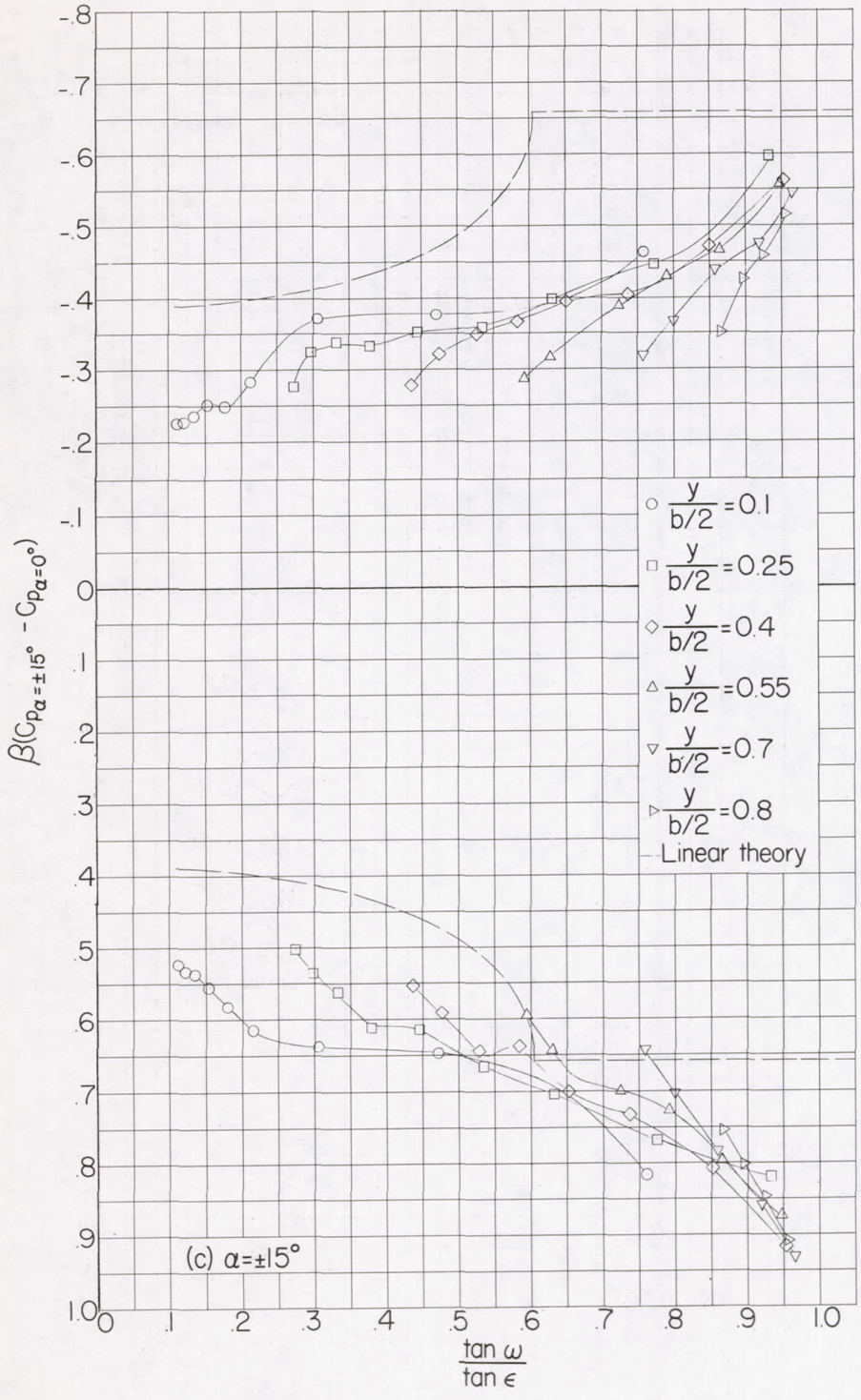


Figure 26.- Continued.

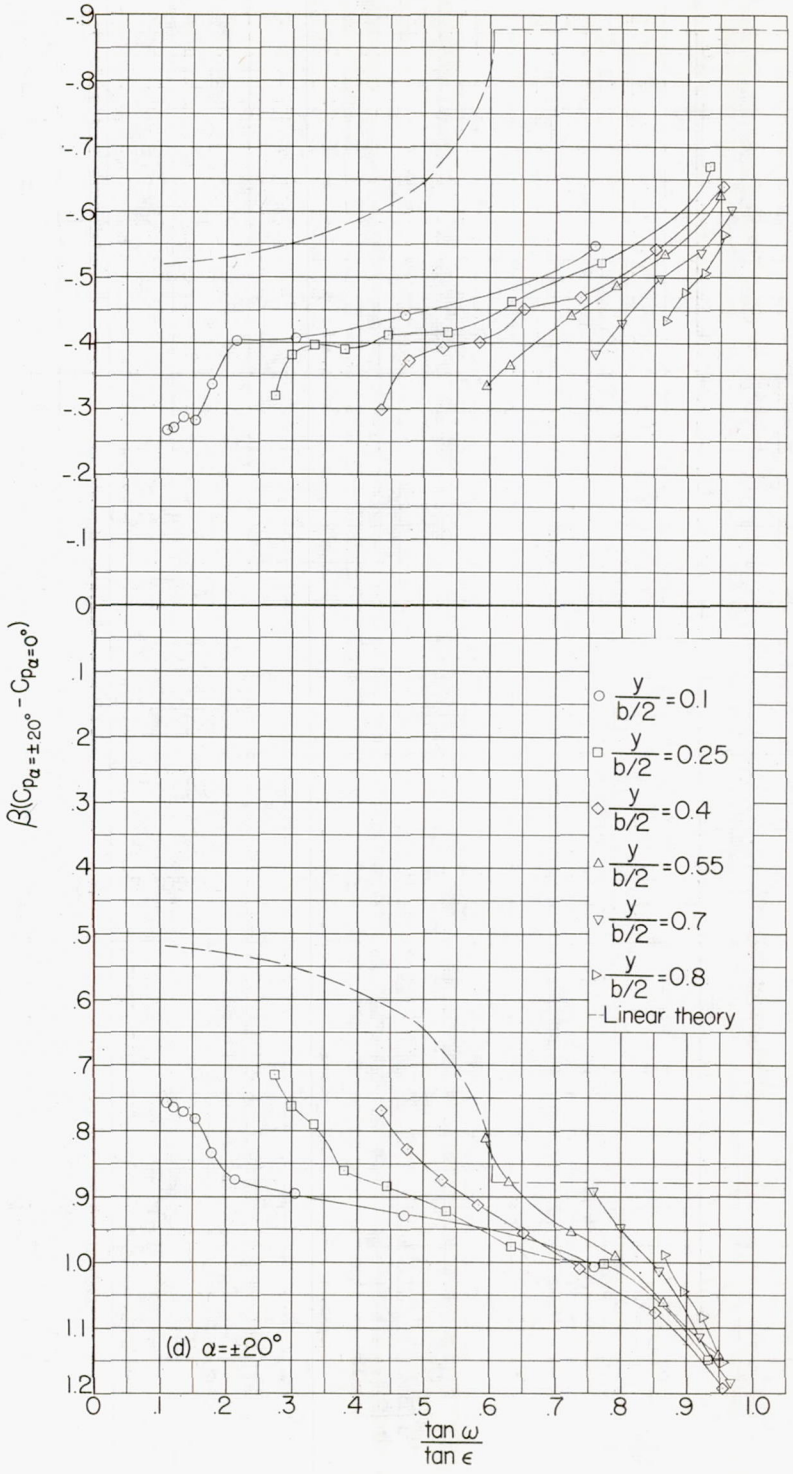


Figure 26.- Concluded.

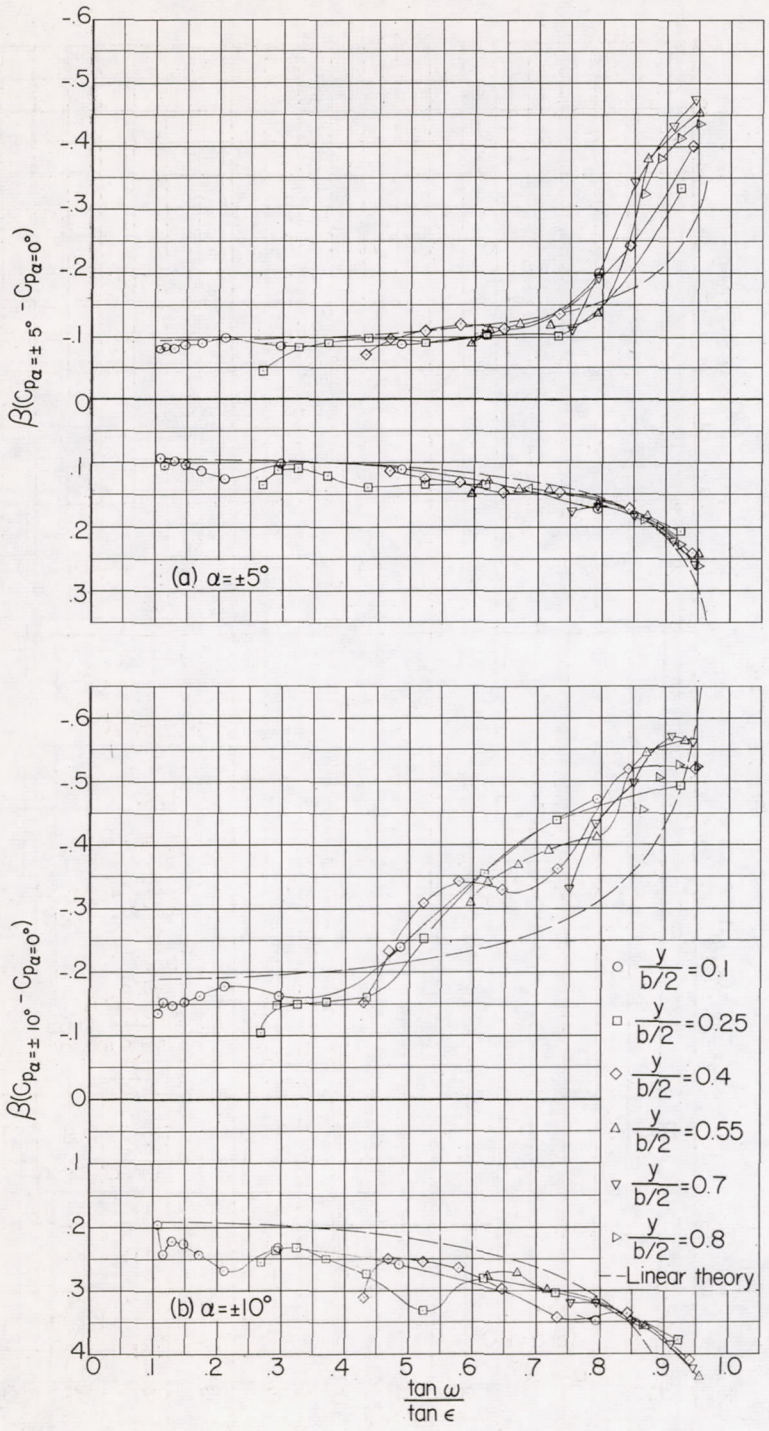


Figure 27.- Pressure distributions as a function of conical ray from wing apex. Wing 3 at M = 1.62.

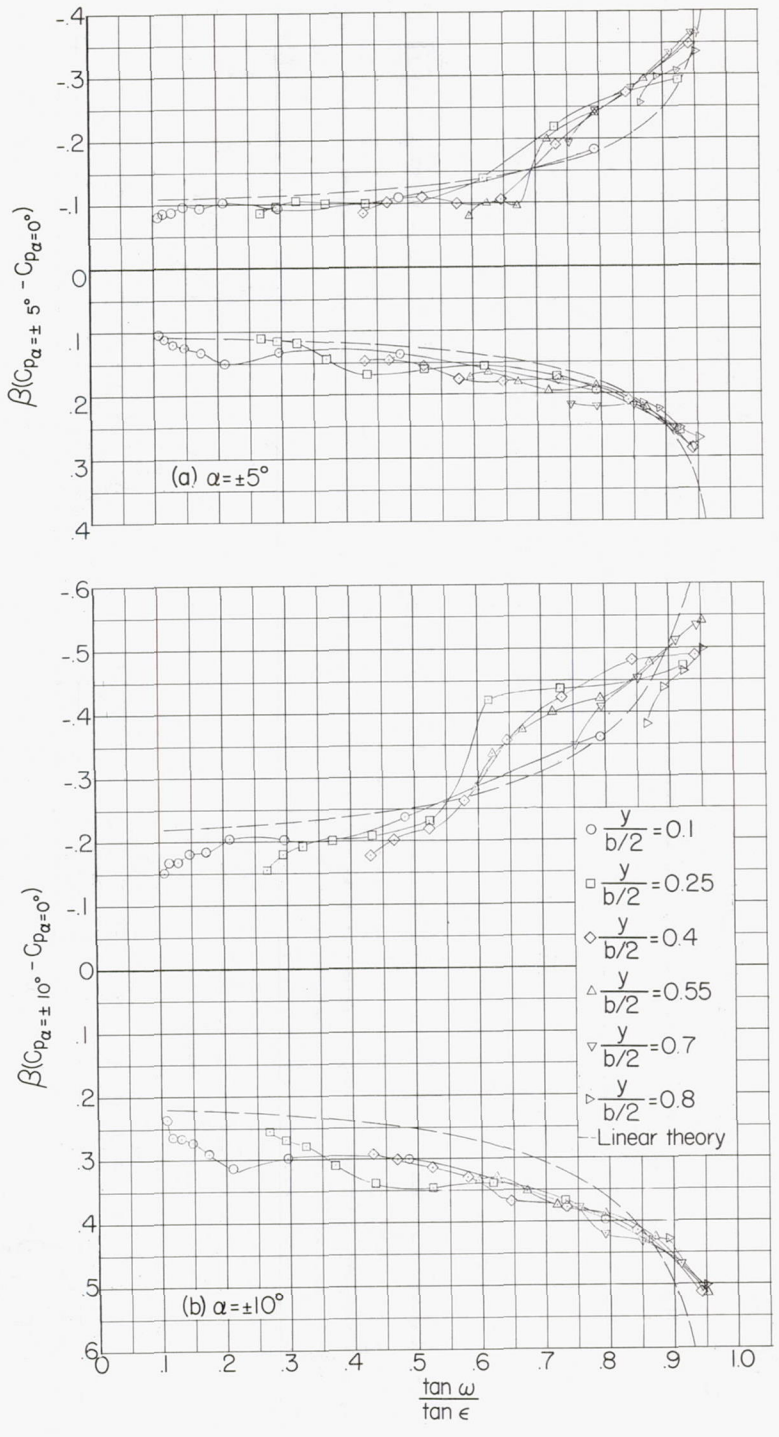


Figure 28.- Pressure distributions as a function of conical ray from wing apex. Wing 3 at M = 1.94.

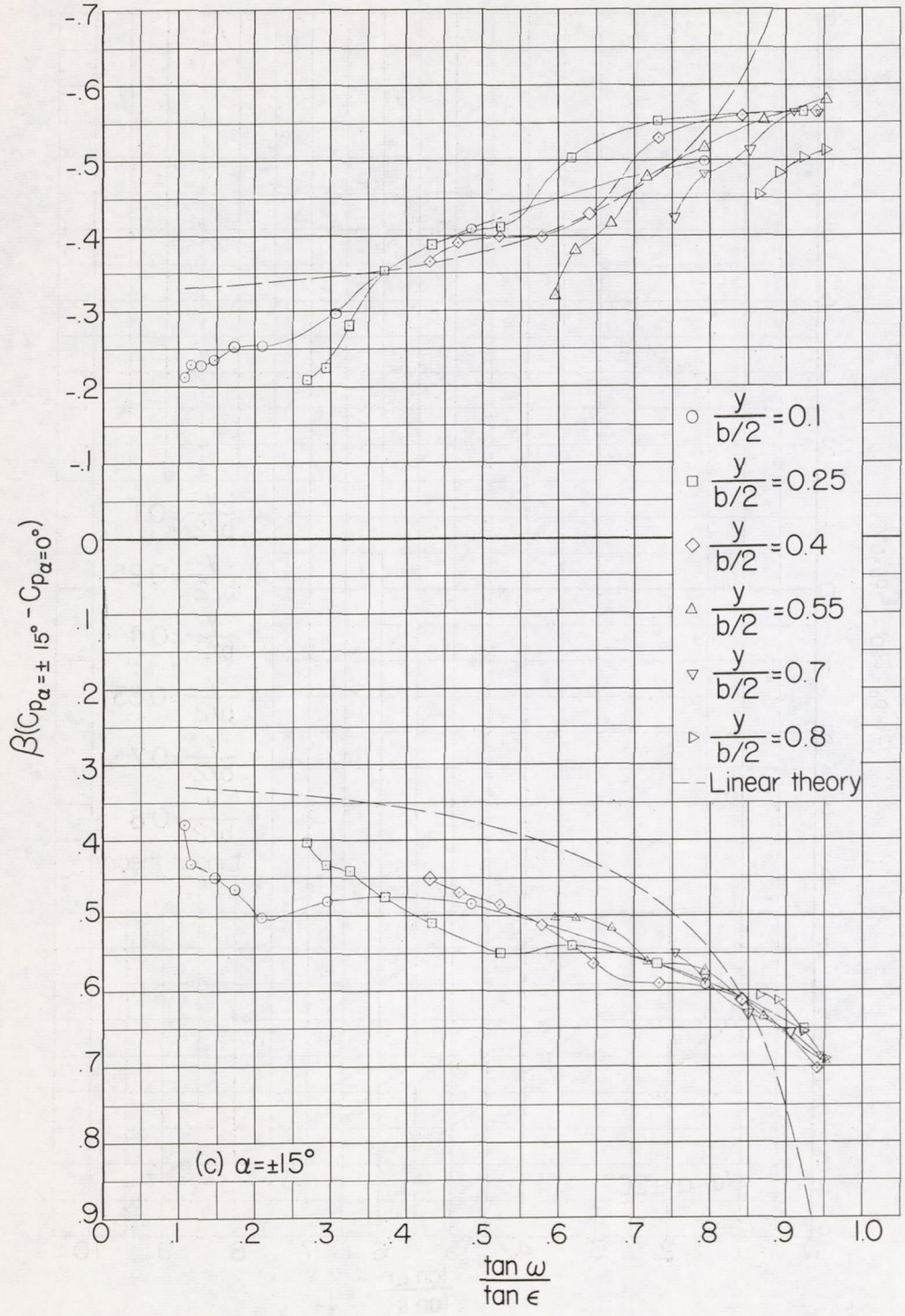


Figure 28.- Continued.

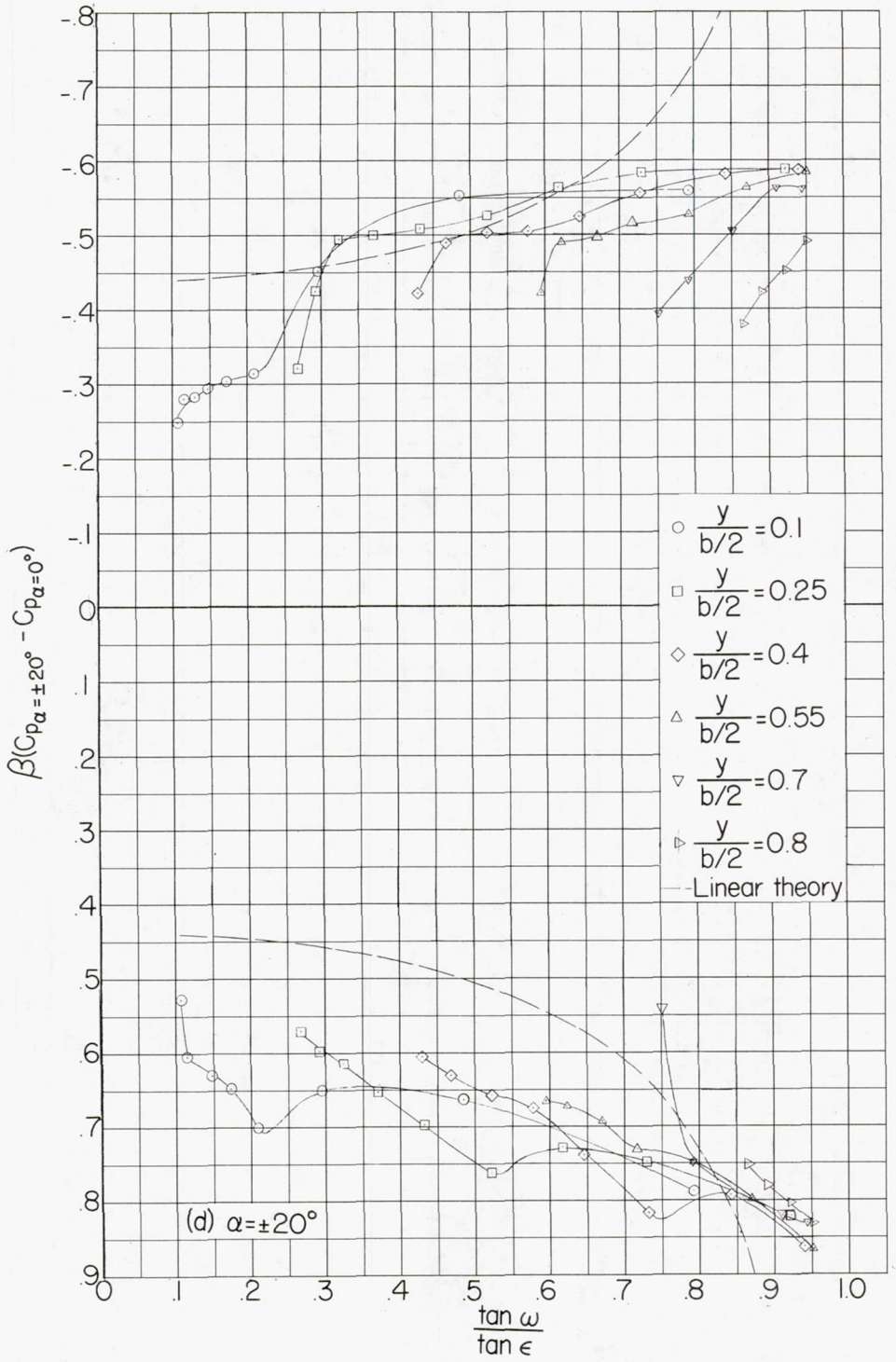


Figure 28.- Concluded.

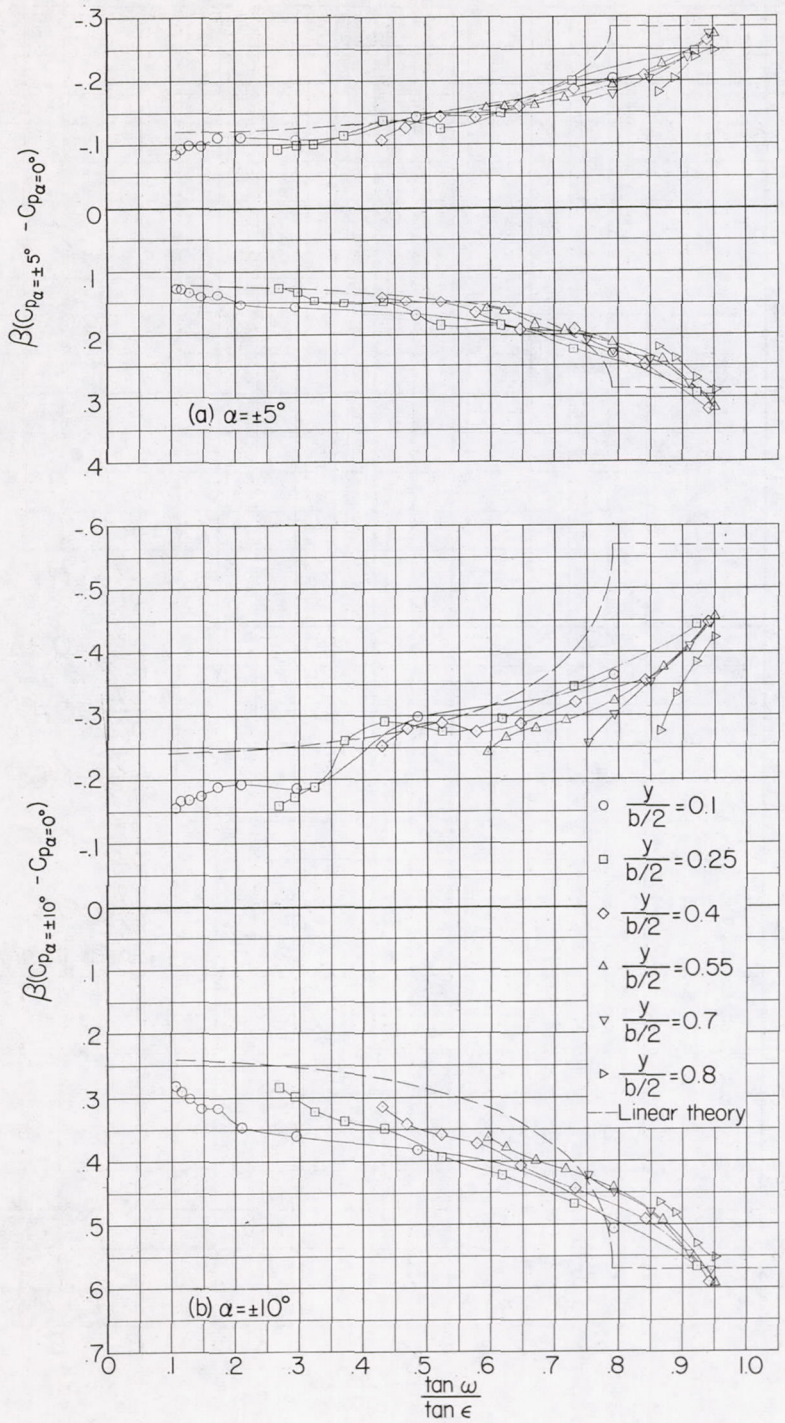


Figure 29.- Pressure distributions as a function of conical ray from wing apex. Wing 3 at M = 2.41.

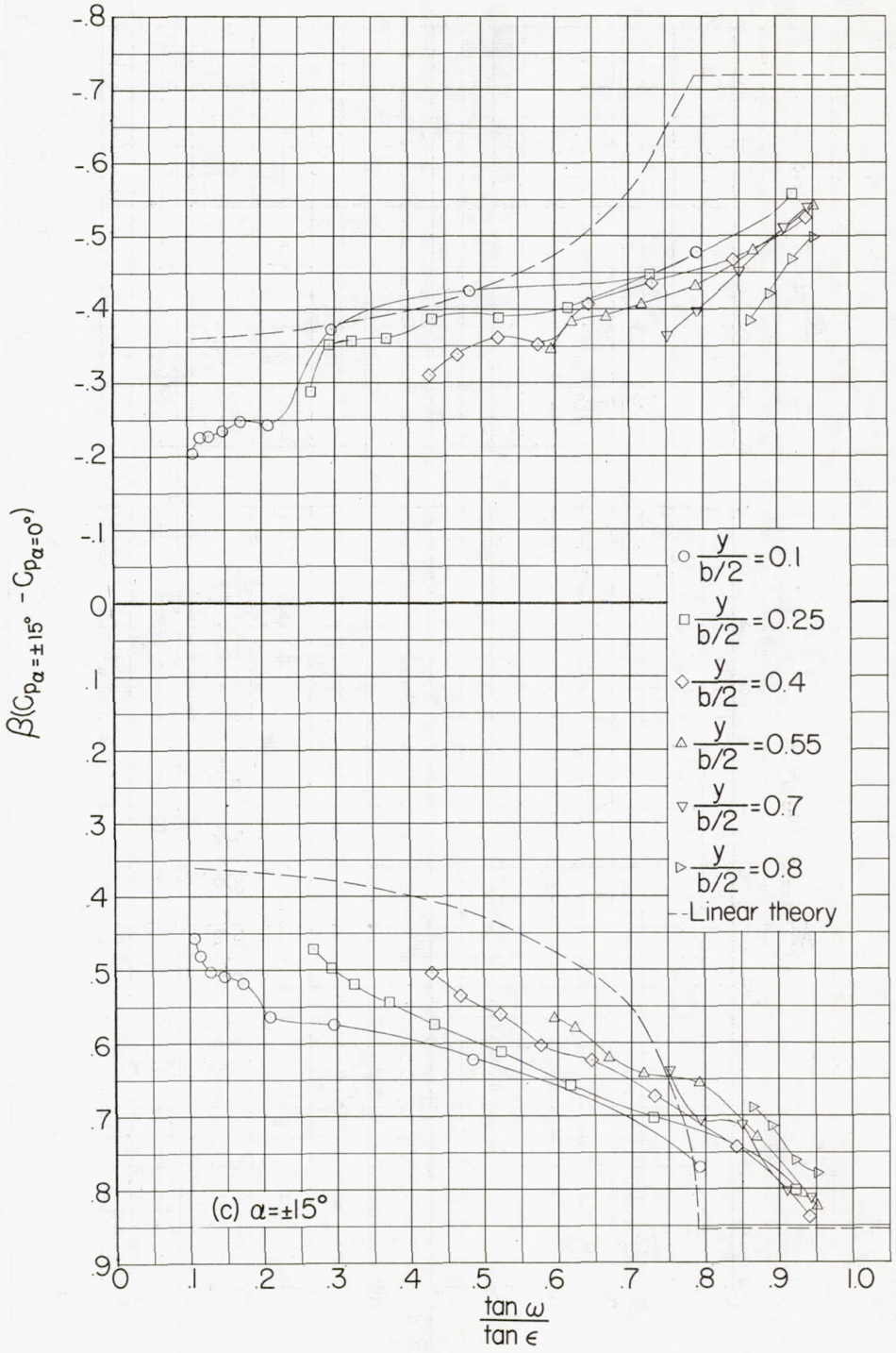


Figure 29.- Continued.

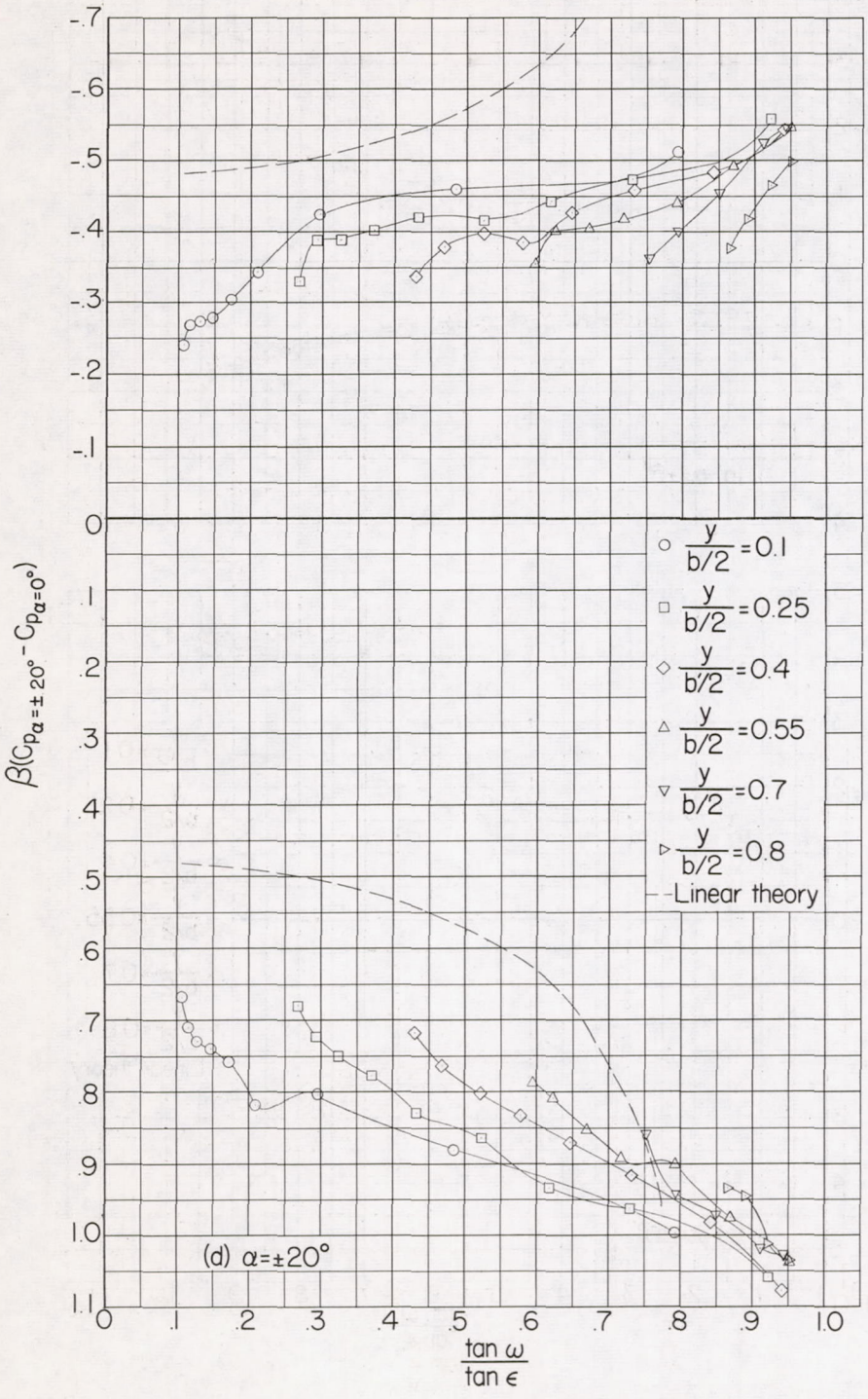


Figure 29.- Concluded.

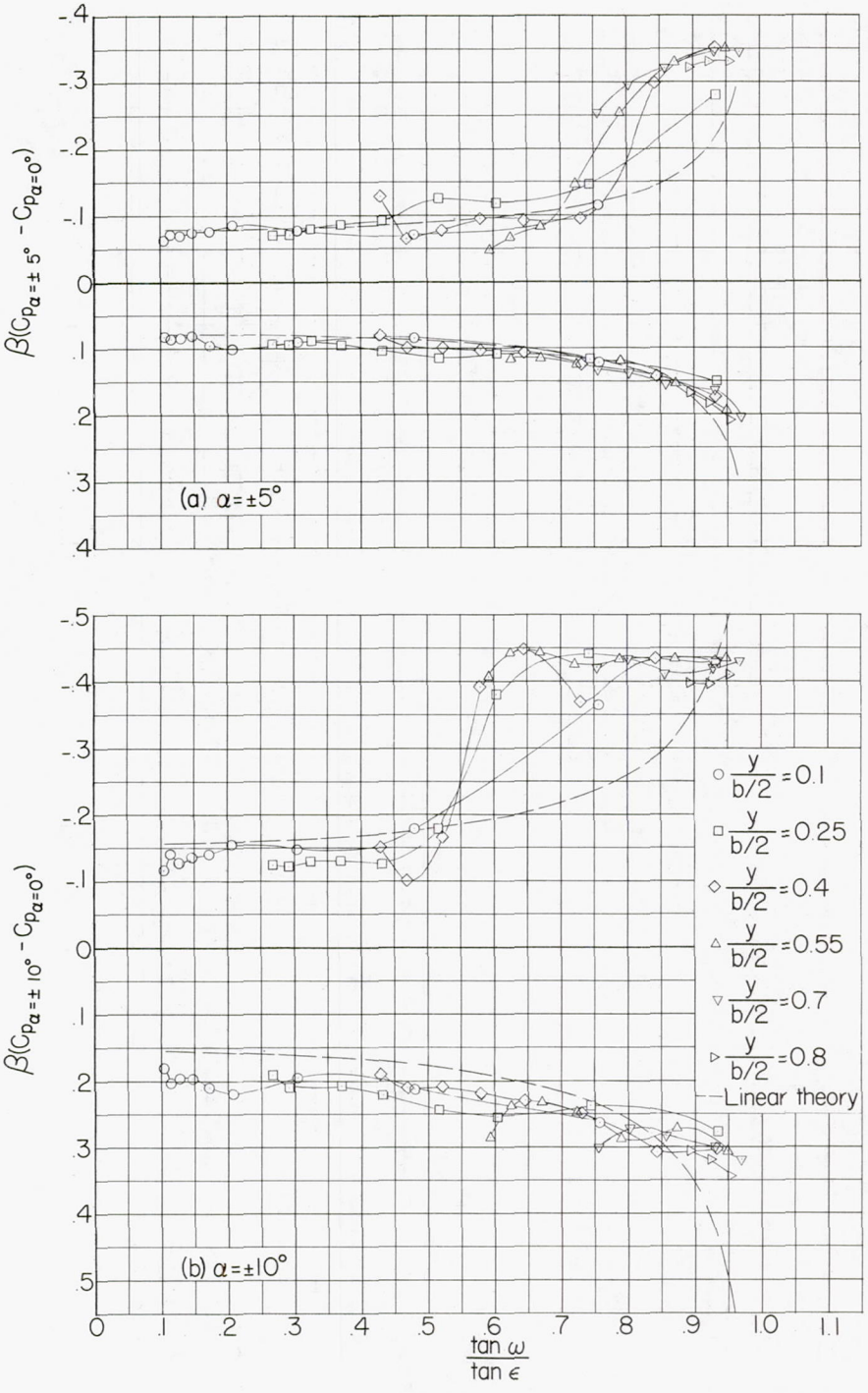


Figure 30.- Pressure distributions as a function of conical ray from wing apex. Wing 4 at M = 1.62.

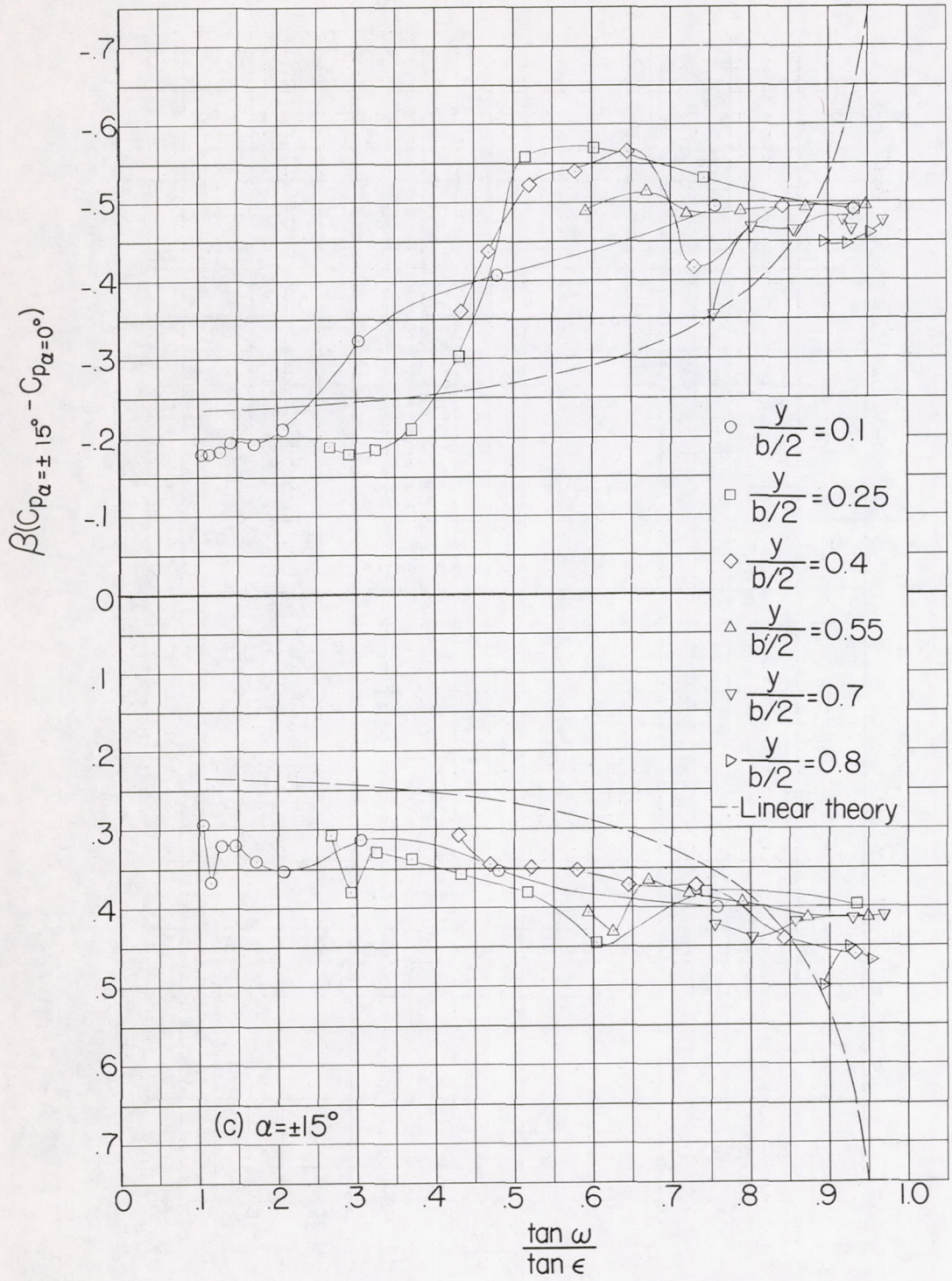


Figure 30.- Continued.

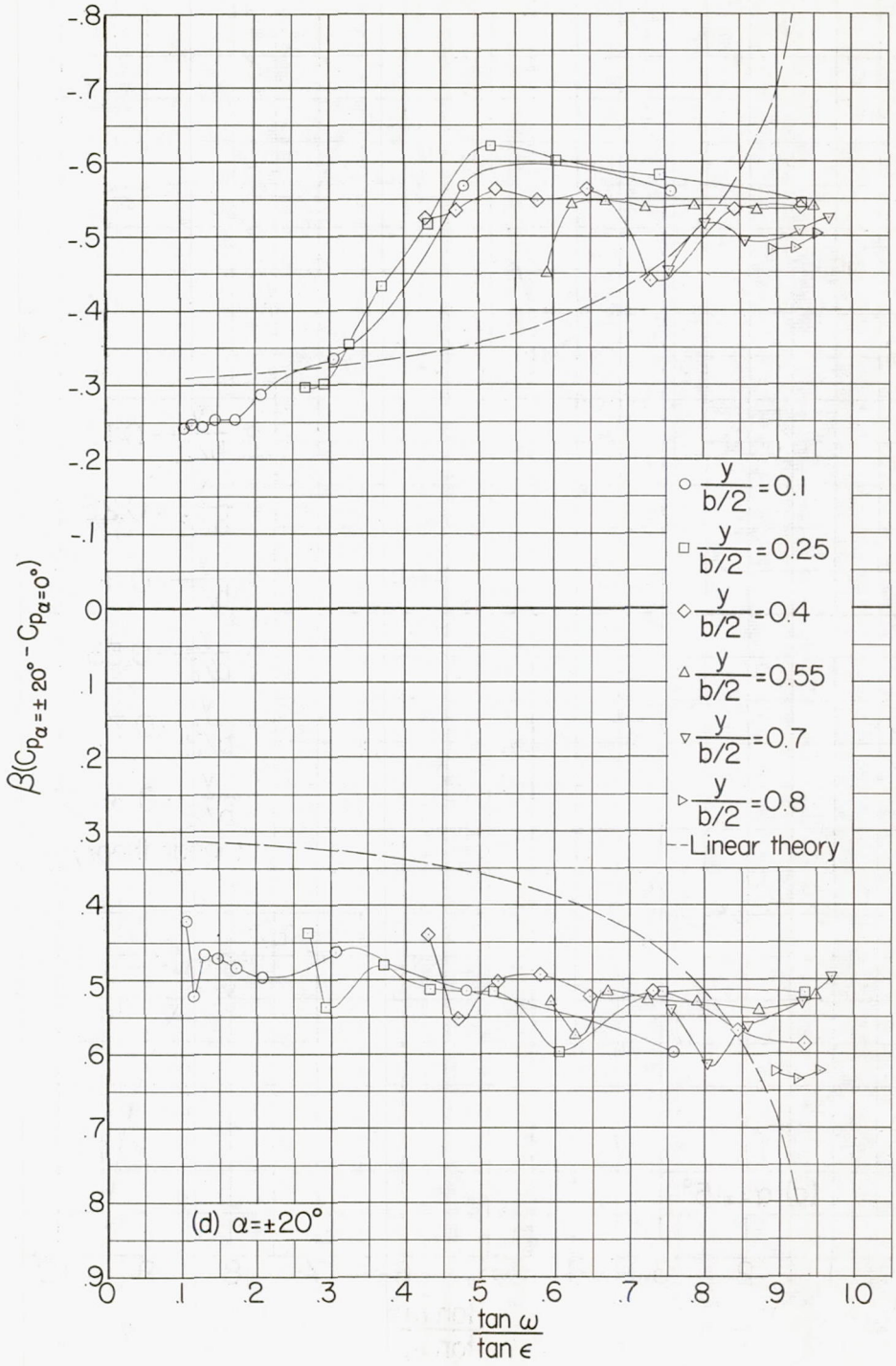


Figure 30.- Concluded.

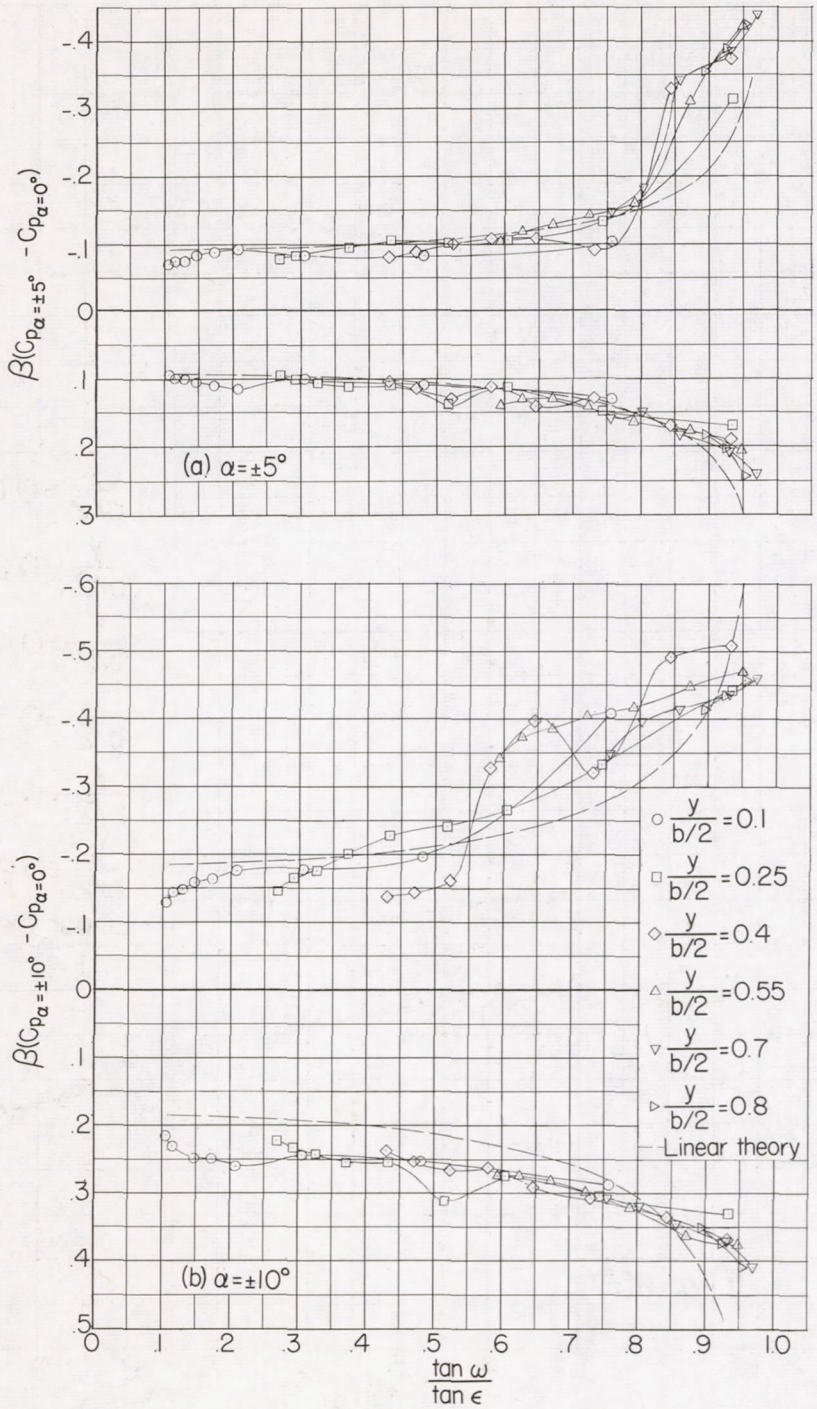


Figure 31.- Pressure distributions as a function of conical ray from wing apex. Wing 4 at M = 1.94.

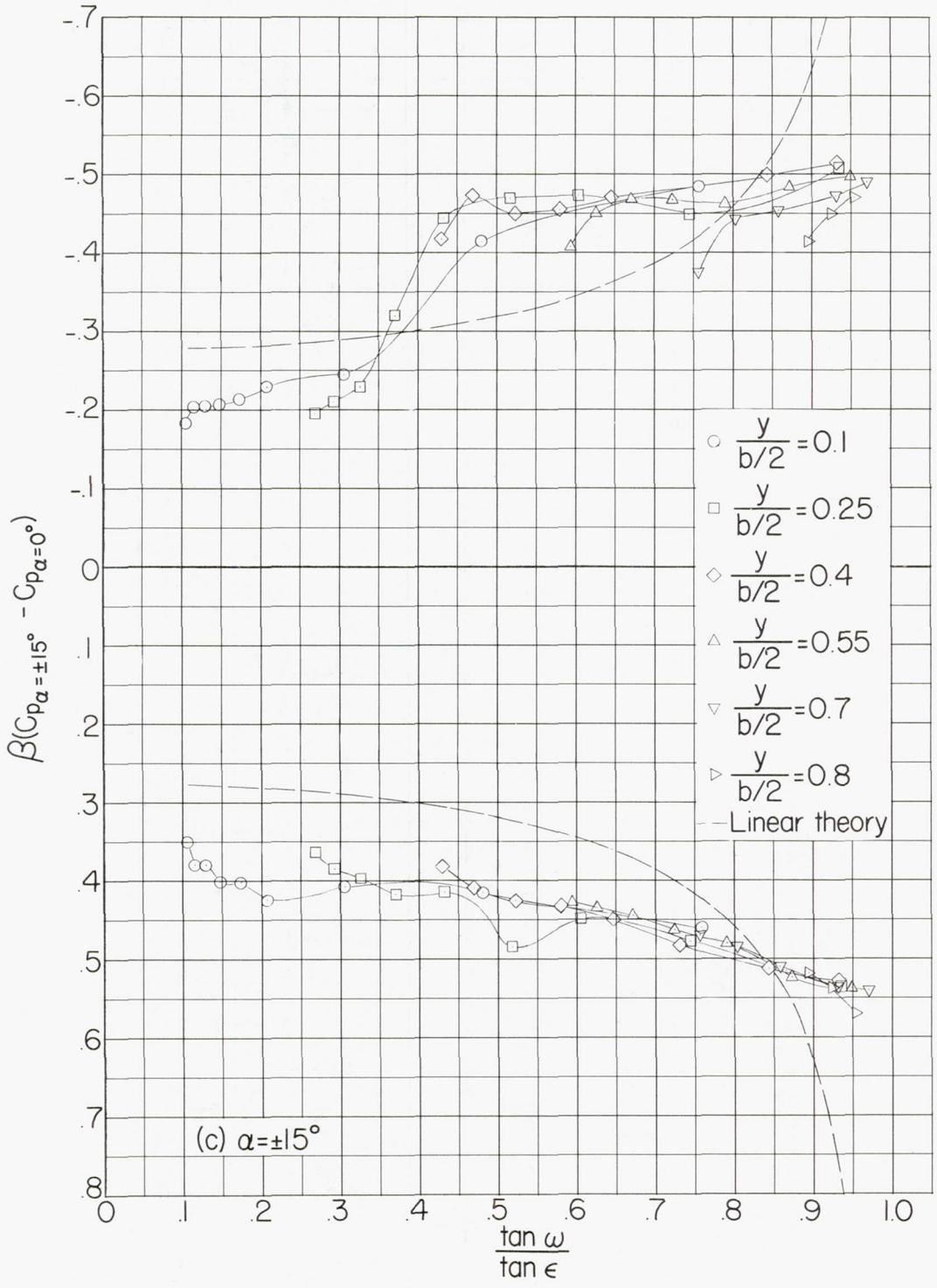


Figure 31.- Continued.

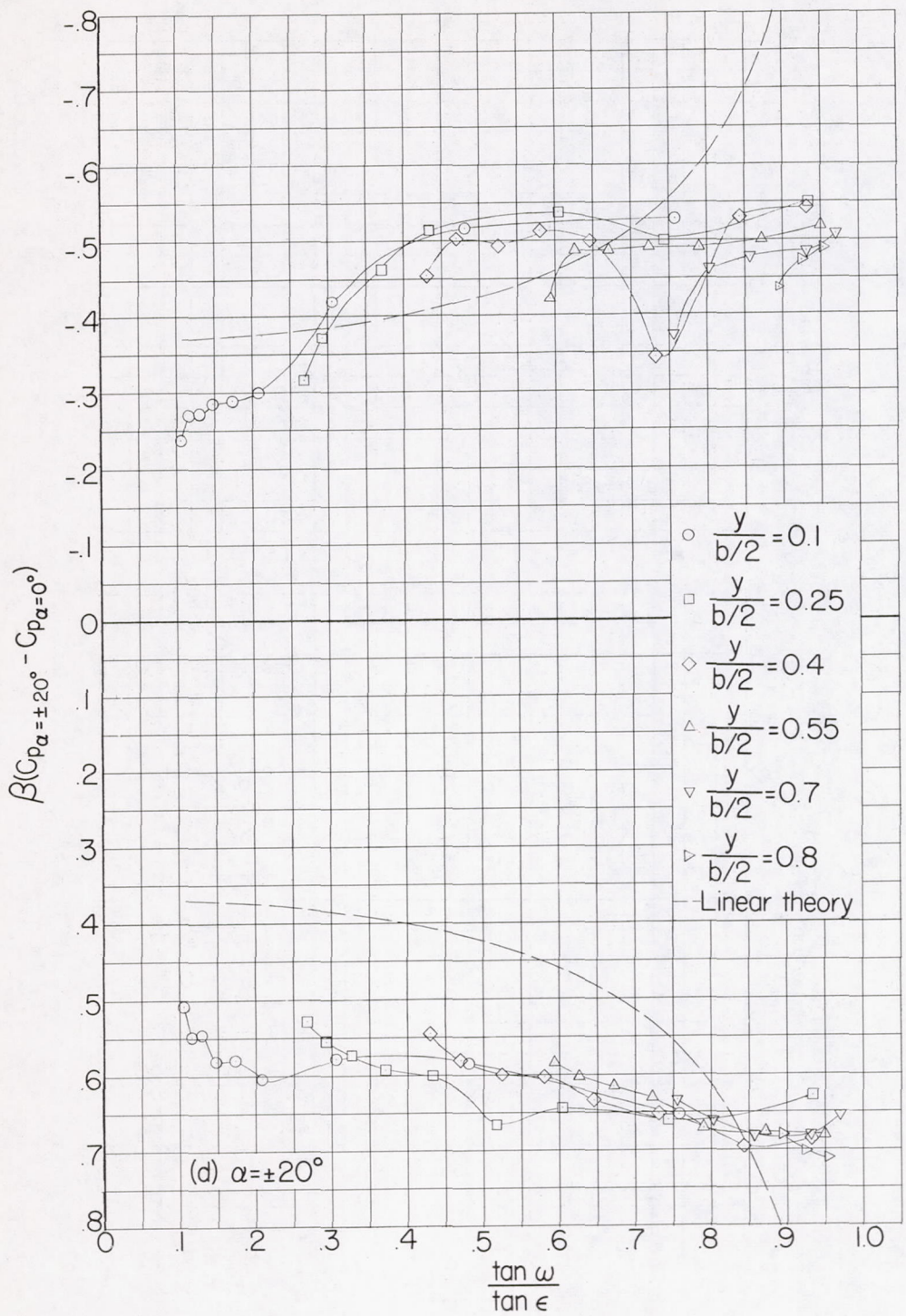


Figure 31.- Concluded.

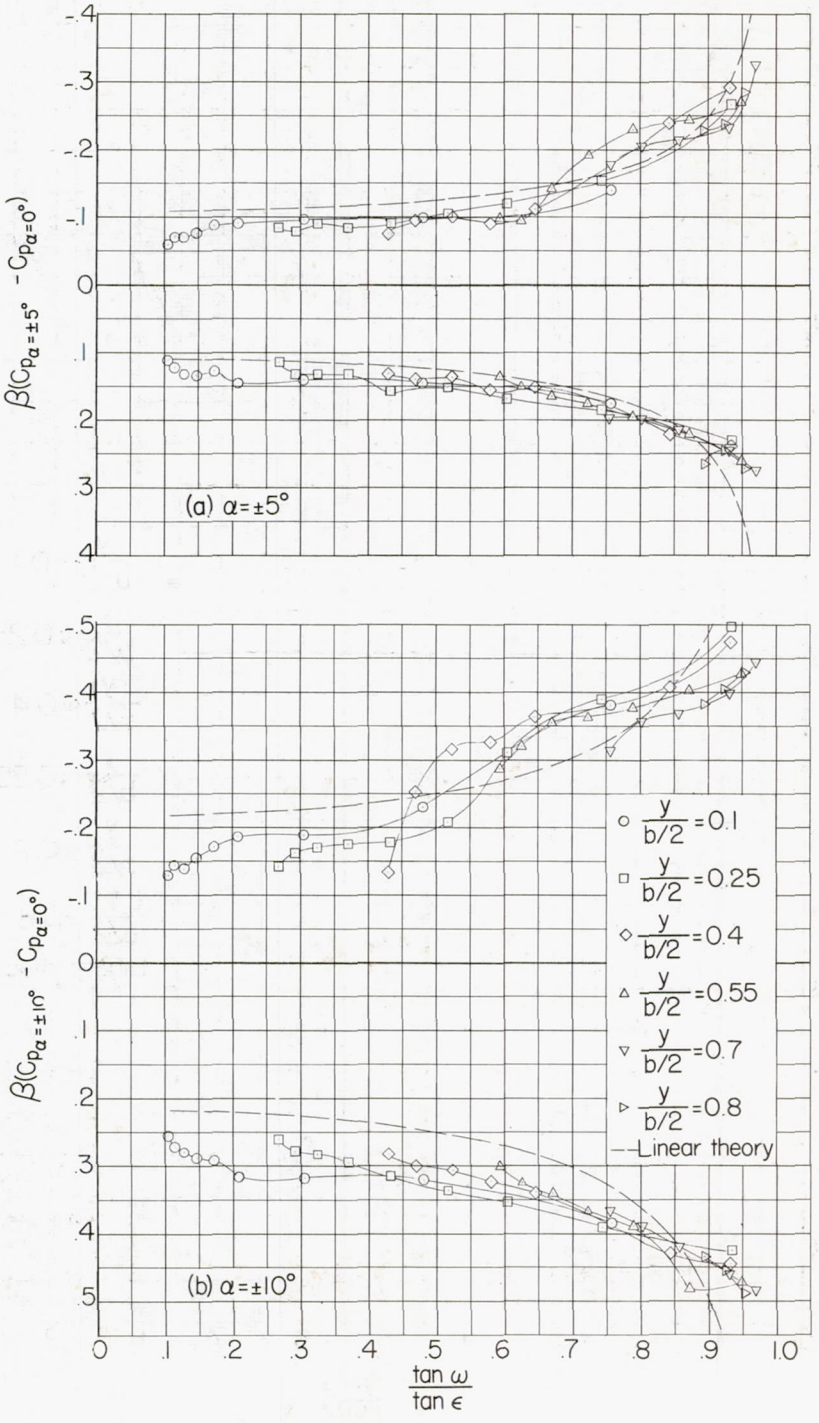


Figure 32.- Pressure distributions as a function of conical ray from wing apex. Wing 4 at M = 2.41.

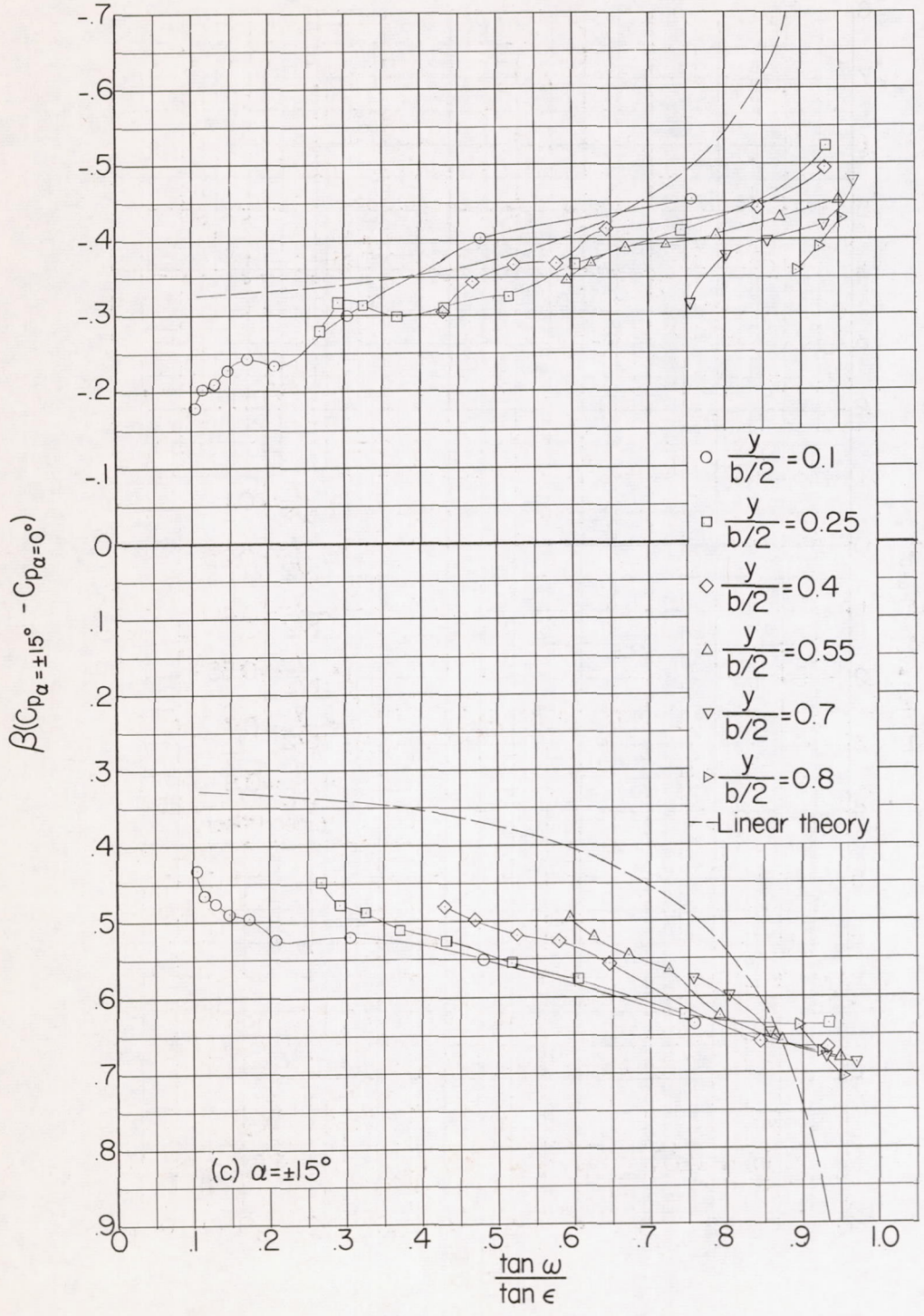


Figure 32.- Continued.

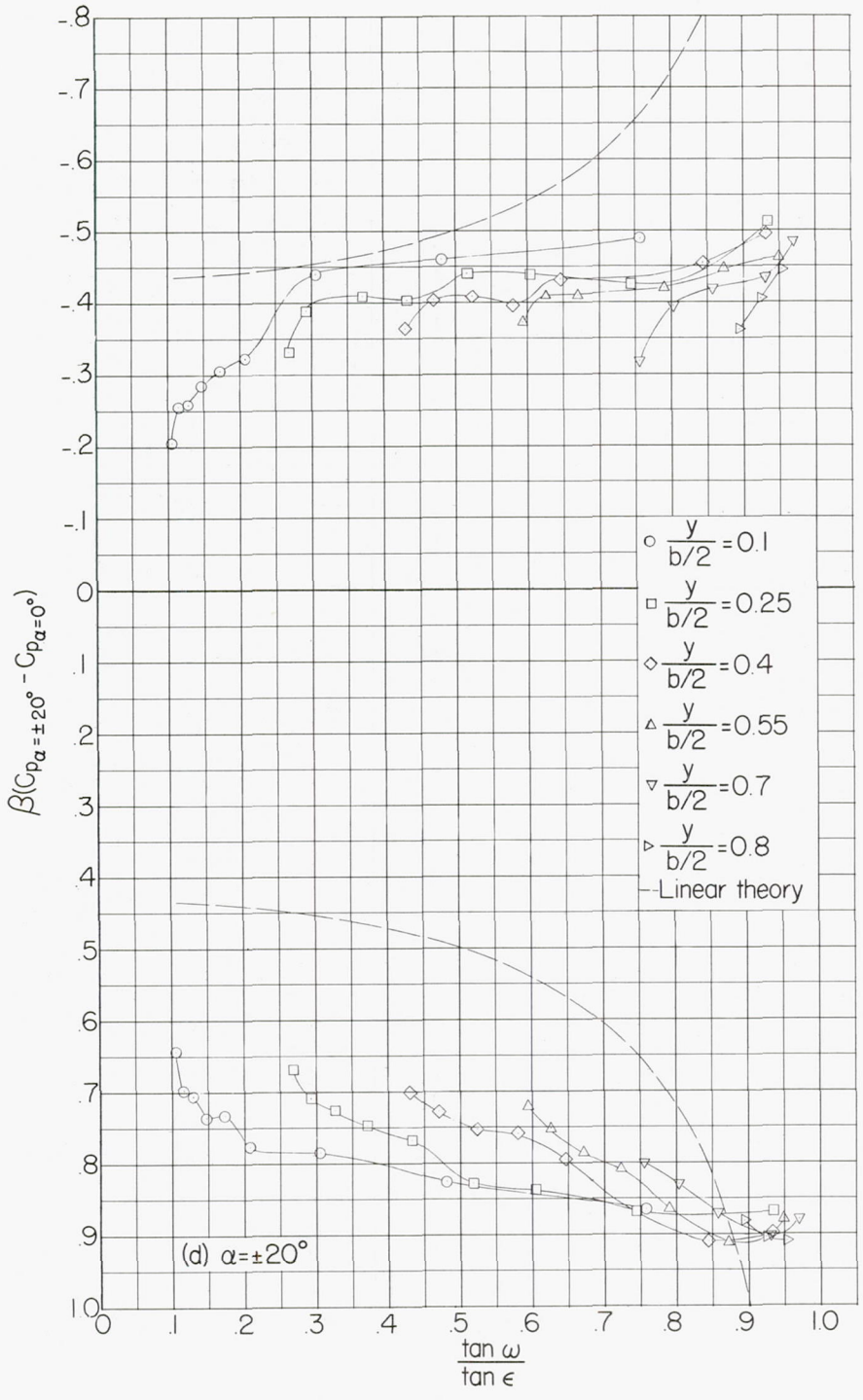
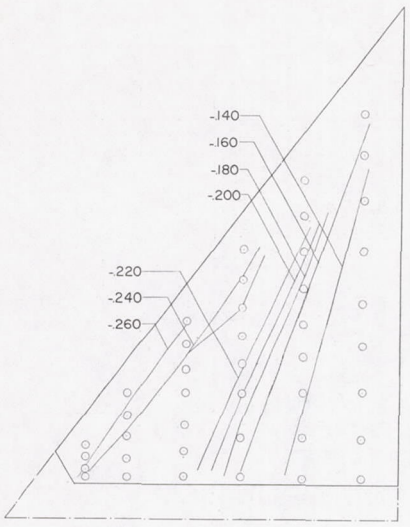
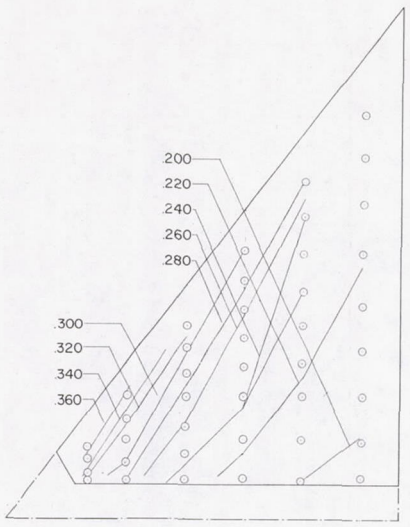


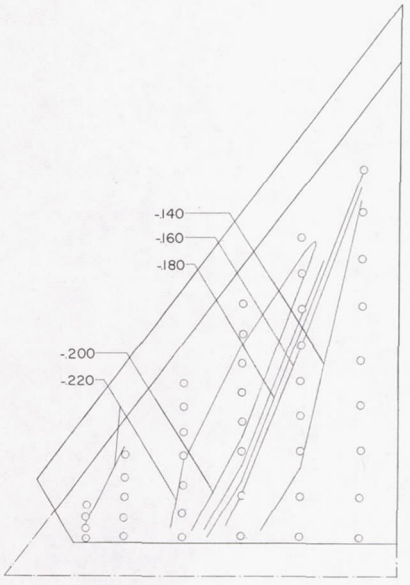
Figure 32.- Concluded.



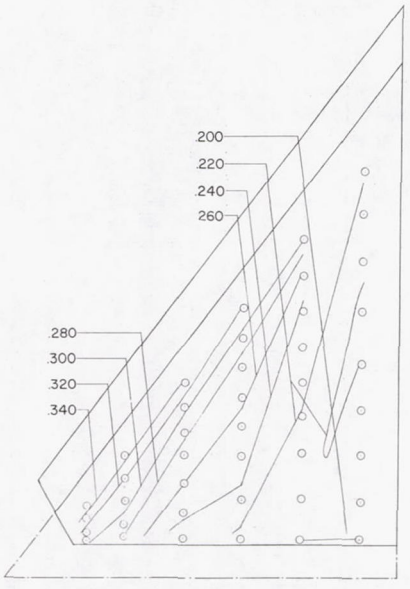
(a) Low-pressure side; no leading-edge extension; values of $C_{p_{\alpha=11.3^o}} - C_{p_{\alpha=0^o}}$.



(b) High-pressure side; no leading-edge extension; values of $C_{p_{\alpha=-11.3^o}} - C_{p_{\alpha=0^o}}$.

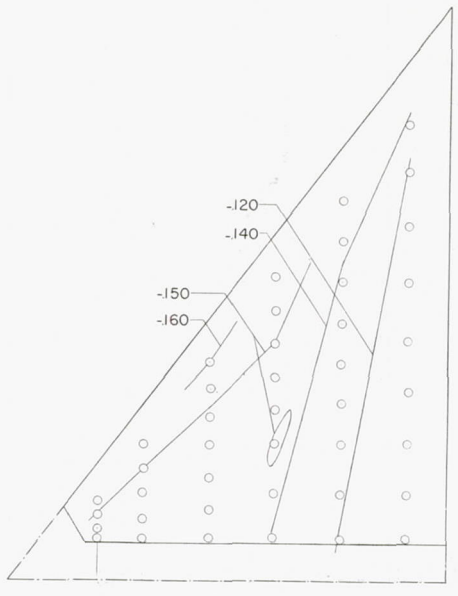


(c) Low-pressure side; with leading-edge extension; values of $C_{p_{\alpha=11.3^o}} - C_{p_{\alpha=0^o}}$.

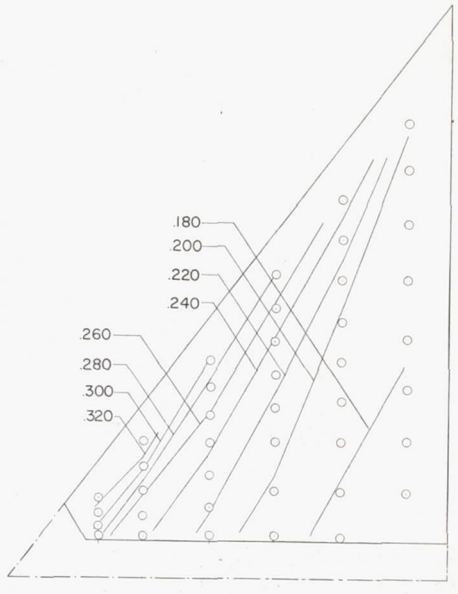


(d) High-pressure side; with leading-edge extension; values of $C_{p_{\alpha=-11.3^o}} - C_{p_{\alpha=0^o}}$.

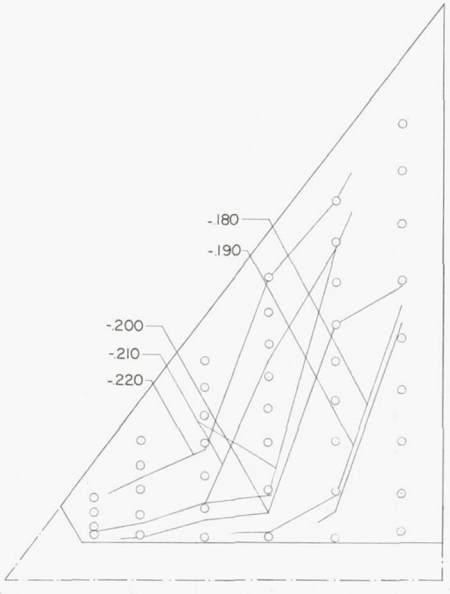
Figure 33.- Pressure contours for wing 1 at M = 1.94.



(a) Low-pressure side; $C_{p_{\alpha=11.3^\circ}} - C_{p_{\alpha=0^\circ}}$.



(b) High-pressure side; $C_{p_{\alpha=-11.3^\circ}} - C_{p_{\alpha=0^\circ}}$.

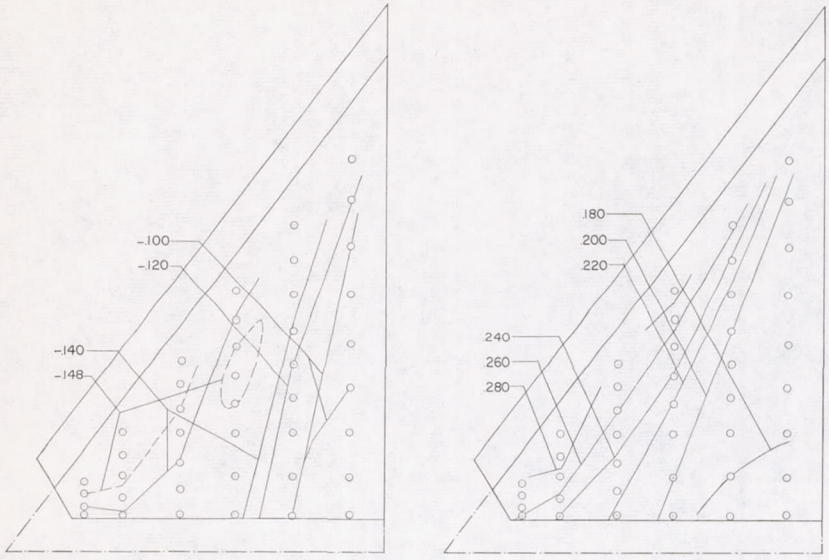


(c) Low-pressure side; $C_{p_{\alpha=21.2^\circ}} - C_{p_{\alpha=0^\circ}}$.



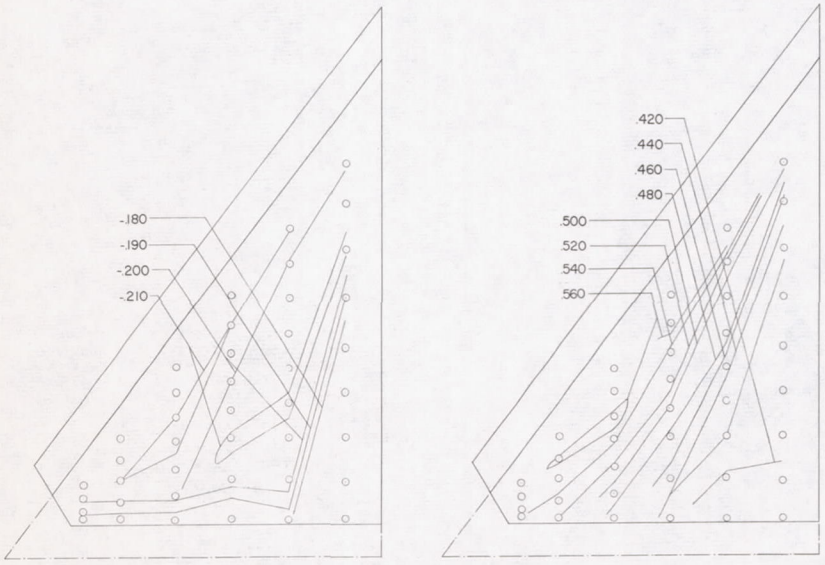
(d) High-pressure side; $C_{p_{\alpha=-21.2^\circ}} - C_{p_{\alpha=0^\circ}}$.

Figure 34.- Pressure contours for wing 1 at M = 2.41.



(a) Low-pressure side; $C_{p_{\alpha=11.3^\circ}} - C_{p_{\alpha=0^\circ}}$.

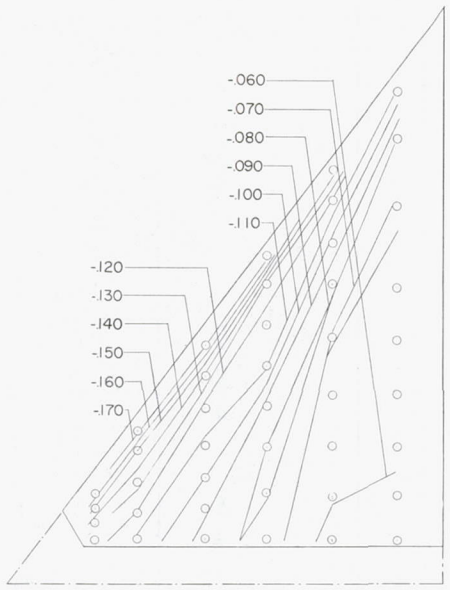
(b) High-pressure side; $C_{p_{\alpha=-11.3^\circ}} - C_{p_{\alpha=0^\circ}}$.



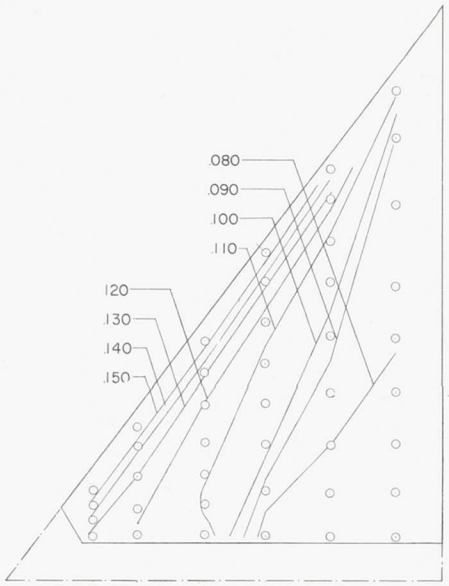
(c) Low-pressure side; $C_{p_{\alpha=21.2^\circ}} - C_{p_{\alpha=0^\circ}}$.

(d) High-pressure side; $C_{p_{\alpha=-21.2^\circ}} - C_{p_{\alpha=0^\circ}}$.

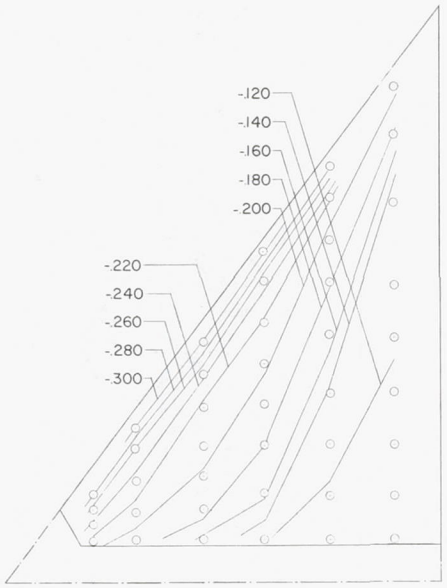
Figure 35.- Pressure contours for wing 1 at M = 2.41 with leading-edge extension.



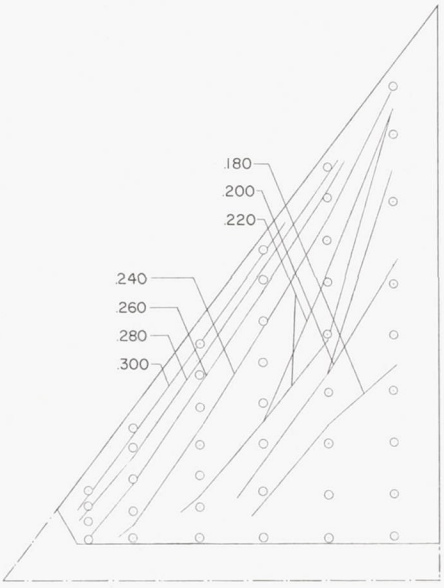
(a) Low-pressure side;
$C_{p_{\alpha=5^\circ}} - C_{p_{\alpha=0^\circ}}$.



(b) High-pressure side;
$C_{p_{\alpha=-5^\circ}} - C_{p_{\alpha=5^\circ}}$.

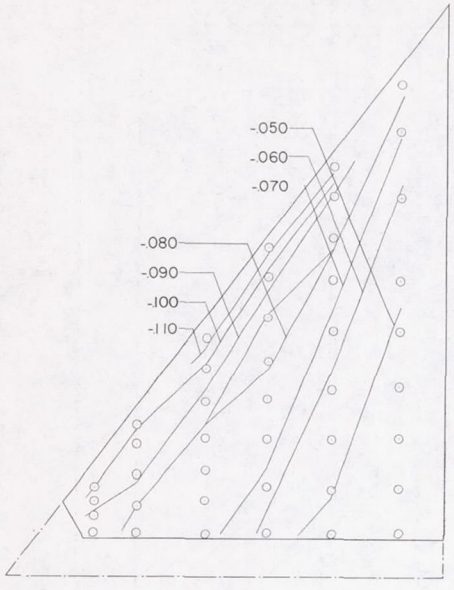


(c) Low-pressure side;
$C_{p_{\alpha=10^\circ}} - C_{p_{\alpha=0^\circ}}$.

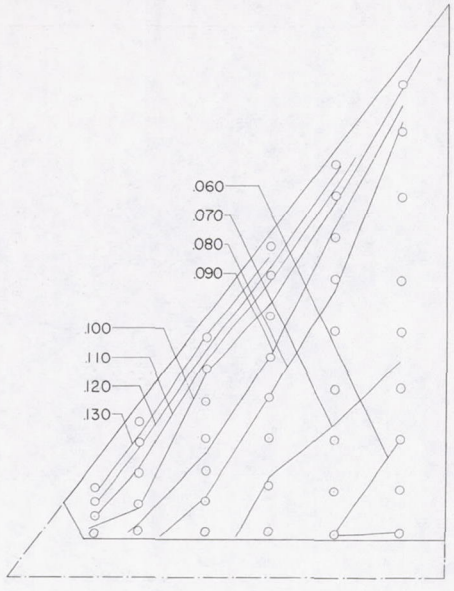


(d) High-pressure side;
$C_{p_{\alpha=-10^\circ}} - C_{p_{\alpha=0^\circ}}$.

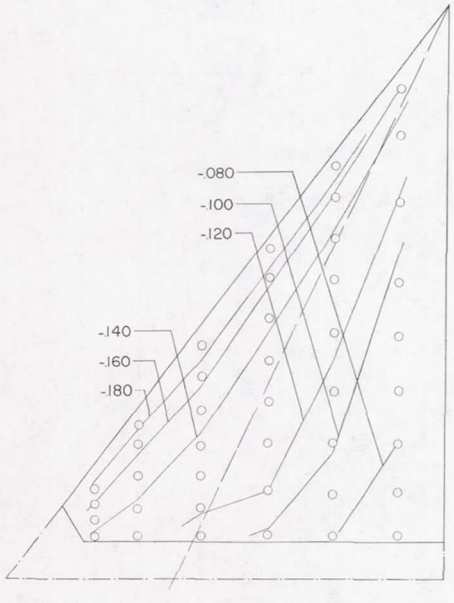
Figure 36.- Pressure contours for wing 2 at M = 1.94.



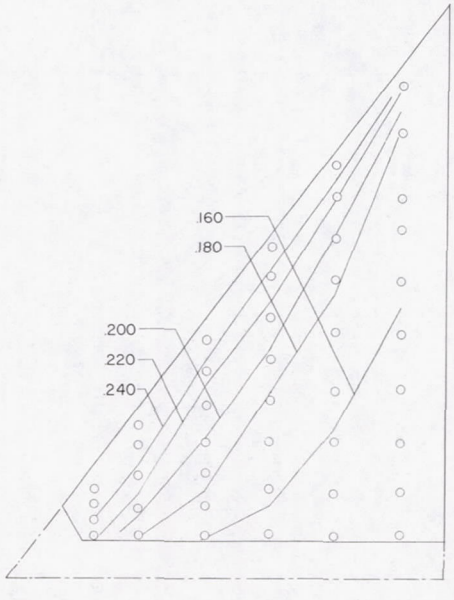
(a) Low-pressure side;
$C_{p_{\alpha=5^\circ}} - C_{p_{\alpha=0^\circ}}$.



(b) High-pressure side;
$C_{p_{\alpha=-5^\circ}} - C_{p_{\alpha=0^\circ}}$.

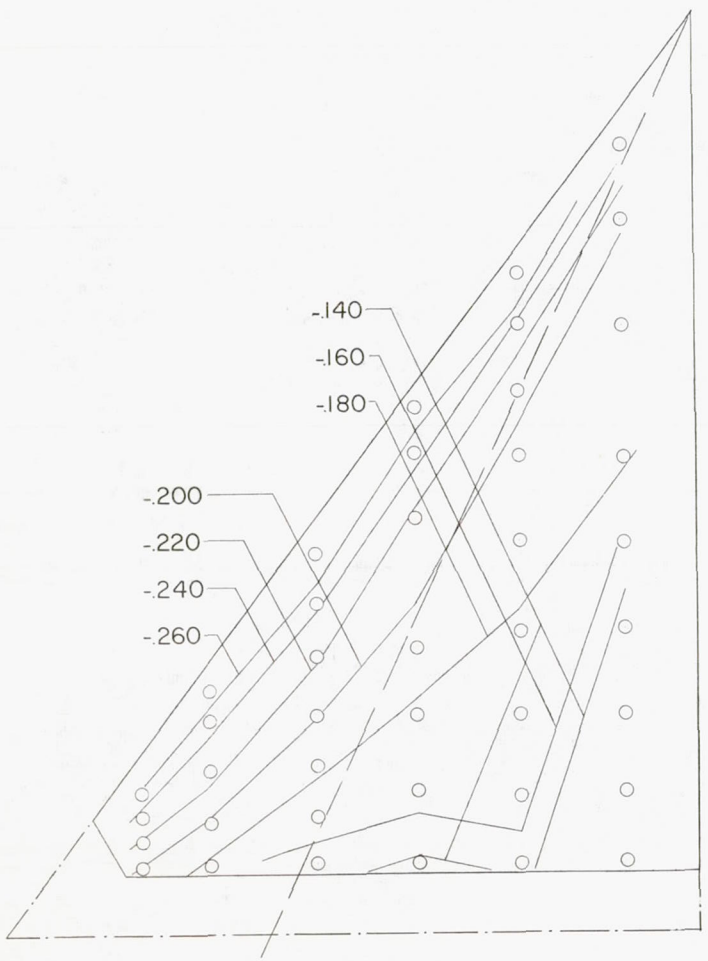


(c) Low-pressure side;
$C_{p_{\alpha=10^\circ}} - C_{p_{\alpha=0^\circ}}$.

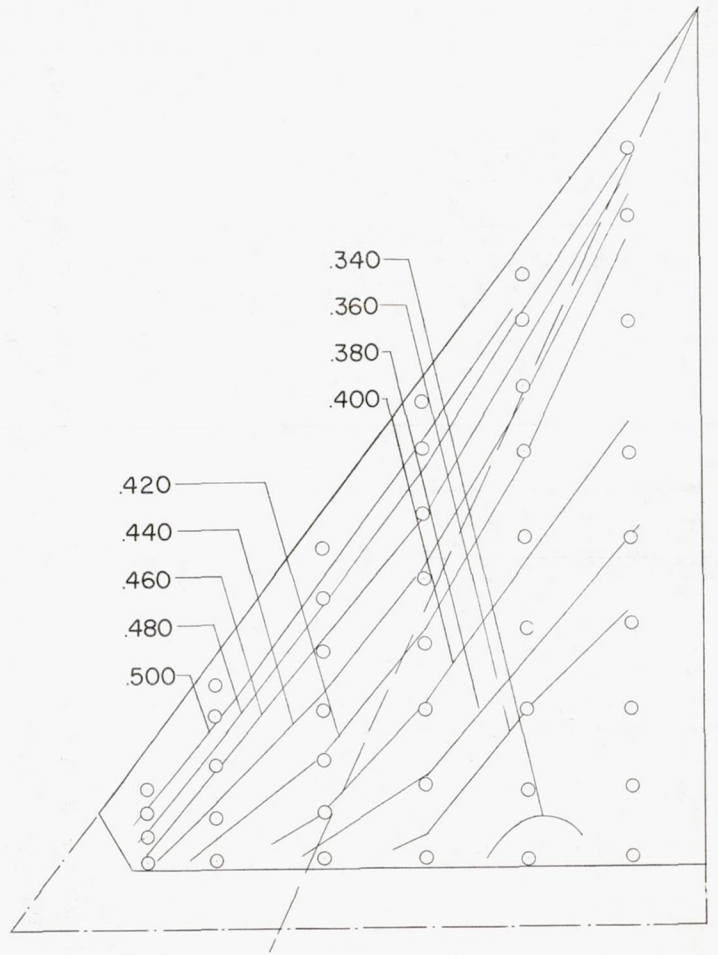


(d) High-pressure side;
$C_{p_{\alpha=-10^\circ}} - C_{p_{\alpha=0^\circ}}$.

Figure 37.- Pressure contours for wing 2 at M = 2.41.

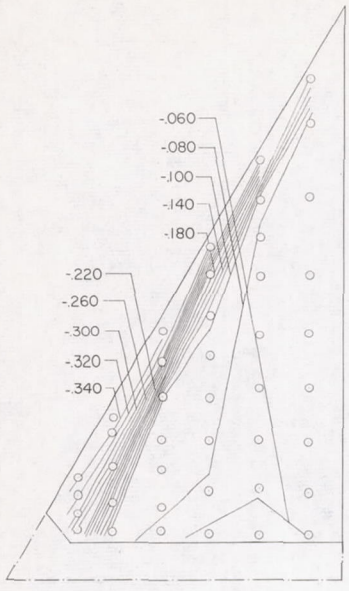


(e) Low-pressure side;
$C_{p_{\alpha=20^\circ}} - C_{p_{\alpha=0^\circ}}$.

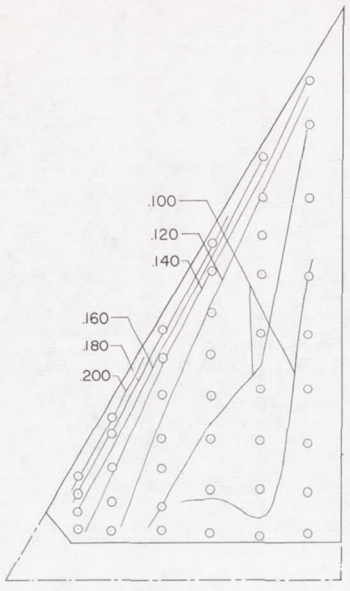


(f) High-pressure side;
$C_{p_{\alpha=-20^\circ}} - C_{p_{\alpha=0^\circ}}$.

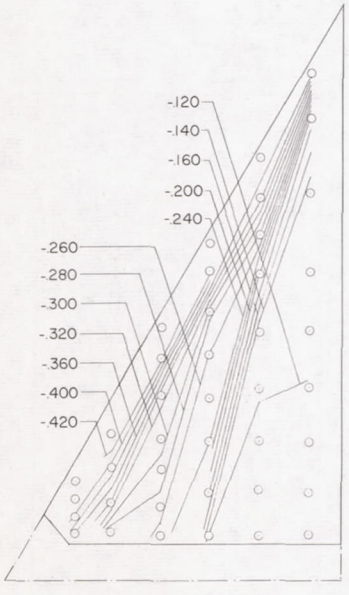
Figure 37.- Concluded.



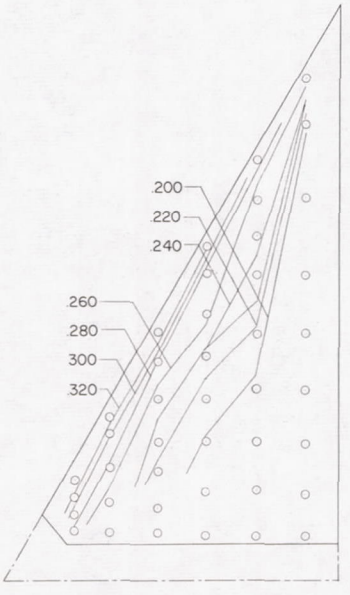
(a) Low-pressure side; $C_{p_{\alpha=5^\circ}} - C_{p_{\alpha=0^\circ}}$.



(b) High-pressure side; $C_{p_{\alpha=-5^\circ}} - C_{p_{\alpha=0^\circ}}$.

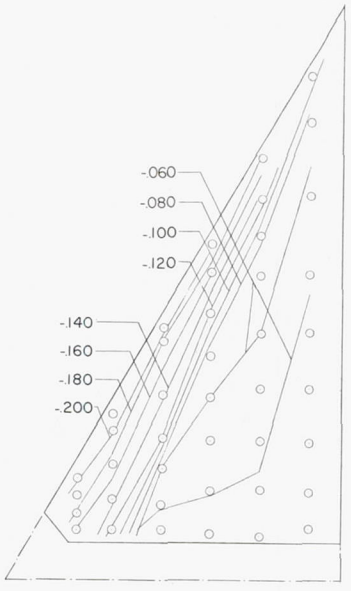


(c) Low-pressure side; $C_{p_{\alpha=10^\circ}} - C_{p_{\alpha=0^\circ}}$.

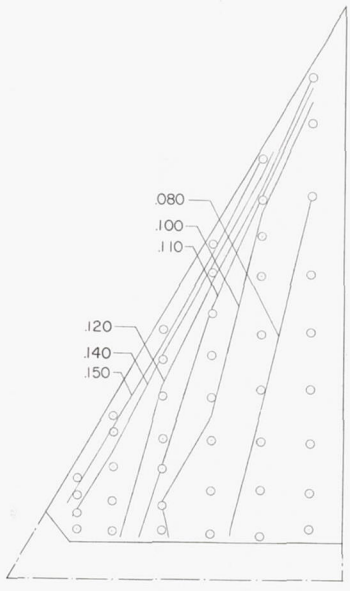


(d) High-pressure side; $C_{p_{\alpha=-10^\circ}} - C_{p_{\alpha=0^\circ}}$.

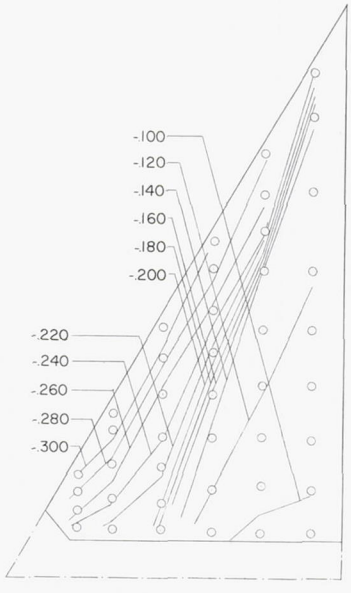
Figure 38.- Pressure contours for wing 3 at M = 1.62.



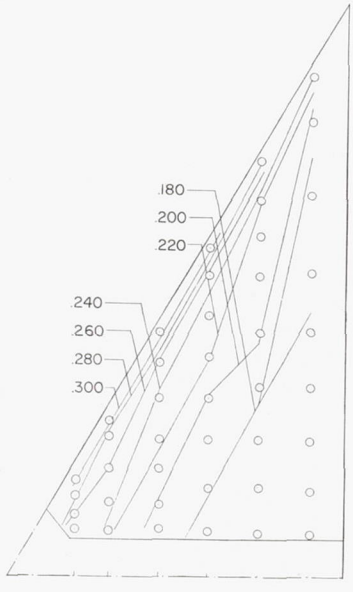
(a) Low-pressure side; $C_{p_{\alpha=5^\circ}} - C_{p_{\alpha=0^\circ}}$.



(b) High-pressure side; $C_{p_{\alpha=-5^\circ}} - C_{p_{\alpha=0^\circ}}$.

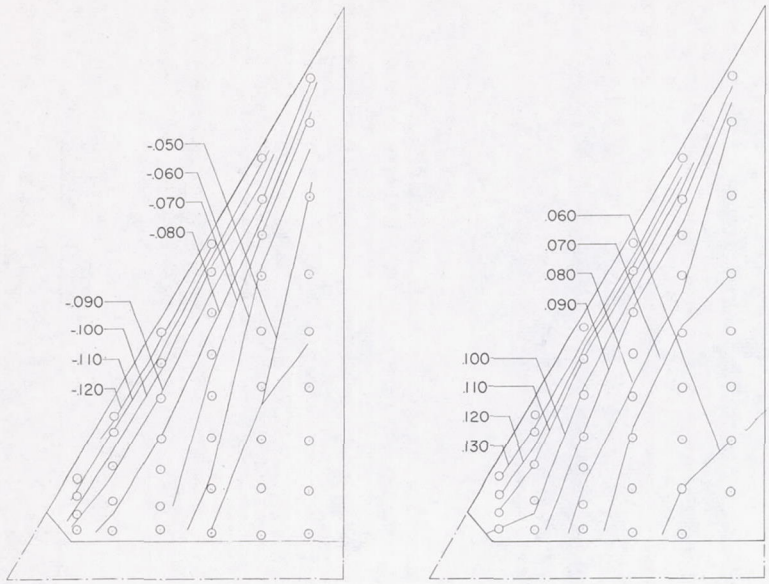


(c) Low-pressure side; $C_{p_{\alpha=10^\circ}} - C_{p_{\alpha=0^\circ}}$.



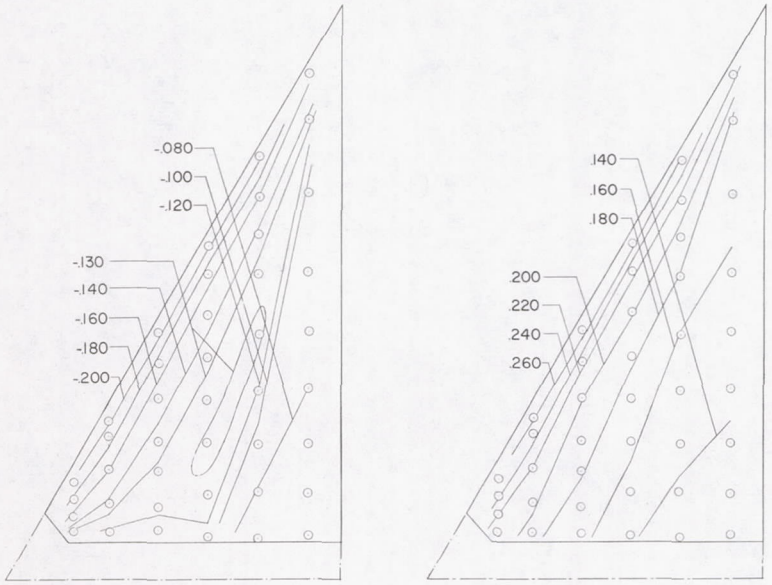
(d) High-pressure side; $C_{p_{\alpha=-10^\circ}} - C_{p_{\alpha=0^\circ}}$.

Figure 39.- Pressure contours for wing 3 at M = 1.94.



(a) Low-pressure side; $C_{p_{\alpha=5^\circ}} - C_{p_{\alpha=0^\circ}}$.

(b) High-pressure side; $C_{p_{\alpha=-5^\circ}} - C_{p_{\alpha=0^\circ}}$.



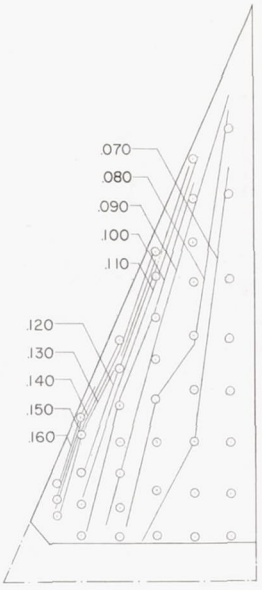
(c) Low-pressure side; $C_{p_{\alpha=10^\circ}} - C_{p_{\alpha=0^\circ}}$.

(d) High-pressure side; $C_{p_{\alpha=-10^\circ}} - C_{p_{\alpha=0^\circ}}$.

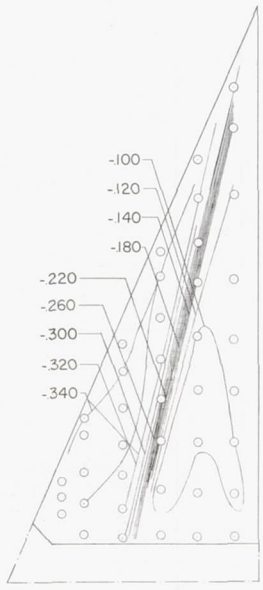
Figure 40.- Pressure contours for wing 3 at M = 2.41.



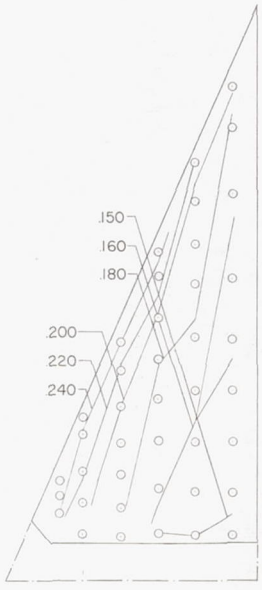
(a) Low-pressure side; $C_{p_{\alpha=5^\circ}} - C_{p_{\alpha=0^\circ}}$.



(b) High-pressure side; $C_{p_{\alpha=-5^\circ}} - C_{p_{\alpha=0^\circ}}$.

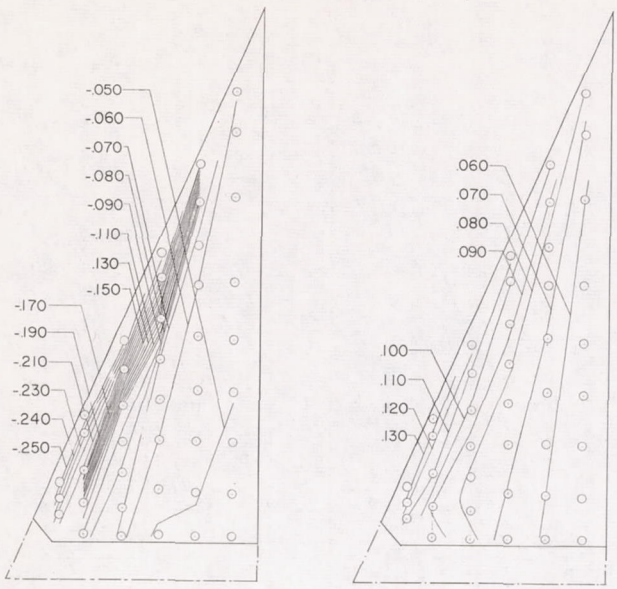


(c) Low-pressure side; $C_{p_{\alpha=10^\circ}} - C_{p_{\alpha=0^\circ}}$.



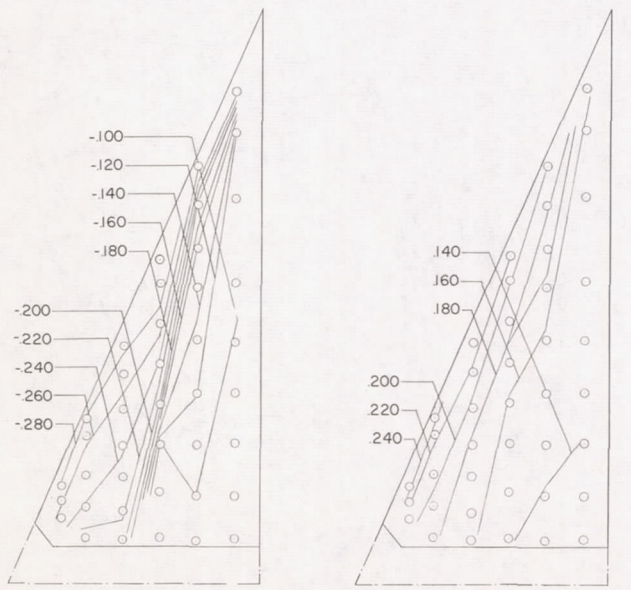
(d) High-pressure side; $C_{p_{\alpha=-10^\circ}} - C_{p_{\alpha=0^\circ}}$.

Figure 41.- Pressure contours for wing 4 at M = 1.62.



(a) Low-pressure side; $C_{p_{\alpha=5^\circ}} - C_{p_{\alpha=0^\circ}}$.

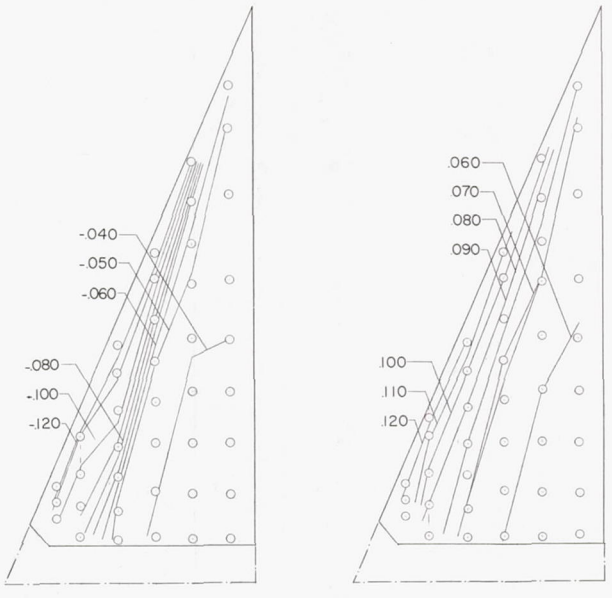
(b) High-pressure side; $C_{p_{\alpha=-5^\circ}} - C_{p_{\alpha=0^\circ}}$.



(c) Low-pressure side; $C_{p_{\alpha=10^\circ}} - C_{p_{\alpha=0^\circ}}$.

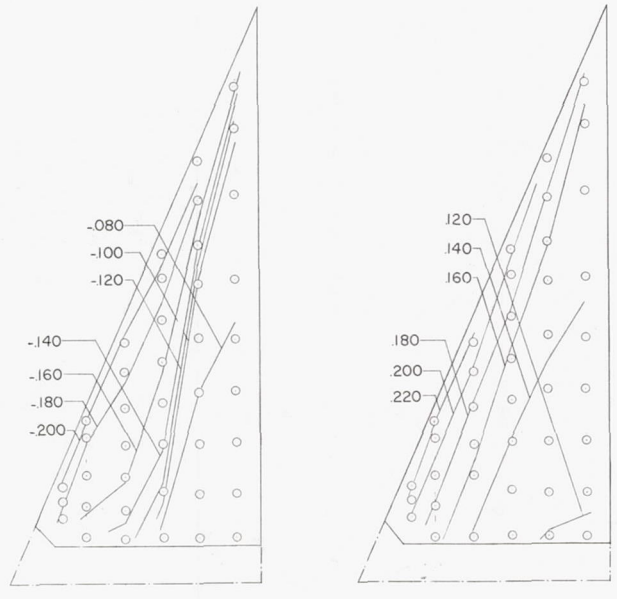
(d) High-pressure side; $C_{p_{\alpha=-10^\circ}} - C_{p_{\alpha=0^\circ}}$.

Figure 42.- Pressure contours for wing 4 at M = 1.94.



(a) Low-pressure side; $C_{p_{\alpha=5^\circ}} - C_{p_{\alpha=0^\circ}}$.

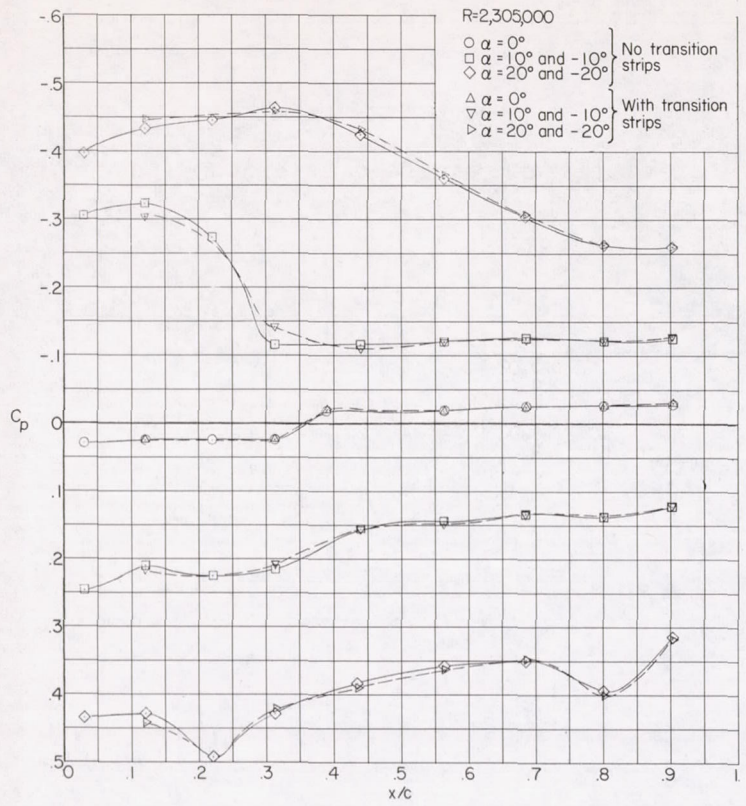
(b) High-pressure side; $C_{p_{\alpha=-5^\circ}} - C_{p_{\alpha=0^\circ}}$.



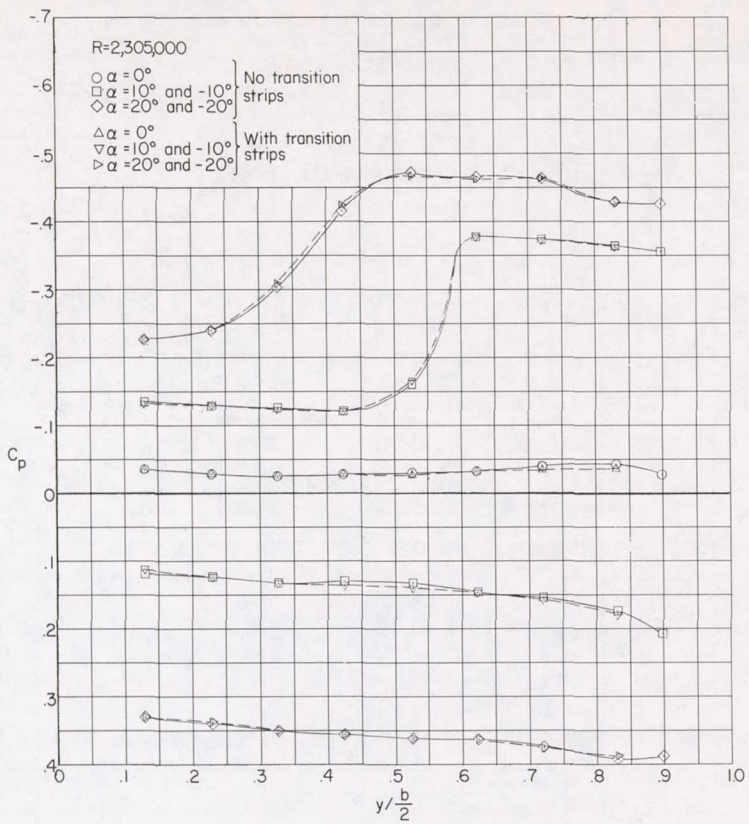
(c) Low-pressure side; $C_{p_{\alpha=10^\circ}} - C_{p_{\alpha=0^\circ}}$.

(d) High-pressure side; $C_{p_{\alpha=-10^\circ}} - C_{p_{\alpha=0^\circ}}$.

Figure 43.- Pressure contours for wing 4 at M = 2.41.

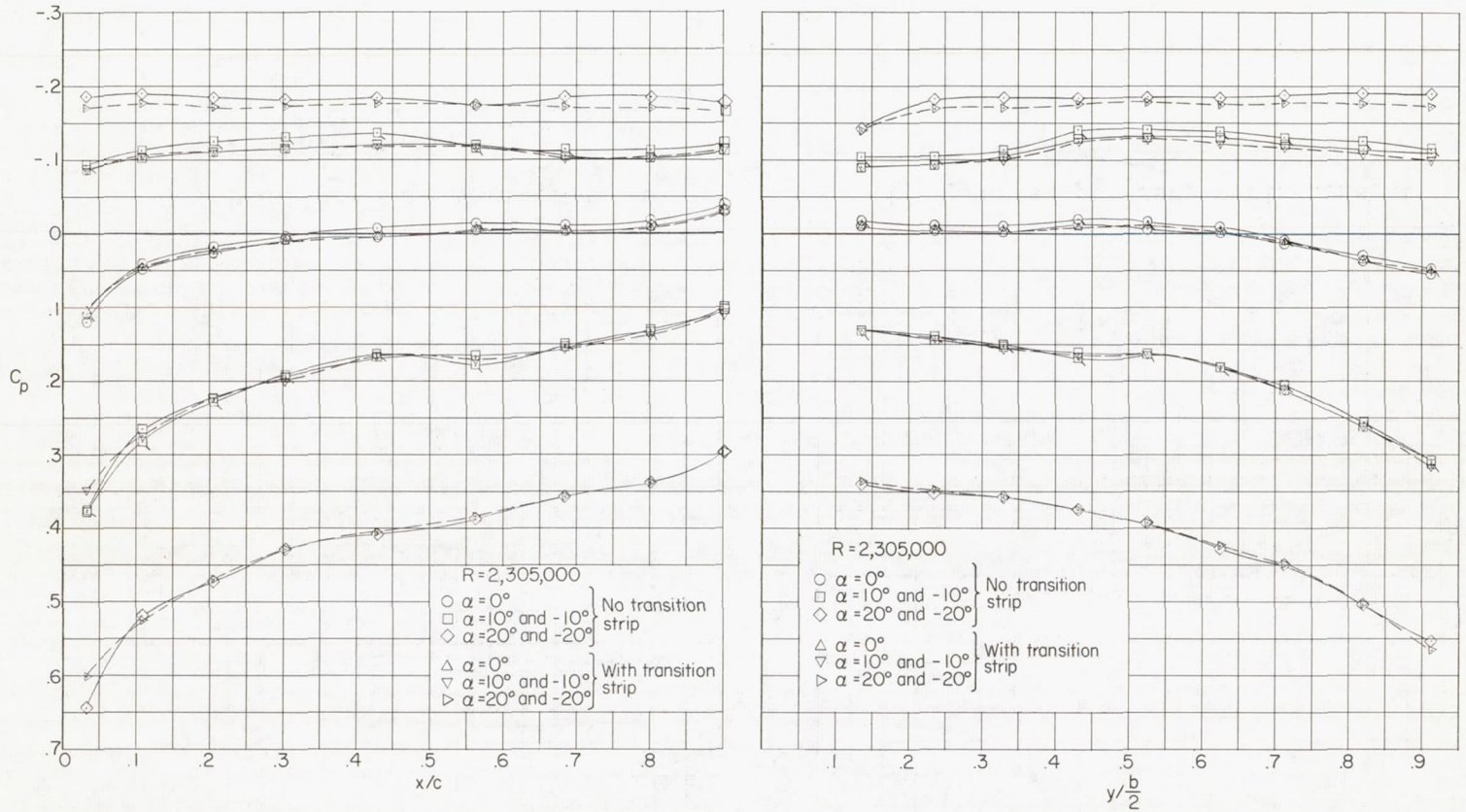


(a) Chordwise pressure variations at $y/\frac{b}{2} = 0.25$.



(b) Spanwise pressure variations at $x/c_r = 0.757$.

Figure 44.- Pressure distributions showing the effect of Reynolds number; wing 4 ($\Lambda = 66.6°$) at $M = 1.62$.



(a) Chordwise pressure variations at $y/\frac{b}{2} = 0.25$.

(b) Spanwise pressure variations at $x/c = 0.762$.

Figure 45.- Pressure distributions showing the effect of Reynolds number; wing 2 ($\Lambda = 53^\circ$) at M = 2.41. (Flagged symbols denote data at R = 4,650,000.)